

Dipl.-Ing. Christian Scholz

**Low friction slip-rolling contacts -
Influences of alternative steels,
high performance thin film coatings
and lubricants**

Die vorliegende Arbeit entstand an der BAM Bundesanstalt für Materialforschung und -prüfung.

Impressum

**Low friction slip-rolling contacts -
Influences of alternative steels,
high performance thin film coatings and lubricants**

2013

Herausgeber:

BAM Bundesanstalt für Materialforschung und -prüfung
Unter den Eichen 87

12205 Berlin

Telefon: +49 30 8104-0

Telefax: +49 30 8112029

E-Mail: info@bam.de

Internet: www.bam.de

Copyright © 2013 by

BAM Bundesanstalt für Materialforschung und -prüfung

Layout: BAM-Referat Z.8

ISSN 1613-4249

ISBN 978-3-9815360-2-7

Low friction slip-rolling contacts – Influences of alternative steels, high performance thin film coatings and lubricants

vorgelegt von

Diplom-Ingenieur

Christian Scholz

geboren am 22. April 1984 in Schönebeck

Von der Fakultät III – Prozesswissenschaften
der Technischen Universität Berlin
zur Erlangung des akademischen Grades

Doktor der Ingenieurwissenschaften

- Dr.-Ing. -

Genehmigte Dissertation

Promotionsausschuss:

Vorsitzende: Prof. Dr.-Ing. C. Fleck

Gutachter: Prof. Dr. rer. nat. W. Reimers

Gutachter: Dr.-Ing. M. Woydt

Tag der wissenschaftlichen Aussprache: 07.11.2012

Berlin 2013

D83

Stay hungry. Stay foolish.

Steve Jobs (1956 – 2011)

Stanford University, 2005

To my family.

Acknowledgments

This thesis is the result of three years research at the BAM Federal Institute for Materials Research and Testing (Berlin, Germany) in the division Macro-Tribology and Wear Protection (BAM 6.3). The completion of this work would not have been possible without the generous funding by the German Research Foundation (DFG) in cooperation with the BAM (DFG WO521/6-2).

First of all, I would like to express my sincere thanks to my supervisor Dr.-Ing. Mathias Woydt, who gave me the opportunity to start my professional development, initiated and intensively supported this PhD work as well as accepted to take part in the examination board. Prof. Dr. rer. nat. Walter Reimers, ordinarius of the Institute for Materials Science and Technology of the Technical University Berlin (TU Berlin), is also gratefully thanked for his interest in the thesis subject, for helpful comments and suggestions as well as for agreeing to participate in the graduation committee of this work.

I would like to thank also Prof. Dr.-Ing. Claudia Fleck, Chairman of the Material Engineering Department (Fachgebiet Werkstofftechnik) of the Technical University Berlin (TU Berlin), for taking over the chairmanship of the thesis committee.

All the staffs of the tribology division are also greatly acknowledged for bringing a pleasant working environment. Dr. Dirk Spaltmann is particularly thanked for the helpful discussions as well as for his proofreading (I firmly believe in your vision of CargoLifter airships). Dipl.-Ing. Manuel Reichelt will find here my many thanks for promoting constantly a good working atmosphere. Sigrid Binkowski and Dipl.-Ing. Norbert Kelling are also gratefully acknowledged for their constant and helpful technical support. André Otto and Sybille Weber are also thanked for their substantial administrative support.

Further on, I would like to express my thanks to my former colleague, Dr.-Ing. Charles-Alix Manier. With his tribological considerations and scientific work on Zr(C,N) and thin film coatings he laid the foundation of my thesis.

My sincere thanks go to Dr.-Ing. Werner Österle (BAM 5.1) for performing the highly relevant TEM investigations as also Dr. rer. nat. Ilona Dörfel and Heidemarie Rooch for the specific analysis and preparation of the samples.

Furthermore, I greatly appreciate the contributions of Dr. rer. nat. Sascha Dieter (former BAM 5.1, today Atotech Deutschland GmbH) for his valuable contributions in residual stress analysis of the steel substrates. I would like to thank Dr.-Ing. Eric Wild for performing synchrotron measurements at DESY (Hamburg) as well as the great help in considering the XRD results.

An important contribution to my thesis was given by Sigrid Benemann, Dr. rer. nat. Thomas Gross and Dipl.-Phys. Thomas Wirth (BAM 6.8), who conducted SEM/EDX, XPS and Auger investigations of the steels and coating materials.

Thanks are surely extended to BMW Group, Fundación Tekniker, KYB Corp. and Fraunhofer IWS for manufacturing of the coatings in industrial deposition chambers and to BAM 9.2 for the specimens preparation.

Last, but by no means the least, I would like to thank my whole family and all my friends for their support. My very special thanks go to my beloved wife Janett and daughter Paula Sophie for your understanding, support and confidence you have placed in me. My sincere thanks deserve my beloved parents, Katrin and Michael, and my brother Martin who were the pillars of this success by giving me the support and guidance throughout my life. Mom, I miss you so much. Dad, you are the best. Martin, I am proud of you.

Abstract

Due to the growing environmental awareness worldwide, containment provisions for CO₂ emissions in mobility systems and increasing performance requirements the demands on mechanical systems and their materials continuously rise. These high demands require the implementation of new technical approaches, for example of light-weight strategies in automotive powertrains, and directly raise questions about the suitability of the most promising technical solution. Two basic parameters, the surface hardness of the tooth flanks and the core fatigue strength of the tooth root, illustrate exemplarily increasing demands on material grades used for gear wheels in automotive powertrains.

In addition to light-weight strategies, a reduction in friction and an increase of the fatigue lifetime are two other major development directions to strive the mentioned targets. It is clear that any kind of solution must show an equal application profile, preferably an improvement, compared to the state-of-the-art solutions. For tribological systems, the following paths may offer lower friction and higher load carrying capabilities:

1. Alternative base oils and additives (such as esters, polyglycols),
2. Thin film coatings (e.g. DLC) and/or
3. Novel steel metallurgies.

In previous investigations on the slip-rolling resistance of thin film coatings (a-C, ta-C, Zr(C,N)) the substrates were mainly made of the bearing steels 100Cr6H and Cronidur 30. Applying contact pressures of up to $P_{0max} = 2.9$ GPa ($F_N = 2,000$ N), the samples were tested up to 10 million load cycles in endurance tests. The aim of the present work is to broaden the research by varying the input parameters. Newly developed engine oil mixtures, high performance thin film coatings and alternative steel solutions are intensively investigated in highly stressed slip-rolling contacts at lubricant temperatures of 120°C. Specifically, in using new steel metallurgies, i.e. the high toughness and high strength steels V300 and NC310YW (Aubert & Duval) as well as CSS-42L (Latrobe Specialty Steel Company), in combination with thin film coatings, even if they compete in the uncoated state, the Hertzian contact pressures could be increased up to $P_{0max} = 4.2$ GPa ($F_N = 5,000$ N) without any surface failures of coating or substrate. It was shown that selected thin film coatings can minimize the wear rates down to nearly 'zero-wear' in highly stressed contacts [Woy08] [Woy11]. In addition, the studies revealed not only the high potential in slip-rolling resistance, but also a possible friction reduction down to 0.047 by use of uncoated steels with increased toughness. Compared to steels like 100Cr6H and Cronidur 30 this means a reduction in friction of approximately 40% under identical testing conditions. Different test series with newly developed base oil-additive formulations were investigated with specific emphasis on the frictional behavior of selected bio-no-tox EP/AW additives and friction modifiers. Additional influencing factors like the structural and surface conditions of the steels/coatings before and after the tests were analyzed by means of REM, EDX, XRD and TEM.

Table of contents

Acknowledgments	IX
Abstract	XI
Table of contents	XIII
Nomenclature	XVII
1 Introduction and aim of this work	1
2 State of the art	5
2.1 Bearing and gear steels for advanced applications	5
2.1.1 Review on bearing materials	5
2.1.2 Review on gear materials	7
2.2 Rolling contact fatigue (RCF)	10
2.2.1 Evolution of residual stresses in rolling contact mechanism	10
2.2.2 White Etching and Dark Etching Areas	12
2.3 Fe-C-Si system	16
2.3.1 Effect of silicon alloying in martensitic and bainitic steels	19
2.4 Slip-rolling friction	21
2.5 Contact configuration (Hertzian contact)	22
2.6 Lubrication	25
2.6.1 Lubrication regimes	26
2.6.2 Tribological interaction of lubricant additives with metal surfaces	27
2.7 High performance thin film coatings	30
2.7.1 Vapor deposition	30
2.7.2 Temperature influence on formation and growth of thin film coatings	32
2.7.3 Low friction carbon-based coatings	33
2.7.4 Zr-based coatings	34

3	Experimental details	36
3.1	Characterization of testing materials	36
3.1.1	Chemical analysis	38
3.1.2	Heat treatment	39
3.1.3	Structure and hardness	40
3.2	Investigated coating systems	42
3.3	Twin disc testing machines	46
3.3.1	Amsler tribometer (A135)	46
3.3.2	Optimol 2Disc tribometer	47
3.3.3	Lubricant properties	48
3.3.4	Failure criterion, test abort criterion	49
4	Experimental results	51
4.1	Slip-rolling tests	51
4.1.1	Slip-rolling reference tests of uncoated steels	51
4.1.2	Slip-rolling resistance of coated systems	57
4.1.3	Tribological behavior of self-mated DLC coatings	64
4.2	Surface analysis at test end	66
4.2.1	SEM/ EDX observations	66
4.2.2	Chemical analysis of detected tribo-reactive layers (EDX-element mapping)	68
4.2.3	Further considerations on the chemical structure (XPS and AES)	71
4.3	Structural XRD results	75
4.3.1	X-ray diffraction profile of V300, NC310YW and CSS-42L	75
4.3.2	Residual stresses in manufacturing state	77
4.3.3	Residual stresses after tribological tests at $P_{0\text{mean}} = 1.94$ GPa	79
4.3.4	Residual stresses after tribological tests at $P_{0\text{mean}} = 2.5$ GPa	82

4.4	Structural analysis of cross sections after tests	84
4.4.1	Microscopic overview of steel structures and hardness	84
4.4.2	Further structural investigations (SEM, FIB/ TEM)	86
4.4.3	c_m/a_m ratio and soluted carbon content in V300 and NC310YW	96
5	Discussion and tribological considerations	100
5.1	Influence of alternative steels	102
5.2	Influence of high performance thin film coatings	104
5.3	Influence of lubricant additives	105
5.4	Global functional profile of coated and uncoated steels	107
6	Summary and Outlook	109
7	References	112
8	List of figures and tables	127

Nomenclature

Symbols

α	[-]	Ferrite
α_p	[GPa ⁻¹]	Pressure-viscosity coefficient
γ	[-]	Austenite
δ	[μm]	Total deformation/flattening
$\varepsilon_{\varphi,\psi}$	[-]	Lattice expansion
η	[-]	Corrective factor of asymmetry for calculation of Hertzian contact pressures
η_0	[mPa·s]	Oil dynamic viscosity at operating temperatures
θ	[°]	XRD peak position
λ	[-]	Tallian parameter, lubricant film thickness to roughness ratio
λ	[nm]	Wave length of XRD CoK α -radiation
μ	[-]	Friction Coefficient (equivalent to COF)
ν	[-]	Poisson's ratio
ξ	[-]	Corrective factor of asymmetry for calculation of Hertzian contact pressures
ρ	[g/cm ³]	Density
τ_{max}	[GPa]	Maximum shear stress
σ_{φ}	[MPa]	Residual stress value
σ_F	[N/mm ²]	Fatigue strength
σ_H	[N/mm ²]	Pitting strength
ν_0	[mm ² /s]	Oil kinematic viscosity at operating temperatures
φ	[°]	XRD rotation angle
ψ	[°]	XRD tilt angle
ω	[min ⁻¹]	Rotation speed
a	[m]	Semi major axis
a_m	[nm]	Lattice parameter of tetragonal elementary cell
b	[m]	Semi minor axis
B	[-]	FWHM value of XRD diffraction peak
c_m	[nm]	Lattice parameter of tetragonal elementary cell
COF	[-]	Coefficient of Friction (equivalent to μ)
D_{hkl}	[nm]	Grain size of cubic structures
E	[GPa]	Young's modulus
F_N	[N]	Normal force
F_R	[N]	Friction force
FWHM	[-]	Full Width at Half Maximum
k	[-]	Elliptical form parameter
k_V	[mm ³ /Nm]	Wear rate
K	[-]	Scherrer constant, depending on shape of the crystal and the grain size distribution
K_{IC}	[MPa·m ^{1/2}]	Fracture toughness
KV	[J]	Charpy toughness
HTHS	[mPa·s]	High-Temperature High-Shear

Nomenclature

L	[m]	Distance run under sliding
m_{ϕ}	[-]	Slope of the regression line of the functional relationship between lattice expansion $\varepsilon_{\phi, \psi}$ and residual stress value σ_{ϕ}
n	[-]	Number of load cycles
P_{0max}	[GPa]	Initial maximum Hertzian contact pressure
P_{0mean}	[GPa]	Initial average Hertzian contact pressure
r	[mm]	Radius
R_a	[μm]	Arithmetical mean roughness
R_m	[MPa]	Ultimate tensile strength
R_{ms}	[μm]	Root mean square (equivalent to R_q)
R_{pk}	[μm]	Reduced peak height
R_z	[μm]	Average maximum height
s	[%]	Slip-to-roll ratio
$t_{\Delta 2\theta}$	[s]	XRD measurement step duration
T	[$^{\circ}\text{C}$]	Temperature
v	[m/s]	Surface velocity
V	[μm^3]	Volume
V_{diff}	[μm^3]	Sliding speed
W_q	[μm^2]	Average worn surface in cross section
z	[μm]	Depth position of maximum shear stress

Abbreviations

a-C	Hydrogen free amorphous carbon
a-C:H:X	Doped amorphous carbon containing hydrogen
bcc	Body centered cubic
fcc	Face centered cubic
hcp	Hexagonal close-packed
pcnl	Process-controlled nanolayering
ta-C	Tetrahedral hydrogen free amorphous carbon
ta-C:H	Tetrahedral amorphous carbon containing hydrogen
ACEA	Association des Constructeurs Européens d'Automobiles
AES	Auger Electron Spectroscopy
AFM	Atomic Force Microscopy
AISI	American Iron and Steel Institute
ASP	Asea Stora Process
BAM	Bundesanstalt für Materialforschung und -prüfung
CAS	Chemical Abstract Service (CAS Registry Numbers)
COF	Coefficient of Friction
CVD	Chemical Vapor Deposition
DEA	Dark Etching Area
DIN	Deutsches Institut für Normung
DLC	Diamond-like Carbon
EBSD	Electron Backscatter Diffraction
EDX	Energy-Dispersive X-ray Spectroscopy

EHD	Elastohydrodynamic
EP/AW	Extreme Pressure/Anti Wear (additives)
FIB	Focused Ion Beam
FM	Friction Modifier
FWHM	Full Width at Half Maximum
FZG	Forschungsstelle für Zahnräder und Getriebebau
GMO	Glycerol Mono-Oleate
HTHS	High-Temperature High-Shear
HVB	Half-Value Breadth
IAP	Imaging Atom Probe
ISO	International Organization for Standardization
IST	Fraunhofer-Institute for Surface Engineering and Thin Films
LVDT	Linear Variable Differential Transformer
MoDTC	Molybdenum Dithiocarbamate
NASA	National Aeronautics and Space Administration
OCABS	Overbased Calcium Alkyl Benzene Sulfonates
OES	Optical Emission Spectrometer
OEM	Original Equipment Manufacturer
PACVD	Plasma Assisted Chemical Vapor Deposition
PAO	Poly-Alpha-Olefin
PAPVD	Plasma Assisted Physical Vapor Deposition
PDF	Powder Diffraction File (PDF-number)
PECVD	Plasma Enhanced Chemical Vapor Deposition
PVD	Physical Vapor Deposition
PESR	Pressure Electroslag Remelting
PSA	Peugeot Société Anonyme
RCF	Rolling Contact Fatigue
REACH	Regulation, Evaluation, Authorization and Restriction of Chemicals
SAE	Society of Automotive Engineers
SAED	Selected Area Electron Diffraction
SEM	Scanning Electron Microscopy
SIMS	Secondary Ion Mass Spectrometry
TEM	Transmission Electron Microscopy
TRIP	Transformation Induced Plasticity
VIM-VAR	Vacuum Induction Melting-Vacuum Arc Remelting
WC/C	Tungsten Carbide/Carbon
WDX	Wavelength Dispersive X-ray Spectroscopy
WEA	White Etching Area
WEB	White Etching Band
WEC	White Etching Crack
WEL	White Etching Layer
WSF	White Structure Flaking
XPS	X-ray Photoelectron Spectroscopy
XRD	X-ray Diffraction
ZDDP	Zinc Dialkyldithiophosphates
ZnDTP	Zinc Dithiophosphates

1 Introduction and aim of this work

Today's interest of automotive original equipment manufacturers (OEMs) is to increase power efficiency and reduce the fuel consumption as well as the environmental impact. They also strive to meet the CO₂-targets set by various governments, but especially the European Union¹. In 2009, the average passenger car in Europe emitted 146 grams CO₂ per kilometer. The new goals of 2015 and 2020 represent a cut of 11 percent and respectively 35 percent from the 2009 CO₂ emission level. Considering the CO₂ emission of new vehicles in the European market it became visible that numerous alternative driving concepts are already within the 2015 CO₂ limit (see Figure 1-1) [Leo11]. In order to meet the target of 2020 there is still a need of optimization in driving concepts. Although in public, the internal combustion engine is seen as the focus of efficiency gains, the whole powertrain offers at least the same range for improvements. In order to achieve these goals, there are three major directions of development:

- reduction in friction (carbon taxes),
- light-weight design (carbon taxes)
and
- increase in lifetime (maintenance costs).

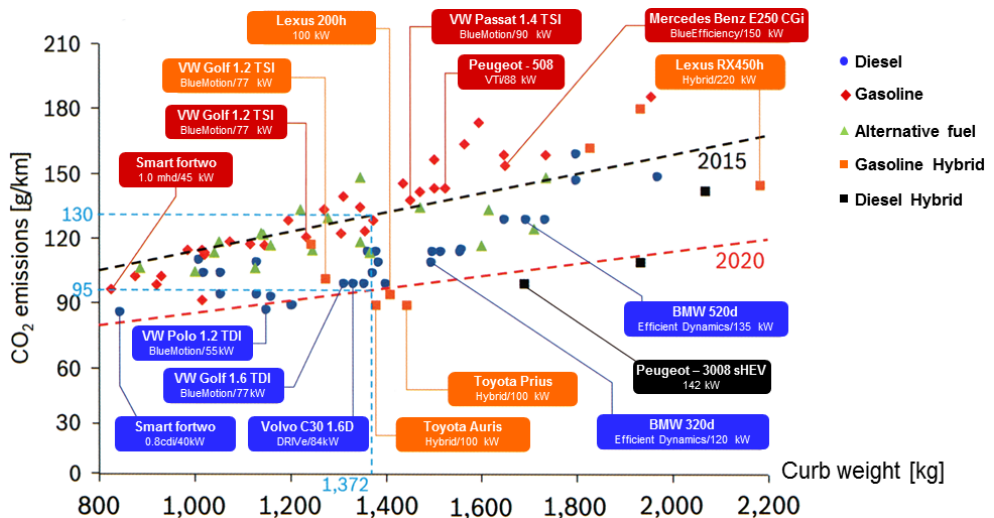


Figure 1-1: CO₂ emissions of selected engine technologies in the European Union over the kerb weight including the European CO₂ targets for 2015 and 2020 [Leo11]

The contributions of the powertrain to light-weight design are characterized by reduced component sizes and/or higher torques for the same component size (ISO-dimensions).

¹ European regulation (EC) No 443/2009 sets a target of 130 g CO₂/km from 2015 and 95 g CO₂/km from 2020 onwards for new car fleets. [EU09]

Introduction and aim of this work

Both aspects, reduced component size and higher torques, increase the Hertzian contact stresses, the PxV-values (pressure times velocity factors) and power density as well as the stresses in the material cores (volume). These high demands require implementations of light-weight strategies in powertrains, and directly raise questions about the suitability of the most promising technical solution. It is clear, that any kind of solution has to show an equal frictional profile, preferably a reduced friction compared to the state-of-the-art and at the same time at least an equal lifetime and/or fatigue life in side to keep maintenance costs at the same level or even below. For tribosystems, the following paths may offer lower friction and higher load carrying capabilities:

- I. thin film coatings (e.g. DLC)
- II. novel steel metallurgies
and/or
- III. alternative base oils and additives (such as esters, polyglycols).

The scheme shown in Figure 1-2 illustrates these development paths in more detail.

Alternative lubricant formulations may reduce the coefficient of friction under mixed/boundary lubrication, enhance fatigue life and increase extreme pressure behaviour (anti-galling) of uncoated and thin-film-coated-steels. Being 'chemicals', these lubricants are subjected to many regulations in view of their environmental impact (REACH², European Preparations Directives³). In consequence, the number of high performance additives available will be limited or restricted. Alternative base oils (esters, polyglycols) meet bio-no-tox criteria (low toxicity) and offer an attractive tribological profile. Although it is not imperative to respect these regulations at all times, keeping them in mind early in the product development cycle is both a corporate responsibility and good business practice. This is in line with the current vision of business solutions based on the philosophy referred to as 'Zeronize' [Toy07] [Ren02]. Zeronize symbolizes the efforts for the minimization of negative and adverse effects of energy conversion and mobility environment.

² REACH – Regulation, Evaluation, Authorization and Restriction of Chemicals, European Commission Environment, EC/1907/2006

³ EC/145/1999, amended by EC/8/2006, superseded by GHS "Global Harmonized System", EC/1272/2008

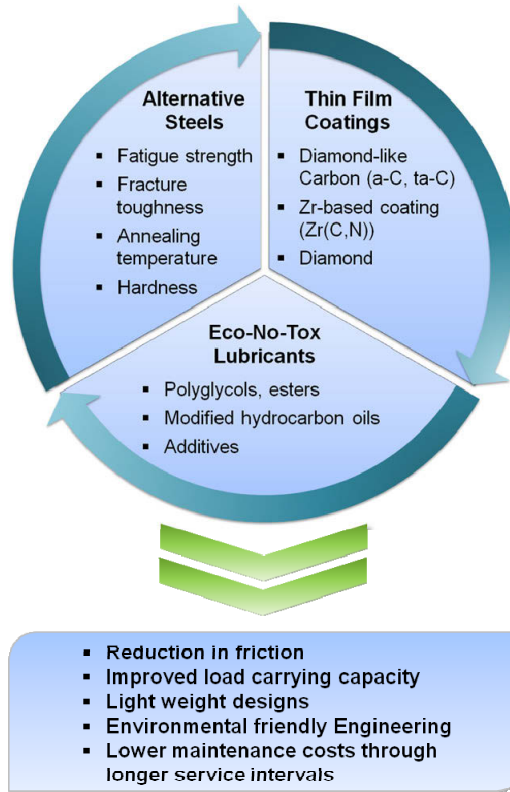


Figure 1-2: Scheme of aspired goals and approaches of this work

Recently, the load carrying capacity and slip-rolling resistance of some of the DLC, a-C and ta-C thin film coatings were significantly improved. Although thin film coatings have thus pushed the tribological barriers to new heights, they still do not comply with the quality demands (batch-to-batch) in mass production and functional needs in highly solicited tribosystems. In view of this, there is still room for improvements. Additionally, two major issues have to be considered for using coatings on carbon steel substrates. Firstly, especially carbon containing coatings need to match the constitutional behavior of the carbon steels. Secondly, the annealing temperature of these steels is generally not high enough to sustain the higher deposition temperature and time required for improved adhesion of such thin films.

Often, the influence is underestimated of the steel substrate on the adhesion of thin film coatings and the mechanical properties of the tribological system. Previous investigations conducted at BAM showed that by using nowadays common tempered steels, positive aspects of thin film coatings were ruined due to structural changes of the steel substrate during the coating process [Man10] [Man10-2] [Man10-3] [Woy10]. Due to a decrease in the hardness values of the steel substrate during deposition process, the metallurgy of steels

Introduction and aim of this work

needs to be optimized to higher annealing temperatures (above 300°C). Novel, but already existing steel grades can withstand sufficiently high deposition temperature for a necessary adhesion (metallurgical diffusion bonding) of modern thin films [Sch11].

This work presents the slip-rolling resistance (with a definite slip rate of 10%) of novel, high toughness steel grades with high annealing temperatures (V300, NC310YW and CSS-42L) in comparison to commonly used bearing steels 100Cr6H and Cronidur 30 in endurance tests. The second emphasis of the present work is to discuss the influence of high performance thin film coatings (a-C, ta-C and Zr(C,N)) on the slip-rolling resistance as well as the load carrying capacity, wear resistance and possibility to reduce friction values in the tribological contact. Therefore, slip-rolling tests up to initial average contact pressures of $P_{0\text{mean}} = 2.62 \text{ GPa}$ ($F_N = 5,000 \text{ N}$) were conducted with uncoated and coated steel pairings. Two lubricants, factory fill engine oil SAE⁴ 0W-30⁵ (High-Temperature High-Shear, HTHS = 2.98 mPa·s) and an alternative polybutylene glycol named PBG B20 (HTHS = 3.75 mPa·s) were used. For comparison, the chosen test parameter applied exceed the well-known and standardized stage above FZG 14⁶ [Sei71-72] for gear applications based on uncoated steel construction lubricated with fully additivated oils. Microstructural characterizations are carried out on the novel, uncoated steel substrates used as well as on DLC/Zr(C,N)-coated test specimen. The influence of lubricants on the formation of tribo-reactive thin films on steel and coating surface is additionally investigated.

⁴ SAE International is an organization for engineering professionals in the aerospace, automotive, and commercial vehicle industries developing standards for the engineering of powered vehicles of all kinds, including cars, trucks, boats and aircrafts.

⁵ SAE Standard J300 defines the limits for a classification of engine lubricating oils in rheological terms only. [SAE09]

⁶ Standardized scuffing load test in order to determine the scuffing load capacity of gear components ends at a load stage of FZG 12 according DIN 51354 or ISO 14635-1:2000. Limits and possibilities of FZG-torque change devices are described by Seitzinger et al. in [Sei71-72].

2 State of the art

2.1 Bearing and gear steels for advanced applications

2.1.1 Review on bearing materials

Until the 1960's, AISI 52100 (100Cr6) and some carburized steel grades, such as AISI 4320 (Ni-Cr-Mo-alloy steel) and AISI 9310 (10NiCrMo13-5), were adequate for most bearing applications. Materials, such as AISI 440, were applied in those cases where improved corrosion resistance was required. In 1957, Wilcock and Booser reported that AISI 52100 is not useful for operating temperature above 177°C. Therefore, only small lots of bearings made from M-1 and M-10 tool steels. These steel grades retain their hardness satisfactorily up to an operating temperature approaching 538°C. Almost simultaneously AISI M-50 steel was used for the first aircraft engine bearings. [Zar90]

The need for higher temperature capability led to the evaluation of numerous molybdenum and tungsten alloy tool steels as bearing materials. These steel grades offer excellent high-temperature hardness resistance. Nonmetallic inclusions in such highly stressed steels, due to melting and casting processes in air environment, had a negative impact on the fatigue resistance. Therefore, techniques such as vacuum induction melting (VIM) and vacuum arc remelting were developed. The steel cleanliness and homogeneity are major factors that determine the rolling bearing fatigue life of the steel. Ordinary steel can be considered clean if its content of impurities, such as phosphorus, sulphur, silicon and aluminum, is very low. These impurities form in combination with oxygen non-metallic inclusions [Rad11]. Impurities in bearing steels have been extensively explored and a large number of investigations showed the positive aspects of clean steels. Figure 2-1 illustrates the effect of applying special melting and heat treatment processes on the lifetime in case of 100Cr6 steel.

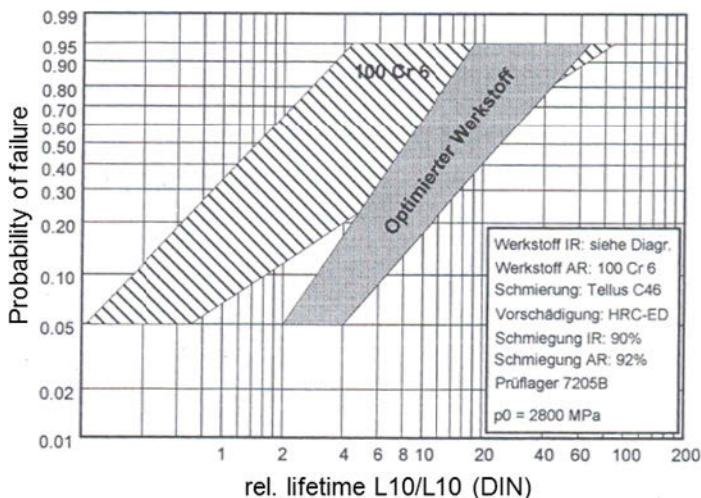


Figure 2-1: Increase in lifetime by use of optimized 100Cr6 in comparison to commonly melted and treated 100Cr6 [Woy10-2]

State of the art

The existence of non-metallic inclusions acts as stress riser, able to initiate micro-cracks during the repeated contact stresses introduced by the rolling load in the shallow layer of the raceways. Eventually, these microcracks can break through the raceway surface and in time spalling may occur and lead to total bearing failure (cf. Figure 2-2) [NSK12].

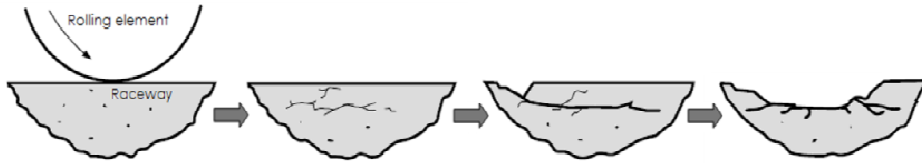


Figure 2-2: The progressive stages of spalling forming in relation to non-metallic inclusions [NSK12]

Surface-hardened or carburized steels, such as M50NiL, are used in many bearing applications because of their resistance to shock loads or cyclic bending stresses. On the contrary, the fracture toughness of through hardened steels is inadequate.

According to Radu there are mainly two types of rolling bearing steels [Rad11]:

- Trough-hardened steels, for which, after the final heat treatment, the hardness attains high values of 58 – 64 HRC in the entire volume of the bearing element.
- Case-hardened steels, for which a carburizing treatment increases the carbon content up to 0.65 – 1.10% only in a superficial layer of 15 – 25 mm thickness. Here a proper hardening and tempering treatment ensures the desired high hardness of 58 – 64 HRC, while maintaining the rest of the material at a much lower hardness of 25 – 48 HRC to provide a better operating toughness.

Over the years, the specific requirements of rolling bearings, i.e. rolling contact fatigue strength, resistance to contact deformation and wear, toughness, machinability and hardenability, led to special grade steel commonly known as bearing steel [Har07].

The aforementioned requirements are especially relevant in bearings of windmills. Bearing in windmills are used in severe conditions with numerous potential damage mechanism. Bore size diameters ranging from 1,500 mm for primary shaft to less than 100 mm for high speed shaft. Due to the wind gust some overloading can occur so that the nominal Hertzian contact pressure of 1.2 – 1.6 GPa may be exceeded. In this case, cleanliness and porosity are important to prevent sub-surface deep spalling. Aside from overloading, insufficient lubrication of bearings used in wind turbine gearboxes lead to micropittings or large spalling on the surface. To face these various damage mechanisms, steelmakers propose different metallurgical solutions, even offering through-hardened or case-hardened steels. In gearboxes, debris denting on bearing raceway can be limited with the use of through-hardened or case-hardened bearing steels with high levels of retained austenite. The soft phase of austenite accommodates plastic deformation during the denting of the surface and there-

fore avoids crack formation. A special steel grade, developed by Ascometal and named EndurAsco PR[®] multiplies the fatigue lifetime by a factor of 2.5 – 3. This type of steels based on a classical 100Cr6 containing additionally silicon and manganese. [Fla09]

Further information on bearing steels can be found within the review of Bhadeshia with the main emphasis on AISI 52100 (100Cr6) steel [Bha11].

2.1.2 Review on gear materials

The relative pitting fatigue lives of materials used in gear components is depends on a combination of operating conditions such as load, speed, lubrication system, temperature as well as production costs of the gears. For most applications, it becomes necessary to harden the gear teeth for improved strength properties and to case harden the gear tooth surface by case-carburizing or case-nitriding for longer pitting fatigue life, better scoring resistance and better wear resistance. Case carburized gears usually require grinding operations after the hardening process, due to distortions during the heat treatment. Nitrided materials offer the advantage of much less distortion during the process and therefore can be used without additional finishing. In many cases, the gear surface fatigue strength and bending strength can be improved by shot peening. As in the case of the steel grades 16MnCr5 (1.7131) and 18NiCrMo7-6 (1.6587), many gear steels have a limited operating temperature above which they begin to lose their hardness and strength. Resulting failures, such as bending failures, surface pitting failures or scoring can occur. Therefore advanced gear materials are necessary with higher tempering temperatures. [Zar90]

Recent research programs have been conducted to develop new gear steel alloys and new steel processing techniques to improve the performance of mechanical components. Relatively new alloys such as Ferrium 61, 64 or 69 utilize efficient nanoscale M₂C carbides strengthening dispersions within a Ni-Co lath martensite matrix. This new class of gear steel alloys using carbide precipitate strengthening dispersions offer a number of key benefits in manufacturing, as well as performance, over alloys. Reduced manufacturing complexity and variability could be generated by use of low-distortion gas quenching and by eliminating liquid quenchant systems and steps. Additionally, gear set weight could be reduced and power density could be higher due to increased surface fatigue resistance. Aside from AISI 9130 and Pyrowear 53, the aforementioned steels are used for example in helicopter gears. [Wri10] [Kra08]

Carburizing is widely applied to gears for automobiles for the purpose of improving fatigue strength and wear resistance. In recent years, 'stronger' and 'smaller' have been mounting demands to improve the fuel economy and reduce the vehicle weight as well as to increase the output of engines. Abudaia reported of nickel-chromium-molybdenum low alloy steels such as SAE 4320 and SAE 8620 alloys that are widely applied for automotive gear steels. These alloys contain about 0.5 to 0.8% Cr and 0.2% Mo with nickel content about 1.8 % in the former and reduced to 0.55 % in the latter alloy. Both these steels are carburizing grades with a basic carbon content of 0.2 %. Higher levels of strength and toughness are

State of the art

achieved by addition of silicon and vanadium to alloys of medium carbon content. It can be noted that the steels selected for gear manufacturing have changed significantly in recent years. For instance, EN36 was once widely used for large case carburised marine gears. The high nickel content (3.5%) produces a high level of hardenability. Experience showed that EN36 gave relatively little problems to manufacturers (for example it was reported to be resistant to grinding burns). On the other hand, nickel is an expensive chemical element and cost factors have led to the replacement of EN36 with alternative alloys in many applications. At the other end of the scale, SAE 8620 is lean in nickel, but its hardenability is adequate for the production of small gears. Consequently, SAE 8620 is favored by automobile manufacturers for automotive gears. [Abu03] [Kan95]

Recent researches were conducted on advanced gear alloys for ultra-high strength applications by the Boeing Company in order to increase the power density of gears in aircraft applications by 40 % while reducing the production costs by suitable high strength steels [She11]. The gear alloys were selected (Pyrowear 675 (Carpenter Technology Corporation), Aermet 100 (Carpenter Technology Corporation), Ferrium C61 and Ferrium C64 (QuesTek Innovations, LLC)) after a preliminary evaluation of a larger material matrix that had also consisted of CCS-42L and LESCO53 (Timken, Latrobe Specialty Steel), 32CDV13 and XD15NW (Aubert & Duval) ferrous alloys. Consistent with other research, it was recognized that aside from greater bending and contact fatigue performances of the steels, increased thermal stability compared with AISI 9310 crucial necessary for high demand applications. Shen et al. reported conditions of high temperatures initiated by "oil-out" or low lubricant situations.

A tungsten-containing Diamond-like carbon coating exhibiting high hardness, low friction, and good toughness was evaluated for application to spur gears by Krantz et al. in 2003. Fatigue testing was conducted at the NASA Glenn Research Center on both uncoated as well as coated spur gears. The results showed that the coating extended the surface fatigue lives of the gears by a factor of about 5 relative to the uncoated gears (cf. Figure 2-3). All gears were tested using 5-centistoke synthetic oil, a 10,000-rpm rotation speed, and Hertzian contact stress up to 1.9 GPa. Tests were run until either surface fatigue occurred or 300 million stress cycles were completed. Today, the mostly applied steels in gear components are 16MnCr5 (1.7131) and 18CrNiMo7-6 (1.6587).

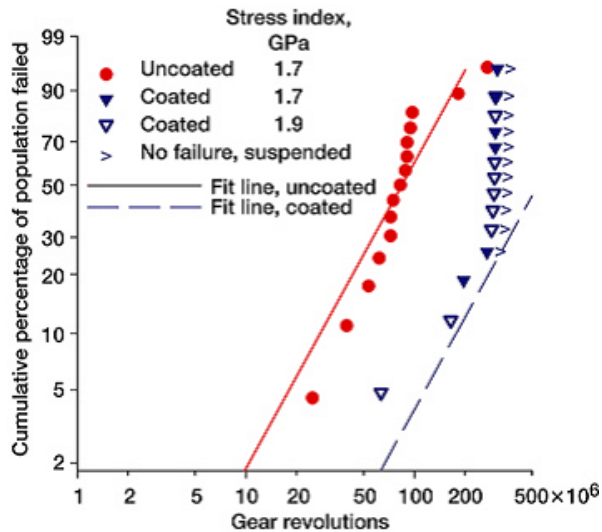


Figure 2-3: Weibull plot of fatigue test data for both uncoated and coated spur gears illustrates improved fatigue lives of coated gear parts [Kra03]

Latest developments in the field of bevel gears tend to apply Diamond-like carbon coatings on transmission gear components in order to reduce the frictional power loss and increase the power efficiency. H.E.F. groupe and PSA Peugeot Citroën was able to verify a frictional gain of 2.5 hp by applying DLC on bevel gears (see Figure 2-4) [Mau12]. As well as H.E.F. and PSA Peugeot the BMW Group applied a DLC on drivers with hypoid toothing. The complex geometry of such gear components made an adjustment and optimization of the coating process necessary. Especially in the area of mixed/ boundary lubrication at high torques such coatings reveal their high potential in increasing the efficiency by up to 1.5% [Sch11-2].



Figure 2-4: DLC coated bevel gear components [Mau12]

2.2 Rolling contact fatigue (RCF)

Rolling contact fatigue is generally induced by cyclic loading of surfaces in contact under combined rolling and sliding operations. The formation of surface cracks leading to a failure of the tribological system is very complex to describe. It is mostly induced by material properties, contact geometry, kinematics, load, lubrication properties, temperature, cyclic deformation and surface topography. The interaction of all parameters determines which material can withstand rolling motion. RCF is encountered most often in rolling element bearings and gears, where high contact stresses due to concentrated, frequently changing loads during normal operating conditions occur [Gra10-2]. Nélias et al. reported two consecutive steps of rolling contact fatigue [Nel99]. In the first step, microcracks are initiated due to the local accumulation of dislocations within the contact bodies. Stress raisers at this stage are high local stresses and associated plastic deformation around subsurface inhomogeneities or surface defects. The second step is the slow growth of microcracks until the fracture toughness of the material is reached, also known as micro-pitting. A selection of influences occurring during rolling contact fatigues are considered in the following sections. For example, the choice of lubricants, steel cleanliness, alloy selection, surface finishing, geometry, design as well as the manufacturing techniques are enhancements to reduce failures of components due to RCF and improve the life time [Gra10-2].

2.2.1 Evolution of residual stresses in rolling contact mechanism

Residual stresses in rolling bearings or gear components may be caused by manufacturing processes (grinding, polishing, shot peening) or during the operation. Böhmer considered the influence of residual stresses on the lifetime and operating performance [Böh10]. He reveals that a compression stress in the range of 10 to 20% of the Hertzian contact pressure during operation reduces the equivalent stress in the most heavily stressed material area and helps to increase the lifetime. The residual stresses also have a positive effect on the rate of fatigue crack propagation. In many applications, residual stresses are specifically implemented in the structure of the material, for example in roller bearing ring through nitration, carburization or martensitic hardening.

The evolution of the residual stresses caused by rolling stresses is shown in Figure 2-5 (left). In the area of maximum shear stress, the strongest changes in the residual stress profile are shown (residual stress maximum). These changes influence the material behavior and increases the life time in rolling contact [Sch88]. As well as the contact pressure, the slip rate has a decisive influence on the residual stress profile (cf. Figure 2-5 right). With high slip rates no compression stress maximum is formed such as at high contact pressures without slip (slip rates not exactly specified by Böhmer in [Böh10]).

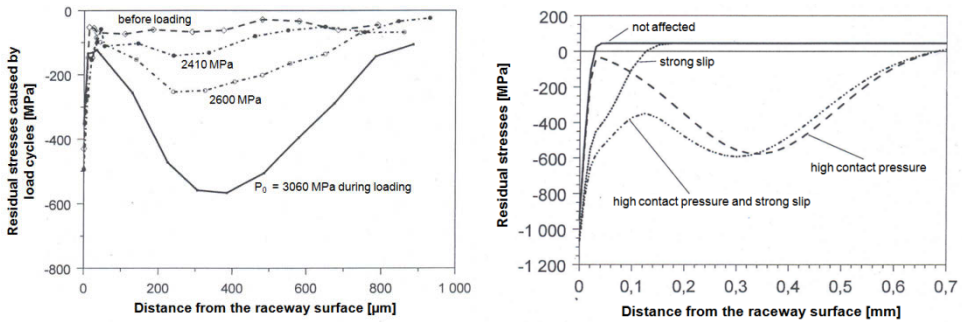


Figure 2-5: Evolution of residual stresses by cyclic rolling stress (left) and influence of contact pressure as well as slip on the residual stress profile (right) [Böh10]

Schlicht et al. as well investigated the role of residual stresses on the fatigue behavior of bearing steels [Sch88]. They assumed that compressive residual stresses influence the fatigue process during the first stage of fatigue process due to reducing the material stressing and thereby retarding plastic deformations. At very high contact pressures, the effect of residual stresses on life time can be neglected. They also proved the effect of compressive residual stresses on structural changes of material. Rolling contact elements of nearly the same hardness were subjected to 10^8 load cycles in a roller test rig at a contact pressure of 3.3 GPa. Plastic deformations in the structure are possible to illustrate and consider by the FWHM (Full Width at Half Maximum of X-ray diffraction peak), also known as Half-Value Breadth (HVB). A reduction of in the FWHM profile implies plastic deformations mostly in the area of maximum shear stress values (cf. Figure 2-6 left). Even a distinct difference in the residual stress profile between martensitic and bainitic structures can be measured after cyclic loading.

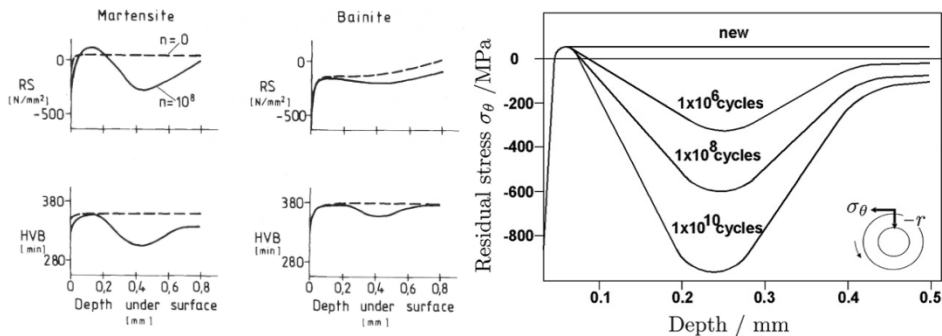


Figure 2-6: Changes of residual stress and half-value breadth through cyclic stressing of martensitic and bainitic structures [Sch88] (left) and residual stress profiles as function of number of cycles for a 52100 steel (850 HV) at 3.2 GPa contact pressure [Bha12] (slip rates in both figures not specified by the authors)

Additionally, in his study, Voskamp analyzed the magnitude of residual stresses at distinct number of load cycles in bearings [Vos96]. He carried out a test series with 52100 steel

State of the art

deep groove bearing in tempered martensite state (850 HV) at a contact pressure of 3.2 GPa. The plotted chart in Figure 2-6 (right) shows a compressive stress peak (tangential stress) at a depth between 0.1 and 0.5 mm and increasing stress values with increasing numbers of cycles. He showed additionally that the state of the residual stress mainly spans in two dimensions: normal and tangential to the surface whereas the latter suggested being the driving force for crack growth [Kan12].

2.2.2 White Etching and Dark Etching Areas

There is a well-known correlation between the amount of cyclic plastic deformation and structural failures in rolling elements under distinct contact pressure. The rolling contact failures are attended by different structural changes, such as:

- microstructural changes
- dark etching and white etching areas (DEA and WEA)
- softening or hardening of the material
- particle assisted nucleation of cracks and
- cyclic crack growth [Bha90]

Particularly etching effects such as dark etching and white etching areas can be observed under reflected light in many bearing failures after etched with nital or picral (cf. Figure 2-7). White etching areas are divided in

- white etching bands (WEB),
- white structure flaking (WSF) [Kot10],
- white etching cracks (WEC),
- white etching layer (WEL) or
- butterflies

and were firstly described as a kind of martensite [Sch73] and occur in many rolling applications (bearings, hard turned surfaces and rail contacts). Many theories for the formation of white etching structures have been advanced in the course of the time [Gra10] [Har05] [Sch88]. Although white structures reveal the same etching behavior, there exist distinct differences in the generation mechanism of different white etching types.



Figure 2-7: Optical image of white etching areas through inner ring of a wind turbine main shaft roller bearing in the cross section below stressed raceway

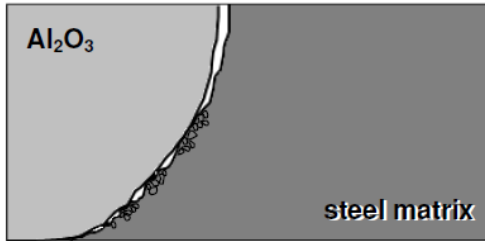
Butterflies are characterized as small cracks with altered microstructure wings of 10 to 250 μm length formed at a depth from affected surface up to 1.5 mm depending on the number of load cycles, temperature and contact pressure [Lun10] [Eva12]. Early explanations of the formation of butterflies are given for example by Schlicht et al. [Sch88]. Non-metallic inclusions in the material generate shear and tensile stresses in the surrounding material areas. By overstressing the material through cyclic stressing the elastic energy is concentrated in the area of non-metallic inclusions and is transformed into energy which is necessary for crack generation. Due to the cyclic stressing the crack generates in direction of the main shear stress. The hydrostatic pressure ensures that the originated crack surfaces are pressed against each other and deformed plastically. Consequently, the area is heated to austenitizing temperature and carbides dissolve. By self-quenching a martensitic highly deformed rehardening zone is generated.

Grabulov analyzed in his PhD thesis the early formation of butterflies and found a contrasting picture on the formation of butterflies to early works of Schlicht [Gra10] [Gra10-2]. Due to shear damage and repeated diffusion bonding/debonding during the stress cycling this interaction is occurred. As consequence of the continued fatigue exposure, the butterfly crack migrates sidewise from the inclusion/matrix interface out into the unaffected steel matrix. The driving force for this effect is a gradual material transfer across the formed butterfly wing and the undamaged matrix. It was a 'Three-Stage Embryonic Butterfly Formation Process', shown schematically in Figure 2-8, developed in the investigation of Grabulov, whereas white structures formed due to low-temperature recrystallization process. This process occurs as a result of crystal point defects stabilization by the presence of carbon in solid solution. Concerning the microstructure, Grabulov showed by TEM only ultra-fine ferrite grains in bcc structure (diameter 10 to 50 nm) without any temper carbides. Further examinations by means of EBSD revealed a grain refinement in the martensite matrix in the vicinity of carbides as a very complex structure of butterfly wing area (cf. [Gra10]). The measured micro hardness of steel matrix and WEA using nano-indentation techniques and was found as significant higher hardness than the steel matrix, up to 1100 HV whereas the matrix offers a hardness of 800 HV (SAE 52100).



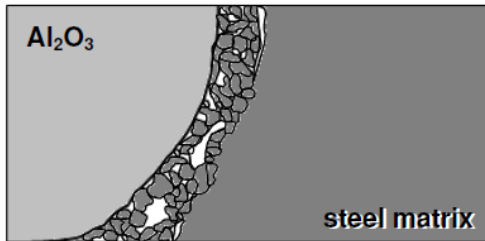
INITIAL STATE

- The alumina inclusion is fully debonded from the steel matrix
- Microstructure of the steel matrix is unchanged and consists of tempered martensite



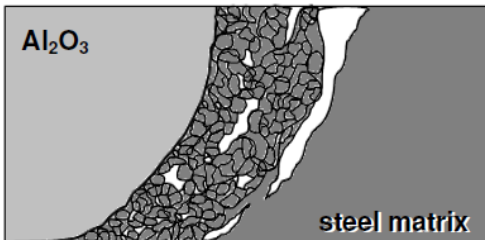
STAGE I

- Initial local interaction between the inclusion and steel matrix
- Rubbing movement induces local shear damage accumulation in the steel matrix and early material transfer from the steel matrix to the inclusion surface
- The deposited microstructure contains large quantities of crystal defects like dislocations and vacancies and is initially even amorphous



STAGE II

- Material transfer, or deposition, due to the rubbing movement continues
- Recrystallisation (RX) of the deposited seam leads to formation of nanometre sized ferrite grains
- Porosity in the RX seam may result from condensation of vacancies
- The initial "play" between the inclusion and the matrix is now found back at the interface between the deposited seam and the undamaged steel matrix as a nanometre sized crack-like feature and as nano-porosity



STAGE III

- Atomistic scale material transfer and dynamic RX leads to build-up of a nano-crystalline ferritic microstructure
- The crack-like feature develops further and migrates gradually out into the steel matrix by repeated deposition of material via a diffusion bonding-debonding cycle
- The deposited material builds up the white-etching butterfly wing
- The cooperative nature of the butterfly wing and crack growth becomes evident

Figure 2-8: Schematic development of early stage butterflies influenced by spherical Al_2O_3 inclusion in SAE 52100 steel [Gra10-2]

Furthermore Evans [Eva12] and Kotzalas et al. [Kot10] described in their review on white structure flaking in turbine gearbox bearings the formation of butterflies and white etching cracks caused by microstructurally changed white etching areas. Evans releases that butterflies and WECs are leading to WSF failure in typical SAE 52100 martensitic through hardened steel turbine bearing steel raceways as it is visible in Figure 2-9. The hardness of WEAs is typically 30 – 50% higher than the matrix [Eva12]. Concerning the structural composition, Kotzalas reveals that white etching areas can be identified as ferrite accompanied in many cases by black-striped microstructures of a pseudo-pearlite phase with the precipitation of cementite.

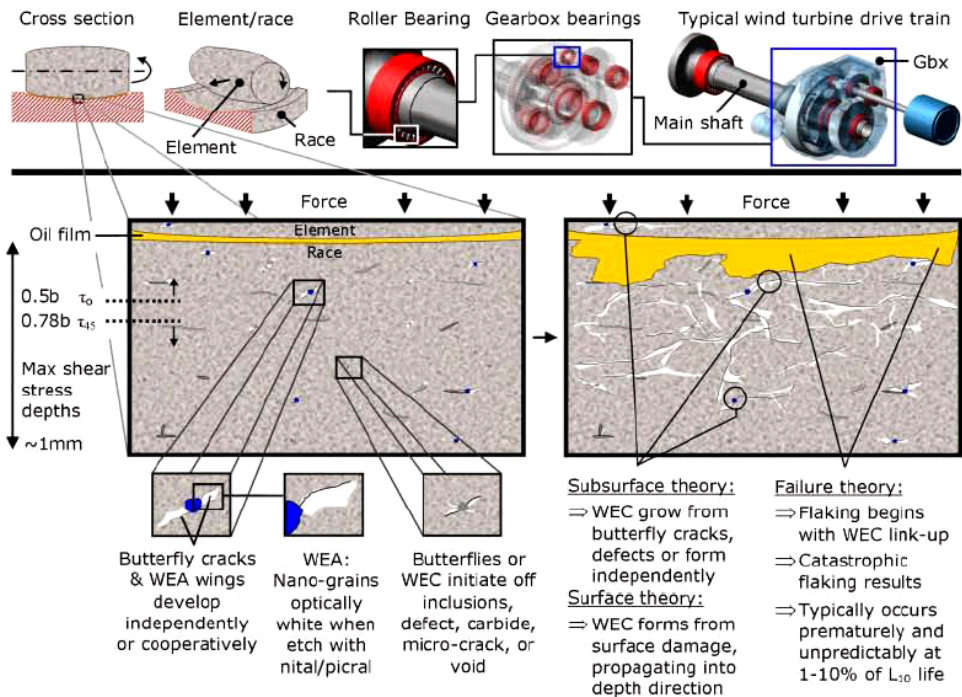


Figure 2-9: Schematic diagrams of Evans theory butterflies and WECs causing WSF failures in SAE 52100 bearing raceways [Eva12]

Considering the evaluation on white etching appearances in cyclic stressed steel materials, it became evident that by using a steel grade with fine grained microstructures and reduced amounts of inclusions (i.e. Al_2O_3) failures initiated by WEAs can be avoided. Looking at the statements and conclusions of the different investigations in literature on white etching structures it becomes clearly visible that many uncertain statements about the microstructural quality exist.

The second type of RCF related microstructural changes besides white etching structures are dark etching areas referred as dark etching areas (DEA). DEAs occur after a high number of cyclic revolutions in ball bearing inner rings. Swahn and co-workers reported a dark zone in the region of highest shear stress under the raceway of ball bearings between 10^7 and 10^8 load cycles [Swa76]. Dark etched regions extended in a transverse section of the inner ring from 0.1 mm under the contact surface to a depth of 0.5 mm. In addition to the number of revolutions, the evolution of DEAs is strongly dependent on the load level i.e. on the Hertzian contact pressure and the slip ratio [Öst80] [Sch88].

As mentioned before, the formation of DEAs is caused after reaching a minimum number of cycles (10^6) at maximum contact pressures above 3.3 GPa [Swa76]. From the darkness of the structure after polishing and etching and its position a conclusion can be drawn about the magnitude of the stress. The formation process of dark etching areas is described by

State of the art

Swahn as slip movement of dislocations along certain crystallographic planes and is characterized as a decay of the martensitic structure [Swa76]. In their investigations, Österlund [Öst80] and Böhmer [Böh99] deal with the structural changes and decay of martensite through cyclic reloading. Österlund summarized his work with the conclusion of a dark etching phase mixture in SAE 52100. He found a varying volume of a ferritic phase in the form of discs (thickness $\sim 1\mu\text{m}$, width $\sim 1\mu\text{m}$) intermixed with “residual” martensite. Using Cronidur 30, Böhmer et al. explained the dark etched regions as a retained austenite-martensite-transformation whereas the content of retained austenite decreases in the dark areas. Swahn as well analyzed the structure of DEAs by means of TEM and proved the areas as a mixture of ferrite and finely dispersed residual martensite. In addition, the latter of the structure contains very few cementite particles. A typical appearance of DEAs is shown in Figure 2-10. In contrast to WEAs, Muro et al. showed that the hardness of structural changed dark regions decreases [Mur70].

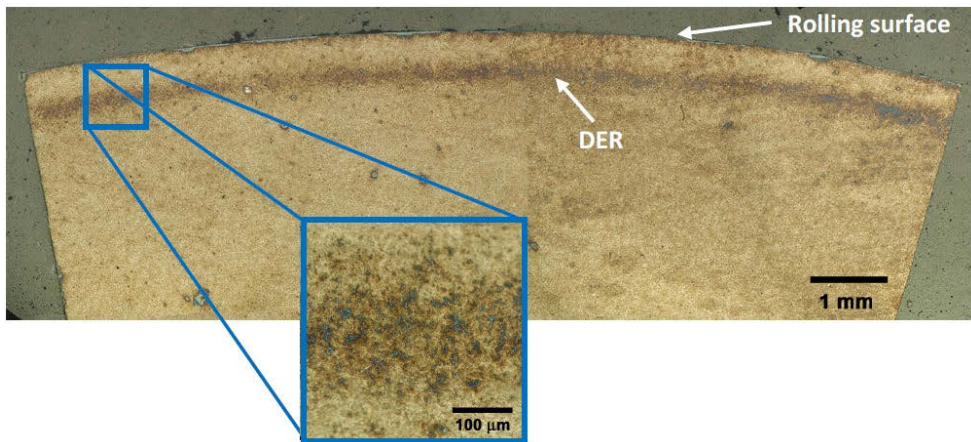


Figure 2-10: Optical micrograph of a dark etching area (within the image labeled as dark etching region DER) in cross section of a groove ball bearing after $2.4 \cdot 10^8$ load cycles under contact pressures of 2.6 GPa [Gra10-2]

As shown above, the Fe-C-system is obviously an active material system containing numerous phase and microstructural transformations. Due to this fact a quantification of a “stable” material system became necessary, which appears invariant with regard to rolling contact stresses and environmental influences.

2.3 Fe-C-Si system

Iron-silicon alloys (up to 6.5 wt.-% silicon) are widely used as soft magnetic materials for electrical devices especially for transformers and motors because of their enhanced electrical properties. By increasing the amounts of silicon, dissolved in the steel matrix, the electrical resistance and magnetic properties can be improved. Therefore, silicon steels with up to 6.5 wt.-% silicon have been developed in order to reduce eddy current and hysteresis

losses at higher frequencies and zero magnetostriction [Lia10] [Yan02]. The conventional rolling of thin sheets of this alloy faces the producers with enormous problems because of an extreme brittleness with increasing silicon amounts. Wittig et al. explained the reduced ductility of 4.5 to 6.4 wt.-% silicon alloys by solid solution hardening of silicon in the iron lattice. The reduction in dislocation cross-slip at higher silicon levels resulting in planar slip mainly on $\{112\}$ planes and increased chemical order that produces superlattice dislocation formation. Reducing the degree of chemical ordering and hence the formation of DO_{19} ⁷ superlattice structures by rapid solidification of iron-silicon cast alloys increased ductility by easier dislocation slip could be maintained [Wit08]. The assessment of the Fe-C-Si system is important for such aforementioned steelmaking processes and cast iron foundry. Numerous investigations on the Fe-C-Si system have been carried out with uncertain results, missing information and knowledge which is still limited [Lac91]. With his investigations, Kubaschewski proposed an experimental phase diagram of binary Fe-Si phases [Kub82] shown in Figure 2-11. A closer look at the Fe-Si phase diagram reveals nine stable and metastable binary phases.

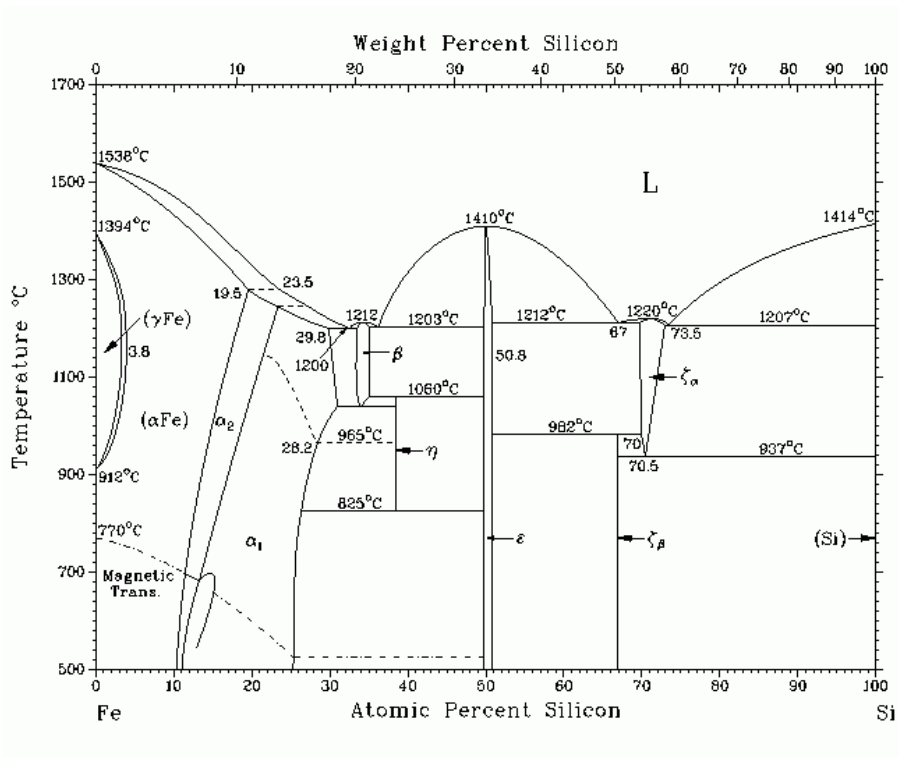


Figure 2-11: Experimental binary Fe-Si phase diagram [Kub82]

⁷ α_1 -Fe₃Si phase of Fe-Si system described more in detail in Table 2-1

State of the art

An overview about the binary phases of the Fe-Si system is given in Table 2-1. At low silicon contents, two phases of disordered solid solutions exist. In γ -FeSi (up to 3.8 at.-% Si between 912 °C and 1394°C) the iron atoms are ordered as face-centered cubic system whereas the silicon atoms hold interstitial positions at the octahedron spaces. This phase is comparable with the austenitic phase in the Fe-C system. The γ -FeSi is completely surrounded by α -FeSi (A2) of body-centered cubic structure. α -FeSi (A2) correlates to the ferritic phase in Fe-C. The following phases of FeSi with increasing content of silicon are α_1 -Fe₃Si (DO₃) and α_2 -FeSi (B2) modifications [Lac91]. The modifications of the DO₃ and B2 were considered by Warlimont, showing that the elementary cells differ in the lattice parameters a_0 and a'_0 and composition of the sublattices [War68]. Phases at silicon contents above 32 at.-%, starting with Fe₂Si form with DO₃ and ε -FeSi an eutectic. Further research on the Fe-Si system was performed by Rix [Rix01].

Table 2-1: Phase description of binary Fe-Si system

Phase name	Formula	Space group	System	Lattice constants [Å]	PDF number	Ref.
Fersilicite	γ -FeSi	Fm3m	fcc			[Msi08] [Rix01]
Fersilicite	α -FeSi (A2)	Im3m	bcc			[Msi08] [Rix01] [Lac91]
Gupeite, Suessite	α_1 -Fe ₃ Si (DO ₃)	Fm3m	bcc	a = 5.653	65-0994, 65-0237, 65-0146	[Msi08] [Wit08] [Rix01] [Lac91] [Kud77] [War68]
Fersilicite	α_2 -FeSi (B2)	Pm3m	bcc			[Msi08] [Wit08] [Rix01] [Lac91] [Kud77] [War68]
Hapkeite	β -Fe ₂ Si	P3m1	hcp	a = 4.052 c = 5.086	83-1259, 26-1141	[Msi08] [Rix01] [Kud77]
Xifengite	η -Fe ₅ Si ₃	P6 ₃ /mcm	hcp	a = 6.7416 c = 4.7079	89-2047	[Msi08] [Rix01] [Kud77]
Fersilicite	ε -FeSi	P2 ₁ 3	cubic	a = 4.489	89-7376, 89-2677, 65-1835, 38-1397	[Msi08] [Rix01]
Ferdisilicite	ξ_β -FeSi ₂	Cmca	orthorhombic	a = 9.986 b = 7.791 c = 7.833	71-0642	[Msi08] [Rix01]
Ferdisilicite	ξ_α -FeSi ₂	P4/mmm	tetragonal	a = 2.684 c = 5.128	89-2024, 73-1843, 65-2795, 35-0822	[Msi08] [Rix01]

Furthermore, several complex carbide formations of iron and silicon (silico carbides) exist in the ternary system such as metastable Fe₃SiC, Fe₄SiC, Fe₅SiC, Fe₆SiC, Fe₈Si₂C and Fe₉SiC₂. The composition of these ternary compounds strongly depends on the heat treatment of silicon, iron and steels. The complete description of all silico carbides and silicides are presented by Materials Science and International Team (MSIT[®]) in [Msi08].

2.3.1 Effect of silicon alloying in martensitic and bainitic steels

In principle, silicon is used as deoxidizer in the steel making process. In literature, the function of silicon in martensitic and bainitic steels is only briefly touched, leading to a still restricted point of view on the effects of silicon during steel transformations. In the following, a short literature review will be given on the effects of silicon alloying.

In Fe-Si-C system a silicon atom generally substitutes into an iron site, because the atomic radius of silicon (1.18 Å) is nearly similar to that of iron (1.24 Å) whereas the atomic radius of carbon is much smaller (0.71 Å) [Jan08].

Kardonskii reported the effect of silicon on the decomposition of the solid solution in maraging steels with different concentrations of molybdenum and silicon. It was shown by this investigation that silicon has a strengthening effect of approximately 10 times greater than that of cobalt in Fe-Ni-Mo alloys. It can be suggested that the addition of 0.1 % silicon is equivalent to 1 % cobalt. The second effect determined by measuring the lattice constants is that silicon effectively reduces the solubility of molybdenum in the ferrite phase. The values of the lattice constants after aging two alloys at 675°C for one hour were smaller for the silicon containing alloy. Furthermore, a hardening effect of increasing silicon contents in 10 % molybdenum containing alloy can be assumed [Kar70].

Aside from the use in electrical devices, silicon alloying is also of interest in the production of bearing steels. As alloying element its beneficial effect on tensile strength property and hardenability is well known [Kim10]. Kim et al. also concluded silicon as effective alloying element to increase the rolling contact fatigue life time. Due to the prevention of forming silica-based oxide inclusions in steel alloys, the occurrence of rolling contact fatigues i.e. WEAs and DEAs can be reduced [Gle10]. Larger concentration of silicon in SAE 52100 (0.85 wt.-%) has the advantage of reducing the chromium content whilst maintaining the hardness [Bha12].

For silicon containing steels, the formation of bainitic phases is of large interest along with some special characteristics. The formation of cementite is suppressed by silicon. In order to get a completely transformed bainitic structure, the formation of carbides is required. An incomplete transformation in silicon steels leads to high contents of retained austenite. As silicon is insoluble in cementite a diffusion process of silicon away from the cementite nucleus is necessary. Due to higher silicon contents around a cementite nucleus, the activity of carbon raises very strongly and carbon inflow is reduced, so that the nucleus is not able to continue growing [Bha79] [Lün91].

Aside from Bhadeshia and Lünenbürger, Sandvik precipitates in his research on the bainite reaction in Fe-Si-C alloys two clearly distinguishable stages of the decomposition of austenite into bainite [San82] [San82-2]. Because of the retardation of carbide precipitation, the decomposition takes place in a primary and secondary stage by use of silicon steels (2.0 – 2.4 wt.-% silicon) with large amounts of retained austenite. The primary stage is character-

State of the art

ized by the formation of essentially carbide free bainitic ferrite in very short time, whereas the austenite phases become strongly enriched with carbon. In this stage the substructural ferrite units, appear to have a plate shaped morphology formed at temperatures of 320°C and 380°C. According to examinations of Sandvik by optical micrographs, the structure of the silicon steel is upper bainite formed at 380°C and lower bainite at transformation temperature of 320°C. The differences between upper and lower bainite are considered in [Bha01] [Bha90] [Bha90-2]. A main feature of the bainitic ferrite is the considerably higher density of dislocations compared to austenite. It was also observed that in crystallographic orientation, displaced twins are different from the orientation of other ferrite plates. This strongly indicates that the bainitic ferrite is formed by shear transformation. Such a mechanism would be similar to that of certain martensitic structures. In these cases martensite plates are able to cross other pre-existing plates. The secondary stage of austenite decomposition takes place at very slow rates in comparison to the primary stage. It is established that the secondary stage is initiated by the formation of carbides partially of new type carbides [Bha79]. Sandvik observed a close relation of the lattice parameters of upper bainitic carbides formed during the second stage to those of cementite and χ -carbide (Fe_5C_2) [San82-2].

- Primary stage: displacive transformation of primary bainitic ferrite [San82]
- Secondary stage: diffusion controlled transformation of secondary bainitic ferrite [San82-2]

As mentioned before, the influence of silicon on the bainite formation is widely discussed in literature. Chang et al. pointed out different perceptions of the retarding silicon effect on the tempering process [Cha84]. One opinion is that silicon diffuses into the ϵ -carbide phase during the first stage of tempering and stabilizes it against transition to cementite. Other investigations could not establish any significant effect of silicon on the formation and stability of ϵ -carbides. In order to consider the effect of silicon, Chang et al. used a pure silicon alloy steel (1.4 wt.-% Si) and analyzed the silicon concentrations in segregated zones by means of time-of-flight and imaging atom probe (IAP). The analysis showed that silicon atoms form silicon-enriched zones at the interface between ferrite and cementite phases. Other significant results were the solubility of silicon in cementite as well as the diffusion in ferrite is very slow in comparison to carbon diffusion. Concluding the results of Chang et al., the silicon enriched ferritic areas apparently interact as kinetic barriers to the further growth of carbides. At the same time, this barrier prevents the silicon transfer from cementite to ferrite, so that the first formed cementite still contains appreciable quantities of silicon. Beside Chang et al., the research of Delagnes et al. dealt as well with the influence of silicon in a 5% Cr tempered martensitic steel [Del05]. It was shown that silicon reduces the flux of carbon which is required for the formation and growth of cementite. This effect increases the strength of the steel alloy due to the interstitial solid solution of carbon in the martensitic lattice.

The addition of 1.22 and respectively 1.76 wt.-% of silicon to two newly developed high-strength carbide-free bainitic steels is reported by Sharma [Sha11]. Due to the addition of silicon, the precipitation of carbides is suppressed. Impressive results (the combination of strength of 1557 MPa and toughness of 236 MPa·m^{-1/2}) were obtained for intermediate temperature of transformation due to the optimization in the fraction of bainite and retained austenite.

Moreover, silicon plays an important role in special high strength and high elasticity steel grades named TRIP-steels. The TRIP-effect (transformation induced plasticity) is characterized by the transformation of retained austenite contained in the steel matrix (10 – 14%) into deformation induced martensite during plastic deformation. The characteristics of TRIP-steels depend on the retained austenite volume and its stability. Silicon as alloying element (0.5 – 1.5 wt.-%) in TRIP-steels positively affects the solid solution hardening [Röt05] and retards the formation of cementite and carbides [Wan09] [Sta08].

With respect to the literature found, a unified image of the effect of silicon in bainitic and martensitic steels is not given. Especially, the arrangement of silicon in the lattice structure of steels or in the form of silicides could not be found in literature.

2.4 Slip-rolling friction

By definition, sliding or slip-rolling occurs when two bodies in contact have different driving speeds. In this case, the speed vectors are not equal in direction or value. For a car tire, the actual forward movement of the wheel does not correspond to the wheel circumference. As described by Manier [Man10] two different equations exist to express the slip-to-roll ratio. In order to calculate the slip ratio, the signs of the speed values need to be always positive in order to fulfill the basic definition of rolling (cf. equation 2.1). If the sign of the second rolling body (counterbody) is negative, it has the same motion of the main body and the resulting speed vector has an opposite direction at the contact point. However, the slip is so high that it does not meet the fundamentals of rolling and sliding occurs.

$$s = \frac{\vec{V}_1 - \vec{V}_2}{\vec{V}_1} \cdot 100\% \quad (2.1)$$

In industrial as well as laboratory applications, such as roller bearings, rolling friction plays a major role. Friction is defined as resistance to sliding, rolling or flowing motion of an object due to its contact with another counterbody. In case of pure rolling, the slip velocities are very small, normally < 1%. During rolling friction, both interacting bodies will undergo deformations due to their respective elastic characteristics. In consideration of a wheel rolling on a flat surface, the wheel flattens out in the contact point (according to the Hertzian contact theory, see paragraph 2.5) while a small trench is formed on the surface. Furthermore, with an appropriately high normal force, the wheel forms a sort of plowing motion resulting in increased deformation in front of the wheel. A small ratio of slip has occurred due to the

State of the art

deformation of the wheel and surface. The overall friction results in a force at the center of the wheel parallel to the surface of contact represented by equation 2.2:

$$F_R = \mu \cdot F_N \quad (2.2)$$

Speed as well as slip, lubrication, adhesion effects and roughness values of the bodies influence the rolling friction too. Indeed, the formation of the bead due to rolling friction can lead to rolling contact fatigue, as described in paragraph 2.2. A coating could reduce the formation of the bead with respect to the higher hardness of the coating compared to an uncoated surface [Man10]. The deformation of the surface is reduced and an improvement of lifetime can be noted. To some extent, the coatings should possess a distinct ability to withstand elastic deformation during the formation of the bead. Otherwise, the coating has no protecting character for the contact surface.

2.5 Contact configuration (Hertzian contact)

In 1881, the German physicist Heinrich Hertz was the first to describe analytically the reasons of deformation of two elastic bodies with curved geometry in static calculation [Her81], known as Hertzian contact pressures. The result of his considerations remains nowadays the only problem in contact mechanics which can be analytically resolved. With help of the Hertzian equations, body combinations like ball-ball, ball-plane and cylinder-cylinder as well as elliptic contacts can be calculated. Nowadays, many scientific investigations on contact mechanics and material behavior under contact stresses do not distinguish between maximum and average Hertzian contact pressure. Nowadays, this distinction according the Hertzian theory is absolutely necessary.

In order to enable the transfer of loads between two different bodies put together in relative motion, one or both of the parts are curved to create a defined contact. This optimization entails smaller contact surfaces as plane-to-plane geometry and consequently increases stresses in the contact area (mostly concentrated locally). Depending on the shape of samples, the contact geometry can be circular, linear or elliptical. By means of the equations of Hertz, geometric parameters of the contact and the contact pressures can be determined. The length of the semi major axis a and semi minor axes b forming the elliptical contact surface can be calculated by using the following equations [Man10]:

$$a = \xi \cdot \sqrt[3]{\frac{3 \cdot F_N (1 - \nu^2)}{\sum k E}} \quad (2.3)$$

$$b = \eta \cdot \sqrt[3]{\frac{3 \cdot F_N (1 - \nu^2)}{\sum k E}} \quad (2.4)$$

where
$$\frac{(1 - \nu^2)}{E} = \frac{1}{2} \cdot \left(\frac{(1 - \nu_1^2)}{E_1} + \frac{(1 - \nu_2^2)}{E_2} \right) \quad (2.5)$$

with E_1, E_2 the Young's modulus, 1 and 2 referring the two contacting bodies
 ν_1, ν_2 the Poisson's ratio, 1 and 2 referring the two contacting bodies
 ξ, η the corrective factors describing the deviation from ball-on-ball geometry
 k the contact parameters and F_N the normal force

The length of the semi major a and minor axis b allows calculating the maximum and average Hertzian contact pressures according to the equations:

$$P_{max} = \frac{1}{\xi \cdot \eta} \cdot \sqrt[3]{\frac{3 \cdot F_N \cdot (1 - \nu^2)^2}{8\pi^3 (\sum k)^2 E^2}} \quad (2.6)$$

$$P_{mean} = \frac{2}{3} \cdot P_{max} = \frac{F_N}{\pi \cdot a \cdot b} \quad (2.7)$$

Shigley et al. evaluated the maximum shear stress, τ_{max} , and principle stresses, σ_x, σ_y and σ_z , as a function of maximum pressure, P_{max} , beneath the surface contact point in a static case of two contacting spheres (Figure 2-12 left) and two cylinders (Figure 2-12 right) [Shi03].

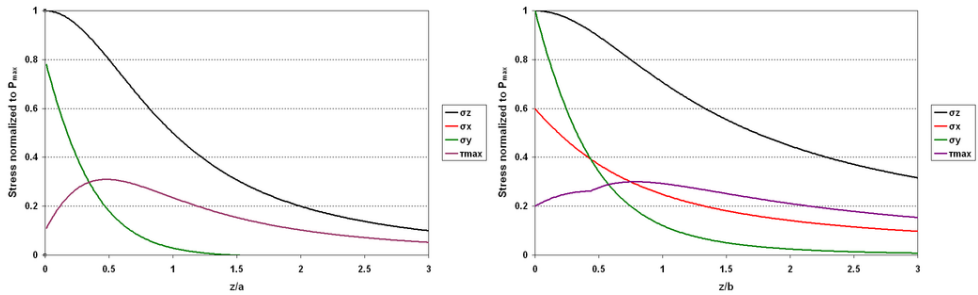


Figure 2-12: Magnitude of stress components below the surface as function of maximum pressure for contacting spheres (left) and cylinders (right) with $\nu = 0.3$ in static case [Man10] [Shi03]

The maximum shear stress at a certain depth position as well as the maximum deflection can be calculated in two ways. Model 1 uses the contact parameters k_1 to k_5 which can be found from the charts in Figure 2-13. The coefficients k_1, k_2 and k_3 are plotted against the k_0 coefficient defined in [Sta93]. The remaining coefficients k_4 and k_5 are shown in Figure 2-13 as chart against the k_2/k_1 ratio.

State of the art

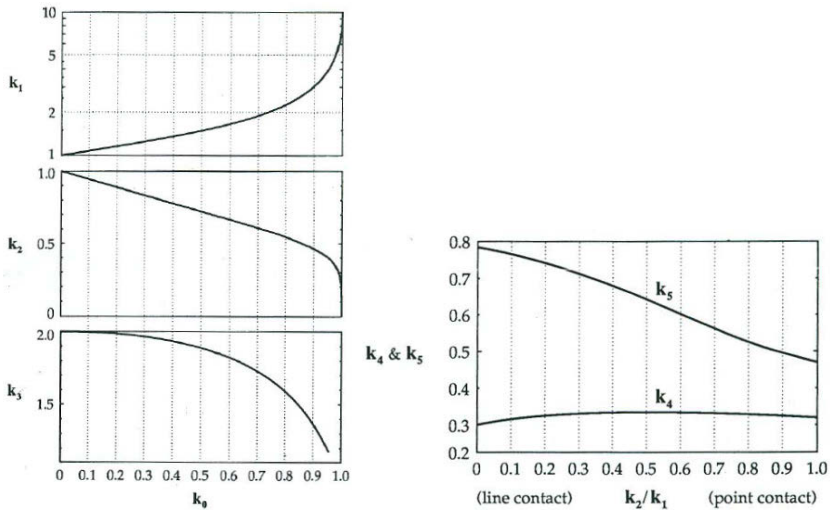


Figure 2-13: Determination of the contact coefficients k_1 , k_2 , k_3 , k_4 and k_5 [Sta93]

The maximum shear stress and depth position, depending on the maximum contact pressure, is given by the following equations:

$$\tau_{\max} = k_4 \cdot P_{\max} \approx 0.3 \cdot P_{\max} \quad (2.8)$$

at a depth position of

$$z = k_5 \cdot b \quad \text{with } b \text{ the semi minor axis of the contact ellipse} \quad (2.9)$$

The method of linear regression by the least squares, developed by Hamrock and Dowson [Ham81], has been applied to derive simplified expressions for the given contact problem. The formula developed, is applicable to any contact and eliminates the need to use numerical methods or charts such as shown in Figure 2-13. However, using the method of Hamrock and Dowson, an assessment of value and depth position of the shear stress is not possible. Using the shear stress hypothesis of Henri Tresca (1864), the depth position of the maximum shear stress can be calculated with (see Table 2-2):

$$z = 0.78 \cdot b \quad (2.10)$$

Table 2-2: Maximal, mean contact pressure and maximum shear stress with its depth position following the Hertz theory for elliptical contact used in twin disc testing machines (see paragraph 0) [Man10]

$R_{x1} = R_{x2} = R_{y1} = 21 \text{ mm}$		$E=208 \text{ GPa}$		Dubbel		Tresca	
$R_{y2} = \infty$		$\nu = 0.3$		$z = 0.59 \cdot b$		$z = 0.78 \cdot b$	
P_{mean} (GPa)	F_N (N)	P_{max} (GPa)	b (mm)	τ_{max} (GPa)	z (μm)	z (μm)	δ (μm)
1.00	287	1.50	0.239	0.45	-141	-186	6.1
1.25	561	1.88	0.298	0.56	-176	-232	9.6
1.50	970	2.25	0.358	0.68	-211	-279	13.8
1.75	1540	2.63	0.418	0.79	-247	-326	18.8
2.00	2300	3.00	0.477	0.90	-281	-372	24.5
2.25	3274	3.38	0.537	1.01	-317	-419	31.0
2.50	4492	3.75	0.597	1.13	-352	-465	38.1

Considering the influence of friction on shear stress it is clearly visible in Figure 2-14 that with an increasing coefficient of friction the maximum of the shear stress curve moves towards the surface of the stressed body. Thereby, an additional stress peak is formed at the surface. [Wut86]

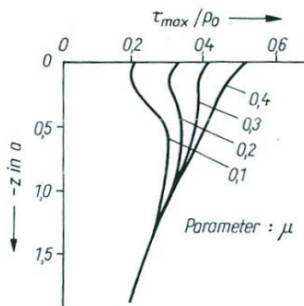


Figure 2-14: Development of the maximum shear stress depending on the coefficient of friction [Wut86]

2.6 Lubrication

Lubricants used in mechanical application have several important tasks [Sch10-2]:

- Transmission of forces due to hydrodynamic thin films and physical or chemical induced reaction films
- Dispersing and deterring of fluid or solid contaminations
- Removing of chips and cooling effects when used as cooling lubricant in metal-working
- Corrosion protection
- Reducing wear
- Evacuation of heat

State of the art

In most mechanical systems (transport, energy production, manufacturing), lubricants are used to reduce friction and wear between moving parts. Lubricants are composed of base oils and additions named additives or active substances. Despite continuous improvements of base oils the relevance of high performing additive packages increases due to increasing demands. Thereby, the interaction of a large number of different additives contained in the oils and the lubricated surfaces plays an important role. The additive package will nearly always contain antiwear additives, metal-containing detergents (e.g. salicylates, sulpho-nates), and ashless dispersants. In each of these classes of additives, the formulator may use a mixture of two or more components to achieve the desired performance profile. Supplementary additives such as antioxidants or friction modifiers may also be present. [Pir02]

The main focus of this paragraph lies on the interaction of lubricant additives with metal surfaces and the formation of tribo-reactive thin films. Further information about the composition of lubricants and the mode of action of selected additives can be found for example in [Rud09] or [Man07].

2.6.1 Lubrication regimes

The thickness of fluid films in tribological lubricated contacts determines the lubrication regime or rather the type of lubrication. Commonly accepted are three basic lubrication regimes illustrated in Figure 2-15. The distinction is based on different domains of the Stribeck curve, describing the evolution of the coefficient of friction over the ratio λ of lubricant film thickness to roughness ratio. The λ ratio is often simply known as Tallian parameter.

- Hydrodynamic lubrication valid for $\lambda > 3$ – two surfaces are completely separated by a fluid film
- Mixed/boundary lubrication valid for $1 < \lambda < 3$ – two surfaces are partly separated or partly in contact
- Boundary lubrication valid for $\lambda < 1$ – two surfaces are mostly in contact with each other even though a fluid is present

In some cases a fourth lubrication regime, called elastohydrodynamic lubrication, is mentioned. In elastohydrodynamic contacts two surfaces are separated by a very thin fluid film. A historical review of the Stribeck curve and the role of Adolf Martens are given by Woydt and Wäsche in [Woy10-2].

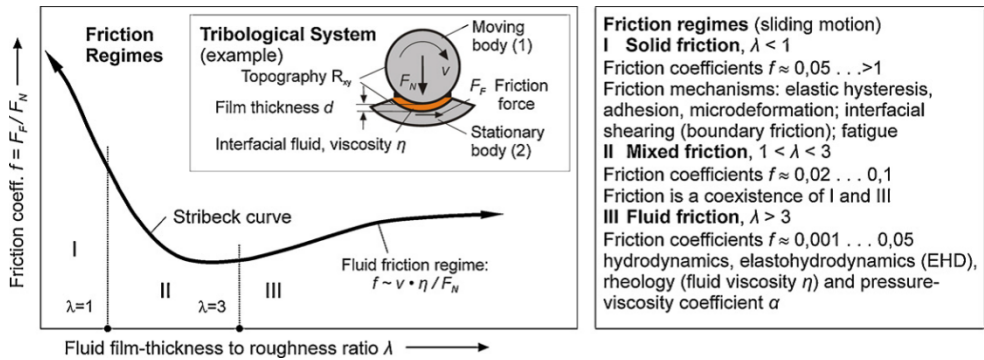


Figure 2-15: Characterization of friction regimes according to the Stribeck curve [Czi03]

Furthermore the surface topography or even surface texture, which refers to the arrangement or orientation of roughness, affects the lubricant film thickness. In case of EHD (elastohydrodynamic) or fully fluid contacts, the surface topography plays no decisive role due to the total separation of the facing surfaces. The surface texture has no influence as the λ ratio is high. However, as the facing surfaces are getting closer, the roughness values may play a role as the lubricant has a certain relaxation constant. The lubricant will not flow in the same way, if the texture is oriented in motion direction, or if it is transversal. [Man10]

2.6.2 Tribological interaction of lubricant additives with metal surfaces

Certain additives have the characteristic to form tribofilms on metallic as well as DLC-coated surfaces due to the absorption of distinct additive molecules on the surface. Physical interactions of additives and surfaces based on van der Waals, ionic, metallic and covalent bonds are described by Schulz et al. in [Sch10-2].

In general, control of the friction values in automotive engine systems in general is one of the most important problems the industry is facing. A decrease of the durability of mechanical systems and a significant increase in fuel consumption in automotive applications is caused by high friction values of rubbing surfaces. In order to address this problem, molybdenum dithiocarbamate (MoDTC) has been widely used as additive in engine oils. MoDTC additives are generally seen as cause for to the molybdenum disulfide (MoS_2) tribofilm formation due to tribochemical reaction. Onodera et al. studied the formation of LI-MoDTC (linkage isomer of MoDTC⁸) induced tribofilms on nascent iron surfaces [Ono10]. The study found an absorption structure of LI-MoDTC molecule forming chemical bonds between S-Mo-atoms in LI-MoDTC molecule and Fe-atoms. Furthermore, three different charges are assigned to three types of S-atoms, those that are bonded to one Mo atom, those bonded to two Mo atoms and those bonded to Mo and C atoms in the molecule (see Figure 2-16).

⁸ Linkage isomerism is the existence of co-ordination compounds that have the same composition differing with the connectivity of the metal to a ligand.

State of the art

The initial state of MoS₂ tribofilm formation can be observed by Mo-O bond dissociation which was induced by both catalytic and friction effects.

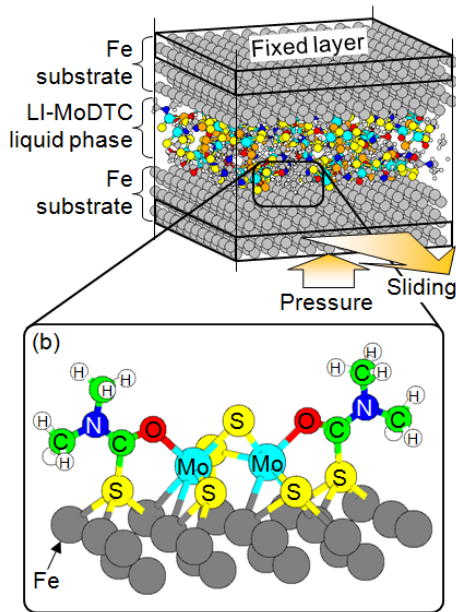


Figure 2-16: Dynamic behavior of LI-MoDTC molecule on nascent Fe(001) surface [Ono10]

Numerous researches dealt with zinc dialkyldithiophosphate (ZDDP) as one of the most common additives forming tribo-reactive films. There are several theories on the antiwear mechanisms of the ZDDP tribofilm summarized by Morina et al. in [Mor07]:

- Formation of a softer than substrate tribofilm which reduces the number of asperities in contact exceeding the shakedown limit
- Reduction of three-body abrasive wear by the decomposition of the iron oxide particles, by the ZDDP tribofilm debris reentering the contact and
- Formation of a phosphate glass structure which in contact conditions will behave as a viscous lubricant

Figure 2-17 gives the schematic model of the evolution of the ZDDP/MoDTC tribofilm with time, deduced from the chemical analyses of the tribofilm. The tests of Morina et al. [Mor07] were conducted in a reciprocating pin-on-plate tribometer (pin and plate made of AISI 52100) in the boundary lubrication regime. Loads of 50 N and 188 N were used which give initial maximum Hertzian pressures of 410 and 640 MPa, respectively. Furthermore, the tests were undertaken at sliding speeds of 0.02 m/s and 0.1 m/s whereas polyalphaolefin (PAO) lubricant with distinct additions of ZDDP and MoDTC additives was heated up to 100°C. MoS₂ was formed following the formation of a ZDDP and N-containing

film during the induction time. The interaction between ZDDP and MoDTC additives in friction performance is also likely to be an interaction between the tribofilms formed from ZDDP and MoDTC in the contact area. An initial study on the effect of ZDDP tribofilm on friction reduction from the MoDTC lubricant, done by applying a 'changing lubricants' procedure, clearly showed that if a tribofilm formed from a ZDDP-containing lubricant was further rubbed in a MoDTC-containing lubricant, the induction time prior to friction drop is significantly reduced, giving useful information about the interaction between ZDDP and MoDTC in low friction tribofilm formations [Mor04]. Another review of ZDDP focusing on its chemical characterization, film formation mechanisms, properties and structures is given by Nicholls et al. in [Nic05]. Nicholls et al. summarized several possible existing mechanisms for the formation of ZDDP antiwear films: thermal degradation, surface absorption, oxidation by hydroperoxide, radical reactions, hydrolysis and chemical reaction with FeO and oxygen in air or a combination of the above.

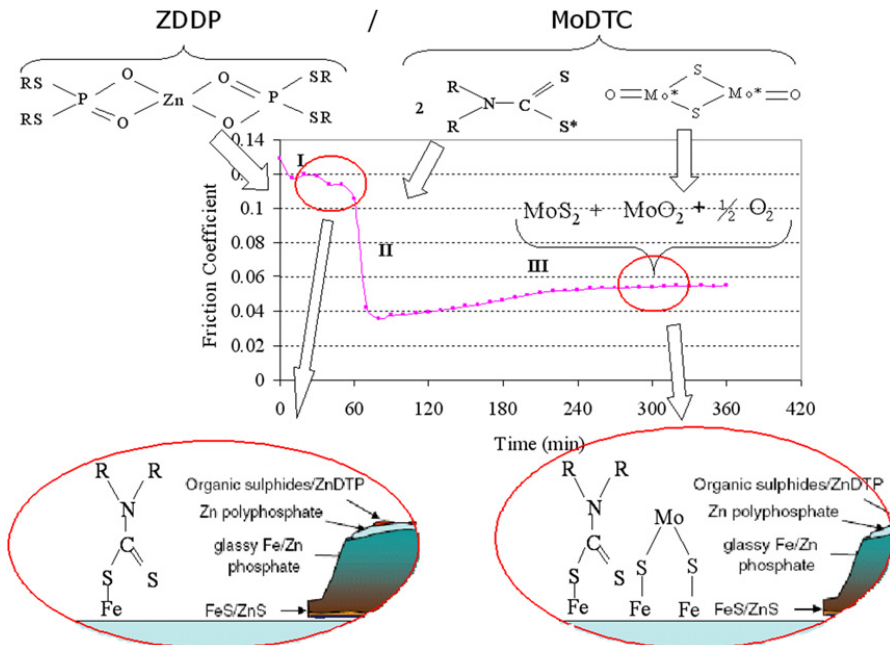


Figure 2-17: Schematic model and formation processes of the ZDDP/MoDTC tribofilm during the induction phase and at the end of the test. I – formation of N-containing species and ZDDP tribofilm resulting in wear reduction. II – adsorption of Mo oxide beside formation of species from process I. III – adsorption of MoS₂ and Mo oxide aside from ZDDP tribofilm [Mor07]

Another group of additives having the possibility to form tribofilms on metal surfaces are functionalized thiadiazoles. They have been widely studied for their application as bioactive compounds, surface-active and metal chelating agents⁹, cross-linkers for polymers, and

⁹ Chelators function in bulk of the lubricant by trapping metal ions to form an inactive or much less-active complex. [Rud09]

State of the art

components of cathode material battery systems. This broad class of compounds also finds application as additives improving tribological properties such as the wear resistance of steel surfaces and corrosion inhibition. The formation of a protective film at the steel interface mainly involves thermal additive decomposition under high loads. In most cases, however, the underlying chemical mechanism of tribofilm formation is not exactly understood. This is also true for thiadiazole derivatives. Functionalized thiadiazoles, such as 2,5-dimercapto-1,3,4-thiadiazole (DMcT), 2-mercapto-5-methyl-1,3,4-thiadiazole (McMT), and their derivatives, may serve as models to elucidate the surface chemistry of this class of compounds. Hipler et al. showed a remarkable high reactivity of thiadiazole molecules even on inert gold substrate. Therefore, this class of additives is used successfully as tribofilm forming additives. [Hip03]

Recent investigations of inorganic and organic nanoparticles used as oil additives showed an improvement in the tribological properties and displayed good friction-reducing and anti-wear characteristics. Especially inorganic mineral nanoparticles, described as Serpentine group, possess good as antioxidant, environmentally friendly, anti-wear properties and high thermal stabilities [Zha12]. The serpentine group describes a group of common rock-forming hydrous magnesium iron phyllosilicate ((Mg,Fe)₆Si₄O₁₀(OH)₈) minerals. They may contain minor amounts of other elements including chromium, manganese, cobalt and nickel. In the work of Zhao et al. serpentine/La(OH)₃ composite particles were synthesized, containing micro-serpentine coated by La(OH)₃ nanoparticles. A tribofilm was observed containing O, Si and Fe elements formed on the surface of the rubbing pair (MHK-500 Ring-block wear testing machine with GCr15 steel ball). The results suggested that the tribofilm was formed due to an ion exchange reaction between iron atoms and Mg²⁺ of the serpentine, the lanthanum acted as catalyst during the reaction. [Zha12]

2.7 High performance thin film coatings

2.7.1 Vapor deposition

Since materials like carbon are applied by vapor deposition in extremely thin, hard and wear resistant layers, they offer numerous new options for use in innovative and tribological relevant applications. The used vapor can be generated on one hand by a chemical reaction of different process gases and on the other hand by a physical reaction. These two major deposition techniques for thin film coatings are:

- Chemical Vapor Deposition (CVD)
- and Physical Vapor Deposition (PVD).

By condensation of the vapor on a substrate, thin films in the range of only a few nanometers and up to 40 μm (i.e. diamond thin films) can be created [VDI05]. The main distinguishing feature of both deposition techniques is the origin of the material. In case of a PVD process the material comes mainly from a solid state target whereas in a CVD process, the material is a product of the reaction between different gases. This gas reaction and its acti-

vation require higher temperature conditions (up to 800°C) as well as a similarly high substrate temperature for a proper deposition. The high temperature during a CVD process makes the application of many Fe-based materials such as steels extremely difficult. A special CVD coating process with lower process temperature is for example plasma-enhanced chemical vapor deposition (PECVD). It can be used to deposit coatings from amorphous to polycrystalline and further on to single crystal types. This procedure is often utilized to produce hydrogenated amorphous Carbon coatings (a-C:H). Through plasma decomposition of the process gases Acetylene (C₂H₄), Methane (CH₄) or other hydrocarbon gases, carbon atoms or ions are generated and form the coating by condensation on the sample surface the coating. Dopants such as Silicon, Nitrogen or Oxygen can be involved by appropriate process gases. [Kol04] [Sch10] [Ste05]

PVD coatings are generally deposited under high vacuum conditions (up to 1.33E⁻⁷ Pa, mostly 1.33E⁻³ Pa) with an inert background gas for example Argon [Sch10]. In the course of the years many different PVD techniques have been developed, a selection of them are:

- Cathodic arc deposition (Arc-PVD) used for metallic, ceramic and composite films (i.e. TiN, CrN, ZrN, Zr(C,N), TiAlSiN) by vaporizing material from a cathode target with an electric arc. [Man10]
- Ion plating or ion assisted deposition (IAD) is an atomistic vacuum coating process in which the surface of a substrate is sputter-cleaned and maintained clean until the deposition film material covers the surface. During deposition, the surface is bombarded periodically or continuously by atomic-sized energetic particles to affect the nucleation, growth and properties of the coating. [Mat00]
- Pulsed laser deposition (PLD) is a coating process in which a high-power laser beam is focused periodically inside a vacuum onto a target material causing an instantaneous evaporation and ionization of the surface atoms and forming dense plasma inside the plume of the evaporated material. [Lac05]
- Vacuum evaporation is a PVD process where material from a thermal vaporization source reaches the substrate without collision with gas molecules in the space between source and substrate. Typically, it takes place in a gas pressure range of 1.33E⁻³ to 1.33E⁻⁷ Pa. The vaporization sources are resistively heated by high-energy electron beams focused and rastered over the surface of the source material. [Kol04]

A decisive advantage of the PVD techniques compared to pure CVD techniques is the lower process temperature. Usually, the deposition temperature varies between 50°C and 500°C (cf. Table 2-3).

State of the art

Table 2-3: Typical characteristics of some coating processes (gaseous state)[Hol09]

Gaseous State Processes					
	PVD	PAPVD	CVD	PACVD	Ion Implantation
Deposition rate [kg/h]	up to 0.5 per source	up to 0.2	up to 1	up to 0.5	
Coating thickness [µm]	0.1 – 1,000	0.1 – 100	0.5 – 2,000	1 – 20	0.01 – 0.5
Substrate deposition temperature [°C]	50 – 500	25 – 500	150 – 12,000	150 – 700	50 - 200
Substrate material	Metals, ceramics, polymers	Metals, ceramics	Metals, ceramics	Metals, ceramics	Metals, ceramics, polymers
Pretreatment	Mechanical/chemical	Mechanical/chemical plus ion bombardment	Mechanical/chemical	Mechanical/chemical plus ion bombardment	Chemical plus ion bombardment
Coating uniformity	Good	Good	Very good	Good	Line of sight
Bonding mechanism	Atomic	Atomic plus diffusion	Atomic	Atomic plus diffusion	Integral

2.7.2 Temperature influence on formation and growth of thin film coatings

In all existing structure-governing phenomena of growing thin films, described in [Tho00], temperature and pressure of the process gas are parameters with strong influence on the microstructure of PVD coatings. As one of the first, Movchan and Demchishin discussed the temperature influence on the structure and properties of nickel, titanium, tungsten, aluminum oxide and zirconium oxide in 1969 [Mov69]. Figure 2-18 shows the structural zones as function of the substrate temperature and melting point of coating material. The model of Movchan and Dechimshin is divided into 3 zones. In zone 1 the condensate has a characteristic domed structure. With increasing temperature the diameter of the domes increases. Zone 2 reveals a smooth matt coating surface. Whereas the surface of zone 3 is bright with a polyhedral structure. Thorton expanded the structure zone model by the parameter of argon pressure to describe the microstructure of PVD coatings in 1974 [Tho74]. Within this diagram (cf. Figure 2-18) it was shown that the greater the energy input to a growing thin film, e.g. by means of increased substrate temperature, the greater will be the densification, and the lower will be the porosity [Hol09]. Amorphous coatings such as DLC are commonly deposited at temperatures around 200°C (even below room temperature). The aim of all coating developments was to comply with the annealing temperature of commonly used steels. Thus, the deposition temperature was reduced in order to maintain the heat treatment properties of the steels. This prohibits the formation of a metallurgical diffusion layer resulting in a strong bonding of the coating to the substrate surface. This strategy required metallic bond layers.

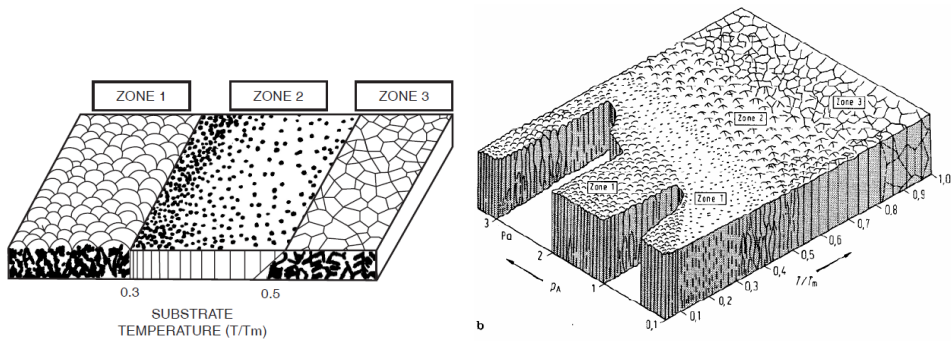


Figure 2-18: Schematic representation of structure zone models of Movchan and Demchishin (left) [Mov69] and Thorton (right) [Tho74] with the influence of temperature and argon pressure on the microstructure of metal coatings. T (K) is the substrate temperature and T_m (K) represents the melting point of the coating material.

2.7.3 Low friction carbon-based coatings

Since the middle of the 1980s diamond and especially diamond-like carbon-based (DLC) coatings have rapidly become interesting for a number of researchers. Today, DLC coatings and their variations can be counted to the most intensively researched tribological coatings. The commercial interest in carbon based coatings is grounded on the unique material properties and the great potential in tribological applications. Of particular interest are properties such as high mechanical strength, chemical inertness, low friction values and excellent wear resistance as well as high hardness. By listing the main properties of carbon based coatings it quickly becomes evident that this coating type is inevitable for low friction contacts. [Hol09]

According to the VDI guideline 2840 [VDI05], DLC coatings can be divided into the following main categories:

- a-C: hydrogen-free amorphous carbon coating
- ta-C: tetrahedral hydrogen-free amorphous carbon coating
- a-C:H: hydrogenated amorphous carbon coating
- ta-C:H: tetrahedral hydrogenated amorphous carbon coating
- a-C:Me: metal-containing hydrogen-free amorphous carbon coating (Me = W, Ti...)
- a-C:H:Me: metal-containing hydrogenated amorphous carbon coating (Me = W, Ti...)
- a-C:H:X: modified hydrogenated amorphous carbon coating (X = Si, O, N...)

The most important structural parameters to distinguish the different DLC coating types are the ratio of sp^3/sp^2 bonded carbon, the hydrogen content, the chemistry and microstructure in the coating. Further details about influences and measurements of sp^3/sp^2 ratio and their characterization are considered for instance by Holmberg et al. [Hol09] and Ferrari [Fer08].

As in every tribological system, the coefficient of friction and low friction properties depend on the contact system. That is why the friction values for example in sliding and rolling con-

State of the art

tacts can strongly vary with regard to the material pairs used. Typical friction coefficients for DLC coatings of various structures and produced by different coating methods are in the range of 0.05 to 0.2 [Hol09]. The mechanism to produce low friction shear planes for DLCs differs from soft metals (Pb, Ag) and lamellar solids such as MoS₂, with its extremely low shear strength between the atomic layers [Erd04]. The explanation of the low friction for DLC surfaces due to a shear process of the weakly bonded shear planes between the contact interfaces is supported by extensive research and is widely accepted. Mechanisms such as this are very relevant, if both contact partners are DLC covered and no debris accumulation or transfer film build-up occurs. Not only DLC-DLC contact combinations are widely used also a combination of DLC and uncoated steel are common. Due to a rubbing process, the uncoated surface will be covered by a carbon rich mixed oxidized and metal-containing transfer layer.

Aside from the non-lubricated application of DLC coatings and the resulting low friction properties, many DLC material combinations are used in combination with different lubricants. The most ambivalent considered research could be found in the field of lubricated DLC material combinations generating extreme low friction coefficients. The so-called superlubricity refers to sliding between two contacting surfaces whereas the friction literally vanishes [Erd07]. Kano [Kan06] and Barros et al. [Bar07] discovered with their investigation on a ta-C coated system in a pin-on-disc test rig (700 MPa, 30 rpm, 60min and 80°C) ultralow friction values in the superlubricity range. For these test series, they applied the coating to a polished carburized steel disc, whereas hardened and polished bearing steel pins (AISI 52100) were used as counterbody. They obtained ultra-low friction properties in the range of 0.02 by this ta-C/steel combination lubricated with a poly-alpha-olefin (PAO) based oil containing 1% glycerol mono-oleate (GMO).

2.7.4 Zr-based coatings

There is a growing interest in studying other coating systems as an alternative to carbon-based coatings. Zirconium as source material for hard and wear resistant coatings can take different forms of thin films. The best-known tribological relevant examples are:

- Zirconium carbide (ZrC)
- Zirconium nitride (ZrN)
- Zirconium carbonitride (Zr(C,N))

Zirconium carbide is a material with excellent thermal, chemical, electronic and mechanical properties, which could be used to form thin film coatings for tribological applications. Many reports described the deposition of ZrC films by PVD and CVD based techniques [Car07]. The main problems in obtaining high quality ZrC films are the high melting point of 3,445°C, low sputtering or evaporation rates and an affinity for oxygen [Woo06]. Gold et al. investigated the fatigue life of PVD-coated cylindrical roller bearings (NU 206) in a roller bearing fatigue test rig (RLP) lubricated with ester 32 cSt at a load of 16 kN. Aside from coating systems such as tungsten carbide/carbon (WC/C), CrAlN and a-C:H the tests included an

evaluation of wear resistance and fatigue life of ZrC coatings. The amorphous carbon- and hydrogen containing coating presented a graded layer construct (Zr-bonding layer – Zr-interlayer – C-top layer). In comparison to other coating systems the ZrC coatings showed a benefit in the wear resistance of rolling elements after 400 h of test duration [Gol07]. Further information on differently graded ZrC coatings are given by Bobzin et al. in [Mur10]. Manier et al. showed that graded ZrC₉ thin films exhibit also an adequate slip-rolling resistance [Man10-3].

Zirconium nitride coatings can be achieved by employing deposition techniques such as reactive ion beam sputtering or vacuum arc deposition. Thus, two types of coatings can be created, a stable ZrN coating and metastable Zr₃N₄ or ZrN₂ phases. Fields of application for these wear resistant coatings are cutting tools and machine elements in combination with titanium nitride (TiN) coatings [Zhi97]. Thom et al. investigated the wear resistance of PVD coated thin films on 440C stainless steel substrate in a rolling contact fatigue (RCF) test at two Hertzian contact pressures of 4.0 and 5.4 GPa, respectively [Tho93]. They reported an increased RCF life of ZrN by increasing the coating thickness up to 1.00 µm at 5.4 GPa.

Manier et al. showed the positive aspects of Zr(C,N)¹⁰ coatings, like low coefficients of friction, in highly stressed rolling contacts as alternative solution to DLC and ta-C coatings [Man10-2]. Considering specific process parameters, a coating structure with nanolayers below 5 nm could offer a slip-rolling resistance up to 10 million of load cycles in a 2Disc-test rig at average Hertzian contact pressures of 1.94 GPa. Furthermore, Zr(C,N) coatings can offer a reduction in friction of 20% in mixed/boundary lubrication in comparison to uncoated steel/steel contacts [Man10]. For this reason Zr(C,N) coating is selected for further tribological test at higher load regimes.

¹⁰ ZrC doped with approximately 13 wt.-% nitrogen [Man10]

3 Experimental details

3.1 Characterization of testing materials

In previous investigations [Woy09] [Man10] [Man10-3] on the slip-rolling resistance of thin film coatings, the substrates were mainly made of the well-known bearing steels 100Cr6H (OVAKO PBQ, tow-times remelted) and Cronidur 30 (X30CrMoN151). Cronidur 30 is a pressure-nitrided cold working steel with martensitic structure. Due to use of a PESR-process (Pressure Electroslag Remelting) in combination with sophisticated rolling technology, extreme high cleanliness and a homogeneous structure with high durability values can be achieved at a maximum hardness of 60 HRC. Better corrosion and wear resistance can be achieved by partially replacing carbon with nitrogen. Another positive aspect of this steel grade is its high temper resistance up to 500°C. [Ene12]

As mentioned in [Man10], the use of high quality substrate materials, i.e. without segregation or porosity, impurities and defects due to production process, for applications in highly loaded contacts is necessary to ensure the highest possible life time. With regard to a possible coating procedure of the substrates, the selected steel has to withstand temperatures up to 300°C without decreasing its hardness or changing its structural constitution. For that reason, Cronidur 30 with a temperature stability of up to 500°C and another three steel grades were chosen. The use of three alternative steels aside from 100Cr6H and Cronidur 30 is motivated by a third reason, the influence of the mechanical properties toughness and high strength. In order to realize light-weight design strategies, especially in gear components, it is essential to use steels with high toughness and fatigue strength properties. Figure 3-1 illustrates two basic parameters, stated in DIN 3990 part 5, describing the increasing demands on material grades used for gear wheels:

- a. surface hardness of the tooth flank and
- b. core fatigue strength of the tooth root.

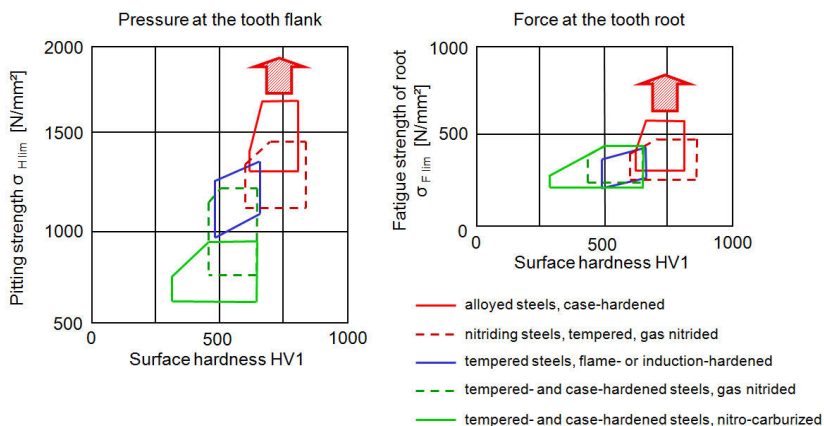


Figure 3-1: New demands on light-weight gear components derived from DIN 3990-5 (1987).

Hence, it is a major task to find a material solution which forms a good compromise between hardness in the tooth contact and ductility as well as basic strength of the tooth base. In consideration of the increased demands on substrate properties (mechanical properties, temperature resistance and excellent quality), two high toughness steels and an aerospace steel of ultra-high toughness were selected for tribological investigations.

In their product spectrum, Aubert & Duval (France) have available steels with special mechanical properties and chemical composition. For the reason of high toughness, values a through hardening steel V300 and a steel for special applications NC310YW were selected. Both steel grades are not considered in literature concerning the tribological behavior. Typical applications for the grade V300 are springs and torsion bars for heavy workloads. NC310YW is designed for various heavily stressed mechanical parts such as gears, transmission shafts and torsion bars [Aub10]. Due to the relatively high tempering temperature, it is possible to deposit PVD coatings without any negative impact on the steel characteristics (see 3.1.2).

Developed by Latrobe Specialty Steel Company (USA) [Lat95], the third steel grade CSS-42L (AMS 5932) is a case carburizable stainless steel alloy, which is capable of achieving very high surface hardness levels and maintaining high hardness at operating temperature up to 427°C. Combining high fracture toughness, hot hardness, metal-to-metal wear resistance and corrosion resistance, while retaining ductility and strength this steel is suited for the use in bearing applications, cams, shafts, gears and bolts. Due to a double vacuum melting process VIM-VAR (Vacuum Induction Melting-Vacuum Arc Remelting) an optimum of control, reproducibility of chemistry, microcleanliness and fatigue resistance can be provided. Tomasello et al. reported a superior ball bearing life time and good wear properties [Tom02]. They recommended the carburized CSS-42L an excellent candidate for severe bearing and gear applications. The life time was tested using 207-sized angular contact ball bearings at maximum contact pressures of 2.758 GPa (rotating inner ring at 5400 rpm). As synthetic lubricant MIL-L-7808H was used at an inlet temperature of 71.1°C. The results were compared to that of 52100 and M-50 steels and showed that none of the CSS-42L inner races failed and exceeded even the predicted 65% confidence limit (Weibull slope of 1.5) for commonly used aerospace bearing alloys. Furthermore, Bhadeshia [Bha12] and Ragen et al. [Rag02] reported very good fracture toughness values. CSS-42L in general belongs to precipitation-hardenable steel alloys. Thus, the formation of Fe-Fe₃C carbides during the heat treatment is suppressed. Additionally the case carburization leads to increased hardness values and possibly avoids the formation of white etching structures (cf. paragraph 2.2.2). However, unfavorable effects are the high costs for the material procurement and further the very complex heat treatment. The mechanical properties of CSS-42L as well as 100Cr6H, Cronidur 30, V300 and NC310YW are summarized in Table 3-1.

The mechanical properties of 100Cr6 as well as 20MnCr5 (1.7147) are determined and considered in detail in the course of a collaborative research center (SFB 570) [SFB09].

Experimental details

Table 3-1: Mechanical properties and tempering temperatures of steel grades used

Material	100Cr6H (AISI 52100)	Cronidur 30 (AMS 5898)	V300 (1.8062)	NC310YW (40SiNiCrMo10)	CSS-42L (AMS 5932)
Density ρ [g/cm ³]	7.8	7.67	7.8	7.66	7.93
Young's Modulus E [GPa]	210	213	198	202	211
Strain [%]	n.d.a.	< 5	10	9	< 18
Hardness [HRC]	~ 63	~ 60	~ 51	~ 57	~ 63
Fracture Toughness K _{IC} [MPa*m ^{1/2}]	16.5	21	80	52	> 120
Charpy Toughness KV [J]	n.d.a.	n.d.a.	10	30	n.d.a.
Ultimate Strength R _m [MPa]	~ 2300 (for 61 HRC)	~ 2300	~ 1600	~ 2150	~ 1840
Maximum Service Temperature [°C]	150	475	410	300	552

n.d.a. – no data available yet

3.1.1 Chemical analysis

In case of V300, NC310YW and CSS-42L, the composition of the steels is measured by Optical Emission Spectroscopy (OES). These values are compared with the standard and supplier specification and presented in Table 3-2. It is clearly visible from the chemical analysis that CSS-42L refers to cobalt-base alloys with 12 wt.-%. The special feature of V300 and NC310YW is the high silicon content up to 2.3 wt.-%. As mentioned above, Cronidur 30 contains 0.2 wt.-% of nitrogen as alloying element for a better corrosion and wear resistance.

Table 3-2: Chemical composition of the steel grades (wt.-%)

Material	C	Si	Mn	P	S	Cr	Cu	Mo	Ni	N	V	Co	W	Nb	
100Cr6H	Standard specifications	1.00	0.25	0.35		1.50									
Cronidur 30	Standard specifications	0.25 – 0.35	0 – 1.00	0 – 1.00		14.00 – 16.00		0.85 – 1.10	0 – 0.50	0.30 – 0.50					
	WDX	0.38	0.62	0.24		15.57		1.00	0.12	0.24					
V300	Standard specifications	0.42 – 0.50	1.30 – 1.70	0.50 – 0.80	< 0.025	< 0.025	0.50 – 0.80	0.20 – 0.30			0.40 – 0.80	11.00 – 14.00	< 0.25	0.01 – 0.05	
	OES	0.48	1.35	0.65	< 0.001	< 0.001	0.62	0.03	0.23		0.64	> 12.00		0.03	
	Supplier specifications	0.461	1.48	0.65	< 0.009	< 0.0015	0.62	0.03	0.22	0.11		0.62	12.43	0.02	0.02
NC310YW	Standard specifications	~ 0.40	~ 2.70			~ 0.85		~ 0.40	~ 1.75		~ 0.20				
	OES	0.42	2.32	0.68	< 0.001	< 0.001	0.82	0.02	0.40	1.88		0.20			
	Supplier specifications	0.414	2.68	0.65	0.005	< 0.0015	0.83		0.41	1.83		0.22			
CSS-42L	Standard specifications	0.10 – 0.25	< 1.00	< 1.00	< 0.020	< 0.010	13.00 – 16.00	< 0.10	3.00 – 5.00	1.75 – 2.75	0.40 – 0.80	11.00 – 14.00	< 0.25	0.01 – 0.05	
	OES	0.13	0.14	0.16	0.002	< 0.001	13.90	0.04	5.36	2.04		0.64	> 12.00		0.03
	Supplier specifications	0.13	0.13	0.17	0.010	0.003	13.89	0.04	4.80	2.03		0.62	12.43	0.02	0.02

3.1.2 Heat treatment

All of the different materials were firstly machined from a steel rod to give them their basic form. After machining, the raw material a special customized heat treatment for each material was carried out (cf. Figure 3-2). The course of heat treatment for CSS-42L is exemplarily described above with an effective case hardening depth of 0.94 mm at 595 HV.

- Hydrogen activation pre-oxidized at 954°C for 30 minutes
- Vacuum carburization at 915°C to target an effective case depth of 0.889 – 1.016 mm
- Vacuum stress relief annealing at 593°C for four hours and nitrogen cooling to 160°C
- Vacuum austenitization at 1121°C for 30 minutes followed by a 20 bar nitrogen quenching
- Two times deep freezing to -196°C followed by a tempering treatment at 552°C for five hours respectively

For the other steel materials no carburization treatment has been applied. A subzero cooling during the heat treatment to -75°C – -90°C is the main common feature of 100Cr6H, Cronidur 30 and NC310YW in order to remove the unwanted retained austenite.

Table 3-1 shows the hardness values reached after the heat treatment. The heat treatment of Cronidur 30 is listed by Manier in [Man10].

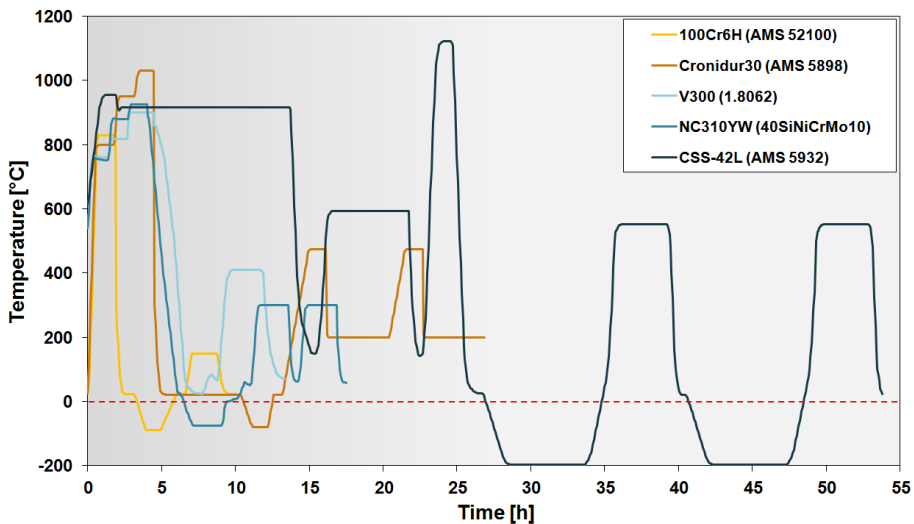


Figure 3-2: Schematic heat treatment curve of the 100Cr6H, Cronidur 30, V300, NC310YW and CSS-42L materials

After being heat treated, the blanks have been finally finish-grinded to their final dimension (spherical and cylindrical). The spherical discs were grinded with machining scores along the circumference and the cylindrical discs were super polished on their outer surface. The

Experimental details

effect of superfinished steel surfaces, i.e. gear teeth, is considered in literature as very positive to increase the load carrying capacity [Kra00]. The roughness values after machining are represented in Table 3-3. In previous investigations, the polished surfaces of the machined steel batches were protected by a multifunctional spray (Technolit WL-50). As some unfavorable effects of the spray on the coating processes have been detected, this treatment of the steel samples is no longer applied. The only preventive action is the storage of the substrates in desiccators to prevent them from any water condensation and corrosion.

Table 3-3: Typical roughness values of polished, cylindrical and grinded, spherical steel samples

Material	100Cr6H (AISI 52100)	Cronidur 30 (AMS 5898)	V300 (1.8062)	NC310YW (40SiNiCrMo10)	CSS-42L (AMS 5932)
R _{a cyl.} [μm]	0.0038	0.0034	0.0048	0.0047	0.0114
R _{z cyl.} [μm]	0.0267	0.0256	0.0314	0.0325	0.0763
R _{pk cyl.} [μm]	0.0074	0.0066	0.0079	0.0070	0.0114
R _{a sph.} [μm]	0.346	0.300	0.170	0.276	0.157
R _{z sph.} [μm]	2.458	2.080	1.300	1.953	1.289
R _{pk sph.} [μm]	0.380	0.288	0.213	0.325	0.149

3.1.3 Structure and hardness

The structural quality of steels was examined after receiving the samples from the heat treatment. The cross sectional structures of the samples were polished and etched followed by a light microscopy investigation and determination of micro-hardness (HV 0.2) depth profiles from the surface (in case of CSS-42L HV 0.5).

Analyzing the sectional structure of 100Cr6H (Figure 3-3 a) and Cronidur 30 (Figure 3-3 c) in both steels a martensitic structure can be found. Due to the forming process during steel production unresolved carbides appearing partially line shaped, see white arrows Figure 3-3 b.

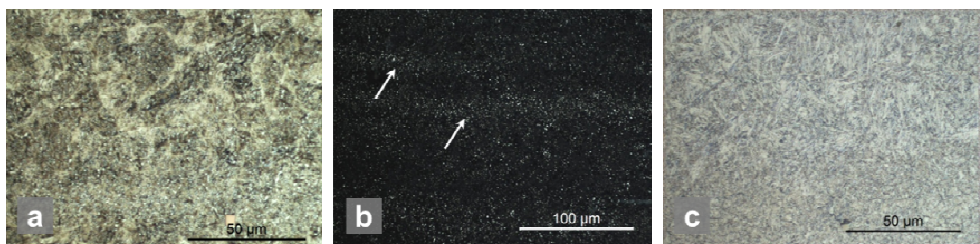


Figure 3-3: Microstructures of (a) 100Cr6H (etchant: Nital), (b) carbide structure 100Cr6H (etchant: sulfuric acid) and (c) Cronidur 30 (etched by Energietechnik Essen, scale: a, c) 50 μm and b) 100 μm)

The structural composition of V300 and NC310YW is specified by the supplier as entirely martensitic and can be confirmed by the first microscopy investigation Figure 3-4. In the course of this work the structures of both steels grades will be examined more detailed. The average hardness of V300 is determined with values of 530 HV 0.2 and for NC310YW of

631 HV 0.2. Following the metallographic characterization the content of retained austenite was quantified by means of X-ray diffraction (XRD). In case of V300, the analysis showed amounts below detection limit (~2.5 vol.-%). NC310YW reveals an residual austenite of content of ~5.2 vol.-%.

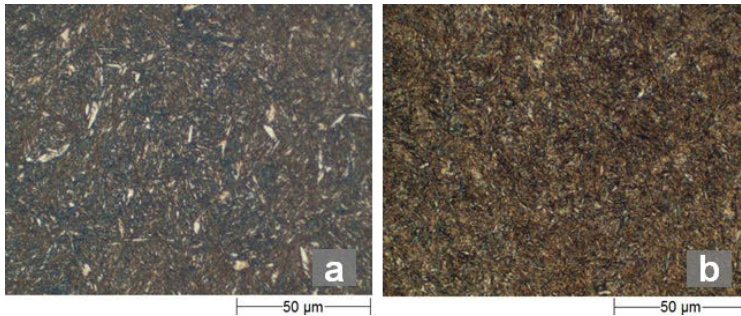


Figure 3-4: Structural composition of (a) V300 and (b) NC310YW (etchant: Nital, scale: 50 µm)

The microstructure of CSS-42L is typical for carburized and heat treated steels. Three distinct regions can be observed in the microstructure. Hetzner and van Geertruyden [Het08] investigated the crystallography and metallography of different carbides in high alloy steels including CSS-42L as well. By etching the first region, Figure 3-5 a, a tempered martensitic structure with a large volume fraction of carbides becomes visible. The etchant (HNO_3) did not affect the carbide structure which appears as white microconstituents. Hetzner identified these carbides as Me_{23}C_6 by means of electron backscatter diffraction (EBSD). The transition zone between the carburized case and core, Figure 3-5 b, entirely consists of austenite (bright areas). The core area is found to be almost completely martensitic with containing partial austenitic areas (Figure 3-5 c). Considering the hardness of CSS-42L, a typical depth profile is shown in Figure 3-6. Starting with approximately 790 HV 0.5 in a carburized zone, the transition zone offers a hardness value of 320 HV and in the core zone a value of 550 HV can be found. Thus, measured hardness is in the field of given supplier data. The content of retained austenite is specified with ~3.2 vol.-% in carburized area (Figure 3-5 a).



Figure 3-5: Microstructure of CSS-42L: a) Me_{23}C_6 carbides including martensitic case, b) transition zone below carburized case and c) core (etchant: HNO_3 and Marble, scale: a), c) 50 µm and b) 500 µm)

Experimental details

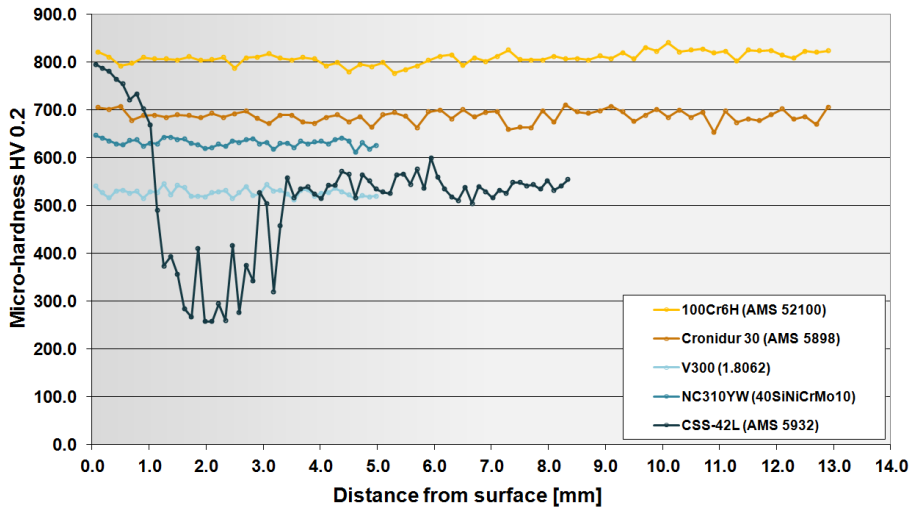


Figure 3-6: Hardness depth profiles (HV 0.2) of steels used

3.2 Investigated coating systems

Two main types of coating systems were investigated in the present study. The Zr(C,N)¹¹ coatings were all deposited at Tekniker Technological Center (Eibar, Spain) in an industrial coating installation by Cathodic Arc Plasma Deposition (Arc-PVD). This method contains two deposition techniques, the arc evaporation and the plasma ion plating. During the coating process the steel substrates act as anode and the pre-cleaned and de-oxidized single Zr-target as cathode. After activation of the arc on the whole surface of the cathode, the evaporation of the targets starts. The evaporated material migrates through the plasma of argon and is ionised. Using N₂ and C₂H₂ as reaction gases the Zr reacts to the coating material ZrN and Zr(C,N). By applying a negative polarization to the substrate, called bias, the ionized material is finally deposited on the substrate. Recent investigations according to the slip-rolling resistance of Zr(C,N) coatings revealed a considerably better resistance of a process controlled nanolayer (pcnl) coating. In order to achieve this type of coating a number of process optimizations and investigations were analyzed. Using a single Zr-target in combination with a continuously rotating planetary system, where the substrates are mounted, results the coating properties desired. Figure 3-7 clearly shows the different coating structures of a slip-rolling resistant process controlled nanolayer structure (left) and a structure with poor slip-rolling resistance.

In order to characterize the composition of the coating EDX, WDX as well as Auger electron spectroscopy (AES) depth profile analysis were performed. The results of the quantitative analysis of this coating type aside from zirconium (~48.1 % atomic concentrations) are nitrogen (~47.08 %), carbon (~4.82 %) and oxygen.

¹¹ A complete characterization of their properties including their deposition parameters can be found in [Man10]

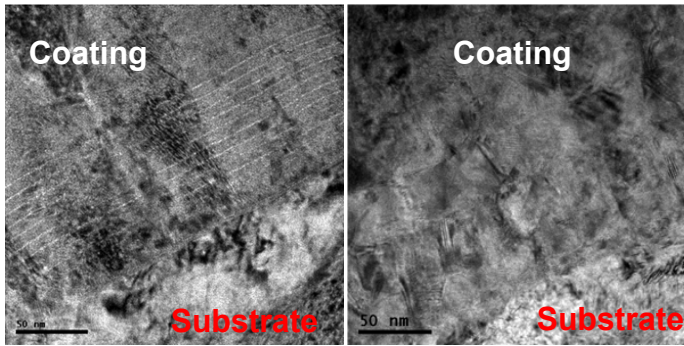


Figure 3-7: TEM analysis of the interface between steel substrate and Zr(C,N)-coating: pcnl structure (left) and conventionally deposited structure (right) [Man10] (scale: 50 nm)

The DLC coatings applied were developed and deposited at the BMW Group (Munich), consisting of different adhesion layers and a functional layer. A SIMS measurement of a BMW coating (shown in Figure 3-8) reveals different chemical compositions and the structural positions of the layers. Starting with a chromium-based adhesive layer and an W-C:H interlayer the functional layer is a hydrogenated amorphous carbon coating doped in some configurations with nitrogen or silicon (a-C:H, a-C:H:-N, a-C:H-Si). Further information concerning the deposition process and coating properties can be found in [Man10]. Doping the coatings with non-metallic elements such as nitrogen and silicon influences special properties of the coatings, for example the surface energy. Heat resistance, translucency, color and ultraviolet resistance are examples for manipulating mechanical and chemical properties with dopants [VDI05].

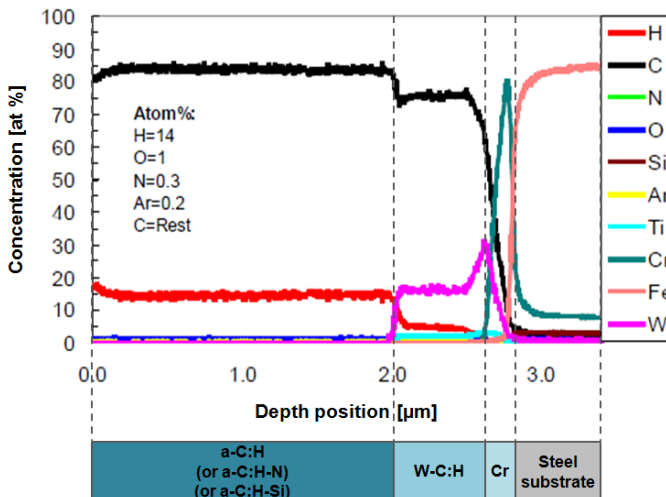


Figure 3-8: SIMS measurement of a used a-C:H type DLC coating (BMW 4) performed at Fraunhofer IST Braunschweig

Experimental details

During the development process of the coatings, some process parameters, i.e. the inter-layer and film thickness, were modified by BMW in order to get the best coating in practice. That is why several coatings from this supplier can be found. AFM topographic studies of the coatings BMW 4 and BMW 4 revealed distinct differences in the surface conditions (see Figure 3-9). Both coatings showed bumpy surfaces. In case of BMW 4 the surface structure appears incomplete compared to the DLC-typical structure of BMW 11. More particularly, it seems that the coating process and hence the layer growth was interrupted. Furthermore, scratches on the substrate surface due to the mechanical finishing process are easily recognizable despite an applied coating (cf. Figure 3-9 BMW 4 AFM image 2D 9 x 9 μm).

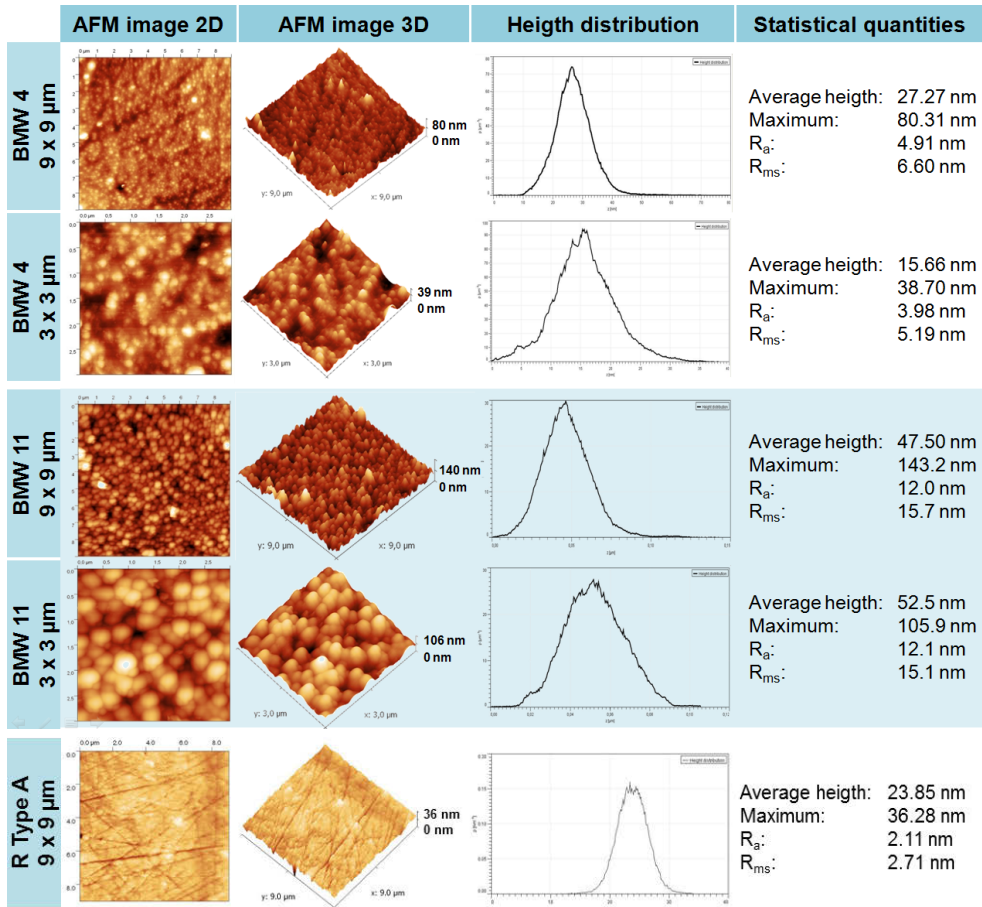


Figure 3-9: Structural characterization of coatings BMW 4, BMW 11 and KYB Type A by atomic force microscopy

There is a specific interest in pure carbon coatings, especially ta-C, for sliding components, especially for automotive application on engine and gear components, because of its potential to very low friction and even superlubricity [Kan06] [Mat08]. For this reason coatings of

a-C and ta-C type are chosen in order to compare this film types with BMW and Tekniker coatings mentioned before. The deposition of Fraunhofer IWS (Dresden) ta-C and a-C coatings was carried out by a vacuum-arc evaporation using a pulsed arc discharge from a graphite cathode. Eight batches V1-V8 were prepared. The types V1, V4, V5, V6 and V8 can be classified as ta-C, whereas V2, V3 and V7 belong to the category a-C according to the VDI guideline 2840 [VDI05]. The versions V1-V3 were deposited by mechanically triggered pulsed arc and the types V4-V8 by laser-controlled pulsed arc. For this purpose the laser-arc system LAM400 developed by Fraunhofer IWS was used. The slip-rolling resistances of the previous ta-C and a-C-types in comparison to V1 (designated as G3) are described in [Woy10]. Prior to deposition, Chromium-ion etching was performed by using a metal dc-arc source. For the types V5 to V8 an additional hollow-cathode Argon-ion etching was performed before metal ion etching. Ion etching was followed by deposition of a thin (30 – 50 nm thick) Cr interlayer using the same dc-arc source and deposition of the carbon layer by pulsed (laser) arc. The maximum temperature during the deposition process was about 150°C due to plasma heating. The temperature during carbon deposition amounted to about 120°C. The differences of coating types were obtained by different ion energies varying the substrate potential and/or the Ar-gas pressure during deposition.

Japanese company KYB Corp. provides two types of coatings: Type A classified as a-C:H typically used for motor cycle shock absorbers. The same applies for the second KYB thin film, Type B, which belongs to the chromium doped a-C:H coatings. Specified by the manufacturer a higher slip-rolling resistance even at high Hertzian contact pressures can be expected from KYB Type B. Coating Type A is designed for technical applications with low contact pressures.

Table 3-4 summarizes the thin film properties measured, the coating type and the deposition process of the industrial coating systems tested in this work.

Table 3-4: Properties of the different DLC and Zr(C,N) coating systems tested

Supplier	Coating name	Coating type	Coating thickness [μm]	Adhesion layer	Process type	Hardness [GPa]	Young's Modulus [GPa]
IWS	V(1-8)	ta-C/a-C	2.0 - 3.0	Cr	PVD	19 - 63	125 - 606
BMW	BMW (4, 11)	a-C:H	1.0 - 5.6	Cr/CrN/W-C:H	PECVD	12 - 25	135 - 214
Tekniker	K(1-10)	Zr(C,N)	~ 3.0		Arc-PVD	~ 26	~ 340
KYB	Type A	a-C:H	1.0	Cr-C	PVD	13	139
	Type B	a-C:H:Cr	2.0	Cr-C	PVD	23	186

3.3 Twin disc testing machines

All tribological slip-rolling investigations were carried out on an Amsler-type machine and on an Optimol 2Disc tribometer, which was designed in 2008. Originally developed for simulation processes of wheel-rail contact researches, twin disc testing machines offer an optimal basis for experiments in combination with the selected surface roughness to operate in the mixed boundary lubrication regime. Nowadays, new twin disc machines can be used for the characterization of tribological systems with slipping, sliding and rolling motion. Modeling the working conditions and contact configuration of gear teeth in contact and ball bearings, these testing machines are widely spread.

3.3.1 Amsler tribometer (A135)

In the Amsler tribometer two discs with the same diameter roll against each other on their cylindrical surface. Using a single electrical motor and several coupling shafts, which ensure the mixed boundary lubrication regime at the start, the rotation speed is fixed at 390 rpm. To enable a continuous slip of 10%, the second disc, applied as counter body, is driven at a speed of 354 rpm. The exact sample configuration in this tribometer is shown in Figure 3-10.

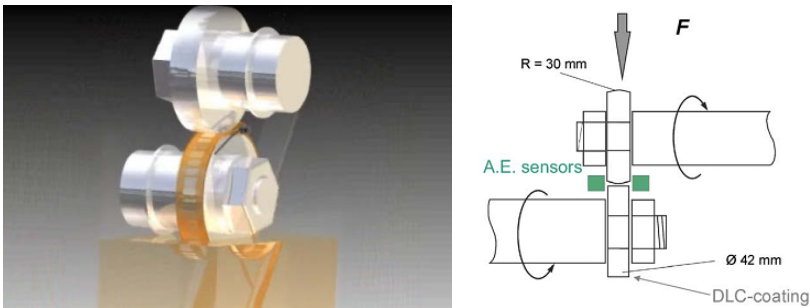


Figure 3-10: Sample arrangement in the Amsler type tribometer

The geometry of the discs with an outer diameter of 42 mm generates a contact configuration of the ball-cylinder type. In the present experiments of this work, the top, ball-shaped counter discs were mainly uncoated and only pre-polished or grinded. The lower, cylindrical discs were used in coated state as well as uncoated with a super polished surface. A normal force is applied by means of a spring, leading to a normal force up to 2,000 N (initial average Hertzian contact pressure $P_{0\text{mean}} = 1.94$ GPa) in the contact point (see Table 3-5). The stiffness of the spring with 14,650 N/m and lever action of the counterbody holder presses the disc against each other. By controlling the compression of the spring the normal force can be adjusted in steps of 50 N. For comparison, an average contact pressure of 1.25 GPa corresponds to a maximum Hertzian contact pressure of $P_{0\text{max}} = 1.875$ GPa, which is equivalent to load stage 12 in the FZG test rig. According to the international standard ISO 14635-1, this load stage is the most demanding test procedure for gear components.

In order to create experimental conditions as close as possible to real applications, the bath temperature of the oil is set at 120°C. For security reason the temperature is controlled by a second thermal sensor couple with a programmable relay, taking down the temperature, if it exceeds 140 °C. The lower cylindrical disc dips into the heated oil reservoir and drags the lubricant into the contact due to the rotation.

During the tests the friction torque can be measured by the axial torque of the lower shaft rotating with 390 rpm with use of a pendulum as well as a planetary gearing coupled with the mentioned axis. The coefficient of friction (COF) can be evaluated with the following equation:

$$\mu = M/(F_N \cdot r) \quad (3.1)$$

In this equation M is the friction torque in Nm, F_N the applied normal force in N and r the radius of the driven sample in m. The deflection of the pendulum is translated into a translation movement for the measurement of the corresponding torque scale. A Linear Variable Differential Transformer (LVDT) permits the transduction of this movement into an electrical signal and records directly the COF. [Man10]

Table 3-5: Experimental conditions

Conditions	Parameter
Dimensions of the discs	Diameter: 42 mm; Width: 10 mm
Contact	Grinded/ polished curved disc (radius of curvature: 21 mm) against uncoated/ coated super polished cylindrical disc
Substrate	100Cr6H, Cronidur 30, V300, NC310YW, CSS-42L
Type of motion	Rolling with a fixed slip rate of 10%
Initial average Hertzian pressure P_{0mean}	1.5 – 2.62 GPa ($F_N = 930 – 5,000$ N)
Rotation at speed	390 – 354 rpm
Sliding speed V_{diff}	0.08 m/s
Load cycles n_{tot}	Up to 10^7 or rupture (damaged surface area of >1 mm ²)
Effective sliding distance	Up to 132 km
Ambient temperature	120 °C oil bath temperature
Lubricants	BMW FF SAE 0W-30 'VP1', Polybutylene Glycol 'B20'

3.3.2 Optimol 2Disc tribometer

The experimental setup in the newly designed Optimol 2Disc tribometer generates similar to Amsler type tribometer a ball-cylinder contact mechanism using the same test samples. Designed for very high normal forces up to 5,000 N for testing the behavior of thin film coatings and their substrates under extreme conditions, this tribometer applies average contact pressures up to 2.62 GPa. Table 3-6 summarizes the normal forces with the corresponding Hertzian contact pressures (P_{0mean} , P_{0max}) and total deformation values of both samples.

Experimental details

Table 3-6: Hertzian contact pressures for the sample geometries tested

Normal force [N]	930	2,000	4,400	5,000
$P_{0\text{mean}}$ [GPa]	1.5	1.94	2.5	2.62
$P_{0\text{max}}$ [GPa]	2.25	2.91	3.75	3.92
Total deformation/ flattening [μm]	13.4	21.2	37.8	41.2

The test rig is powered by two electric motors, which rotate independently of each other. Thus, the slip rate of the two discs as well as rotation speed is freely adjustable driven by an integrated computer control unit. In order to ensure the comparability and consistency of the test results obtained on both test machines, the experimental conditions (rpm, slip rate, lubrication, temperature) are always kept identical, with the exception of the Hertzian contact pressure. As shown in the test arrangement (c.f. Figure 3-11), the samples are positioned on the same vertical level, whereas the load application is induced by an electrical servomotor. This servomotor compresses a spring fixed between motor and axle of the cylindrical disc. It thereby adjusts the previously set normal force.

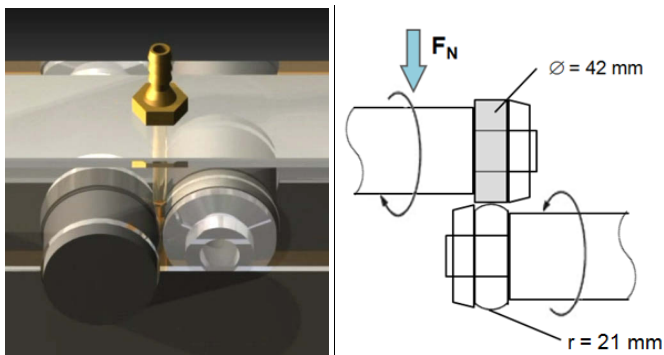


Figure 3-11: Configuration of the test samples on an Optimol 2Disc tribometer

The test software is designed to measure the friction force as well as wear rates of both samples and plot it in situ. In contrast to the Amsler type tribometer the test sample do not dip into the oil reservoir. The oil is fed by a gear type pump within a circular flow into the contact point of both samples.

3.3.3 Lubricant properties

In previous BAM studies i.e. [Man10], unadditivated paraffin oil ISO VG 46 was taken as lubricant for the tribological tests at room temperature to avoid the influences of EP/AW (Extreme Pressure/Anti Wear) and FM (Friction Modifier) additives. With regard to the poor stability at a temperature up to 120°C, paraffinic oil was replaced by fully formulated factory fill engine oil SAE 0W-30 (ACEA A3/B4¹², HTHS = 2.98 mPa·s) used at the BMW Group

¹² ACEA A3/B3 oils are designed for general usage use in a wide range of gasoline and light duty diesel engines. ACEA A3/B3 oils are typically used in older vehicles as they do not provide the minimum performance demanded by the latest OEM specifications. [Lub12]

(Table 3-7). In selecting this oil, tests can be carried out at more representative conditions of today's lubricated engine or power train components.

Containing more additives as paraffinic oil, it is one part of the following investigations to analyze and understand the interactions between different types of surfaces and the lubricants. In order to meet the emerging or already existing regulations concerning the environmental impact of lubricants, a fully hydrocarbon soluble polybutylene glycol (PBG)¹³ named B20 was used as second in some respects as reference oil. However, one of the future targets for PBG B20 as ash, metal- and polymer-free lubricant is to fulfill the requirements of the ACEA C4¹⁴ specification.

Table 3-7: Viscosimetric properties of engine oil SAE 0W-30 VP1 and Polybutylene Glycol B20 [Sch06]

	BMW FF SAE 0W-30 'VP1'	Polybutylene Glycol 'B20'
Viscosity Index	168	133
Pour Point [°C]	-57	-37
$\eta_{100^\circ\text{C}}$ [mPa·s]	8.04	
$\eta_{150^\circ\text{C}}$ [mPa·s]	3.34	
$\nu_{40^\circ\text{C}}$ [mm ² /s]	57	66.12
$\nu_{100^\circ\text{C}}$ [mm ² /s]	10.2	9.91
$\nu_{150^\circ\text{C}}$ [mm ² /s]	4.42	5.43
HTHS [mPa·s]	2.98	3.61
$\alpha_{p80^\circ\text{C}}$ [GPa ⁻¹]	14.17	
$\alpha_{p150^\circ\text{C}}$ [GPa ⁻¹]	11.9	

3.3.4 Failure criterion, test abort criterion

The failure criterion of thin film coated steel substrates has led to many discussions in the recent literature. Liu et al. proposed the total removal of the coating inside the wear track as failure criterion in a ball-on-flat test rig [Liu07]. Protecting the substrate material against wear as long as possible, a damaged coating cannot fulfill its task, if the damaged surface is bigger than the contact area. Therefore a new failure criterion was established. A damaged area of 1 mm², corresponding to the size of the Hertzian contact ellipse at an average contact pressure of 1.5 GPa, was chosen as criterion to stop the test. In case of slip-rolling tests with uncoated systems, the same criterion was used after the occurrence of pitting on the surface. The development of the COF and the wear volume cannot be as easily assessed as this 1 mm² criterion for a critical damage. Previous tests have shown that the rise in the COF is not necessarily caused by a failure of the coating. However, an increase in roughness values lead to an increased coefficient of friction. It might occur that a certain coating is damaged in several locations leading to a total damaged area larger than 1 mm²

¹³ precise description of PBG: polybutylenglycol monobutyleneether

¹⁴ ACEA C4 oils are high performance lubricants with lower sulphated ash, phosphorus and sulphur contents. They are designed for use in high performance gasoline and light duty diesel engines where advanced aftertreatment systems such as Diesel Particulate Filters (DPFs) and Three Way Catalysts (TWC) are used. [Lub12-2]

Experimental details

but examined individually, these damages are smaller than 1 mm^2 . Such systems would still count as resistant to slip-rolling, as long as none of the single damages exceeds the criterion. [Spa04]

Generally, the slip-rolling tests were run until 10 million load cycles, if the coating or the substrate did not fail (Table 3-5). Increasing the number of cycles from 1 million up to 10 million the duration of the endurance tests corresponds to 18 days at 390 rpm, running non-stop. The vast metallurgical development and numerous practical experiences of recent years have forced to increase the number of load cycles as well as to increase the contact pressure. With 430 hours at 120°C , it also includes a kind of oxidation aging for the engine oil.

4 Experimental results

4.1 Slip-rolling tests

Using 100Cr6H and Cronidur 30 as substrate materials for slip-rolling tests of various thin film coatings, an impressive number of results are collected in recent investigations [Man10] [Man10-3] [Spa04]. As it has already been stated in Table 3-1 and Table 3-4 the number of steel substrates and coating variations induces many possible combinations for slip-rolling tests. Therefore, the tests of slip-rolling resistance, frictional behavior and wear rates are divided for reasons of clarity into three major parts:

- Slip-rolling reference tests of uncoated, self-mated steel pairings und standard testing conditions (Table 3-5) with increasing Hertzian contact pressures
- Slip-rolling tests of coated vs. uncoated samples under standard test conditions with increasing Hertzian contact pressures
- Slip-rolling tests of DLC coated vs. DLC coated samples under standard test conditions at a Hertzian contact pressure of $P_{0\text{mean}} = 1.5 \text{ GPa}$

The tests should reveal which system used in the three mentioned parts above shows the best test results with respect to slip-rolling resistance, coefficient of friction and wear rates. The question of whether or not the application of an expensive and in quality assurance hard to handle thin film coating is of advantage will be considered more clearly in comparison to the reference test with uncoated steel pairings.

4.1.1 Slip-rolling reference tests of uncoated steels

First of all, reference tests were necessary to investigate a possible positive or negative effect of applying a coating on a cylindrical disc. Therefore, the samples were all tested under the aforementioned conditions without any coating and self-mated. Starting with a Hertzian contact pressure $P_{0\text{mean}} = 1.5 \text{ GPa}$, further tests were carried out in four load stages up to 2.62 GPa. Following the tests, optical microscopy images were taken of the wear track generated under the applied Hertzian contact pressure. In order to consider the performance of different coating types and uncoated steels, the evaluated wear rates and coefficients of friction at the beginning and at the end of tests, respectively are used as tribological assessment. Figure 4-1 recapitulates the morphologies of the wear tracks on the cylindrical test sample and on its respective spherical counter body at four different load stages. In case of steels 102Cr6¹⁵, 100Cr6H and NC310YW the tests at 2.62 GPa contact pressure were not conducted due to failures on the steel surface at a lower load stage. All pictures are engendered after the upper testing limit of 10 million load cycles or in the occurrence of the failure criterion (damaged area > 1 mm²).

¹⁵ lower quality steel 102Cr6 (1.00 wt.-% carbon, 1.5 wt.-% chromium) used for comparison purposes to the high quality steel grade 100Cr6H

Experimental results

Material	1.5 GPa (930 N)		1.94 GPa (2,000 N)		2.5 GPa (4,400 N)		2.62 GPa (5,000 N)	
	Counter Body	Test Sample	Counter Body	Test Sample	Counter Body	Test Sample	Counter Body	Test Sample
102Cr6 subzero treated	10 ⁷ cycles		10 ⁷ cycles		10 ⁷ cycles			
100Cr6H	10 ⁷ cycles		10 ⁷ cycles		10 ⁷ cycles			
Cronidur 30	10 ⁷ cycles		10 ⁷ cycles		10 ⁷ cycles		10 ⁷ cycles	
V300	10 ⁷ cycles		10 ⁷ cycles		10 ⁷ cycles		2.18 · 10 ⁸ cycles	
NC310YW	10 ⁷ cycles		10 ⁷ cycles		1.26 · 10 ⁶ cycles			
CSS-42L	10 ⁷ cycles		10 ⁷ cycles		10 ⁷ cycles		10 ⁷ cycles	

Figure 4-1: Optical light microscopy photographs of the typical wear tracks of rolling steel/steel contacts displaying their morphology at different load stages, $P_{0mean} = 1.5, 1.94, 2.5$ and 2.62 GPa (scale: $500 \mu\text{m}$ respectively $1000 \mu\text{m}$ for all pictures)

- **Test results at $P_{0mean} = 1.5$ GPa ($F_N = 930$ N)**

Applying a normal force of 930 N in the first load stage of slip-rolling tests it is obvious on the light microscopy pictures that the cylindrical test sample as well as the spherical counter body were relatively undamaged. Microcracks, scuffing and pitting phenomena have not been established by optical microscopy. Apparently, the motor oil VP1 used avoids such failures due to its additive packages protecting the two surfaces in contact. Under identical testing conditions Manier found microcracks in the scale of about 20 to $100 \mu\text{m}$ on the superpolished Cronidur 30 surface [Man10]. This appearance could not be confirmed in the new test series of this work. All material pairings achieved the maximum number of load cycles (10 million cycles).

The quantification of the volumetric wear rates of the steel samples were taken into account following the test as tribological criterion. Four profiles on each sample were taken by tactile profilometry perpendicular to the sliding direction spaced, at an angle of 90° (cf. Figure 4-2). The measured average worn surface W_q permits the calculation of the volumetric wear rate k_v by following equation:

$$k_V = \frac{V}{F_N \cdot L} = \frac{\overline{W}_q \cdot 2 \pi r}{F_N \cdot n \cdot 2 \pi r} \quad (4.1)$$

In this equation, V represents the worn material volume, F_N the applied normal force and L the distance run under sliding. Due to the low depth of the track, the wear volume V is equal to the planimetric wear surface W_q multiplied by the circumference of the sample.

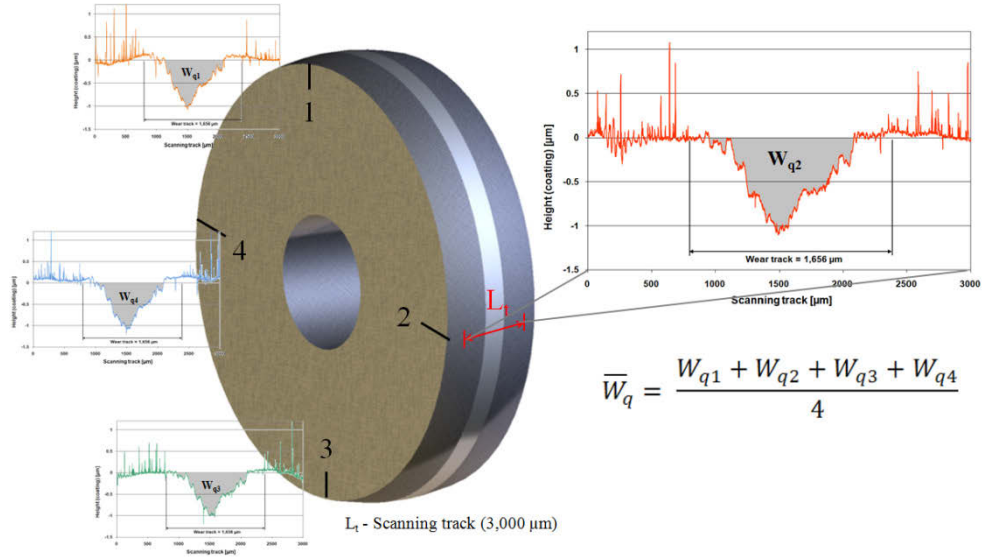


Figure 4-2: Evaluation of the planimetric wear surface W_q by tactile profilometry

As in all cases, the steel sample surfaces were relatively undamaged after the tests, wear can only be found within the wear track. The results of the calculated volumetric wear of all uncoated test pairings conducted at $P_{0\text{mean}} = 1.5$ GPa (up to 2.62 GPa) are illustrated in Figure 4-3. Clearly visible is that the wear rates of the counter bodies are nearly in the same range. Considering the worn surface of the superfinished, cylindrical test samples, the case carburized CSS-42L exhibits a very low wear rate with $1.81 \cdot 10^{-10}$ mm³/Nm. At lower contact pressure it became obviously that the cylindrical discs revealed lower wear rates in comparison to the spherical counterbodies. Increasing the load on the test samples the wear rates of the spherical discs becoming closer to the values of the cylindrical discs.

Experimental results

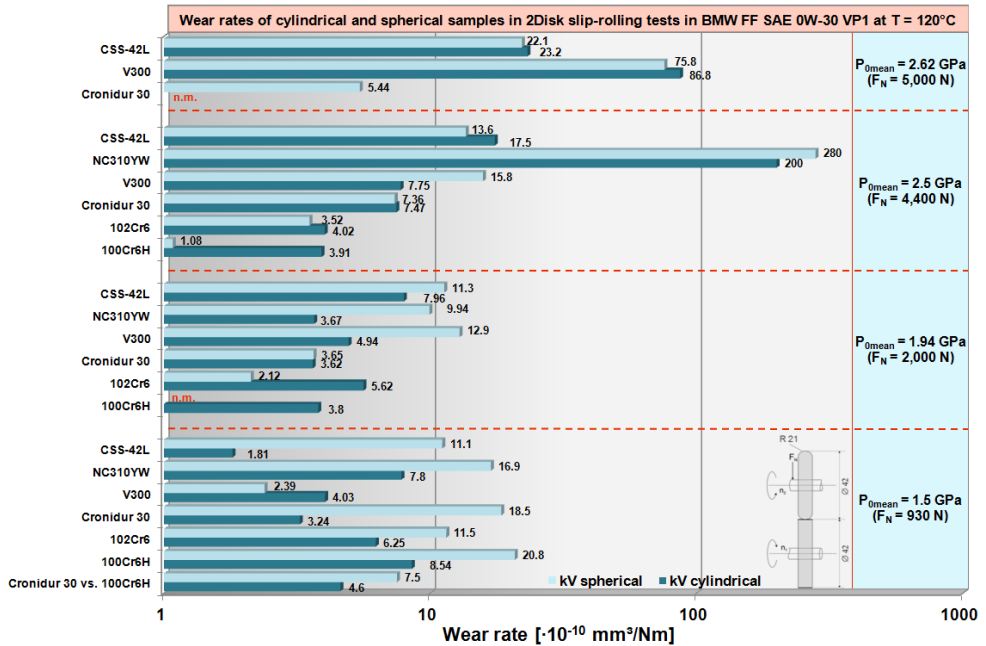


Figure 4-3: Comparison of wear rates of different uncoated steel pairings following the tests in BMW FF SAE 0W-30 VP1 at T = 120°C

Thus, it appears that the carburized edge layer apparently produces a wear protection at low contact pressures. Analyzing the wear tracks by scanning electron microscopy (Zeiss Gemini Supra 40, BAM 6.8) it was underlined that no obvious failures on the surface of the high toughness steels can be detected (Figure 4-4). At higher magnification, only the steel NC310YW showed some uncritical microcracks transversally to the rolling direction in the scale of 4 to 10 μm . Due to the rolling stress, several microcracks along the included carbides of CSS-42L became visible on the surface (see Figure 4-4 c)

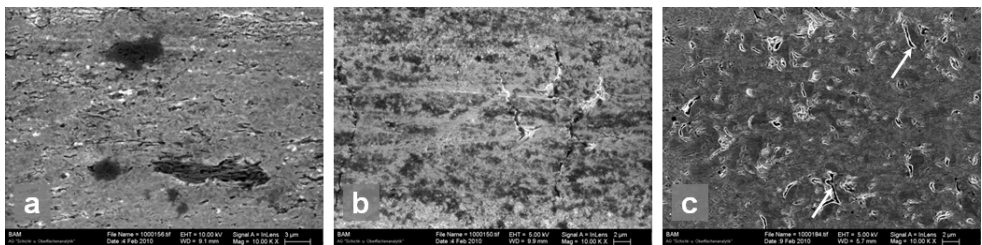


Figure 4-4: SEM images of the wear tracks of the steels a) V300, b) NC310YW and c) CSS-42L stressed at 1.5 GPa (scale: a) 3 μm , b) and c) 2 μm)

Figure 4-5 presents the coefficients of friction at test beginning and end. A first glance shows only one striking difference between the different materials. Whereas the coefficients of friction at test end of the commonly used steels 100Cr6H (102Cr6) and Cronidur 30 as

well as the alternative steels NC310YW and CSS-42L are ranged between 0.06 and 0.083 the high toughness steel V300 revealed a very low friction coefficient of 0.047. In order to exclude any measurement errors or other influences resulting in low friction coefficients, a repeating test under same conditions was conducted with similar test result. The coefficient of friction in the repeating test could be reduced to 0.041 over the test duration of 10 million cycles.

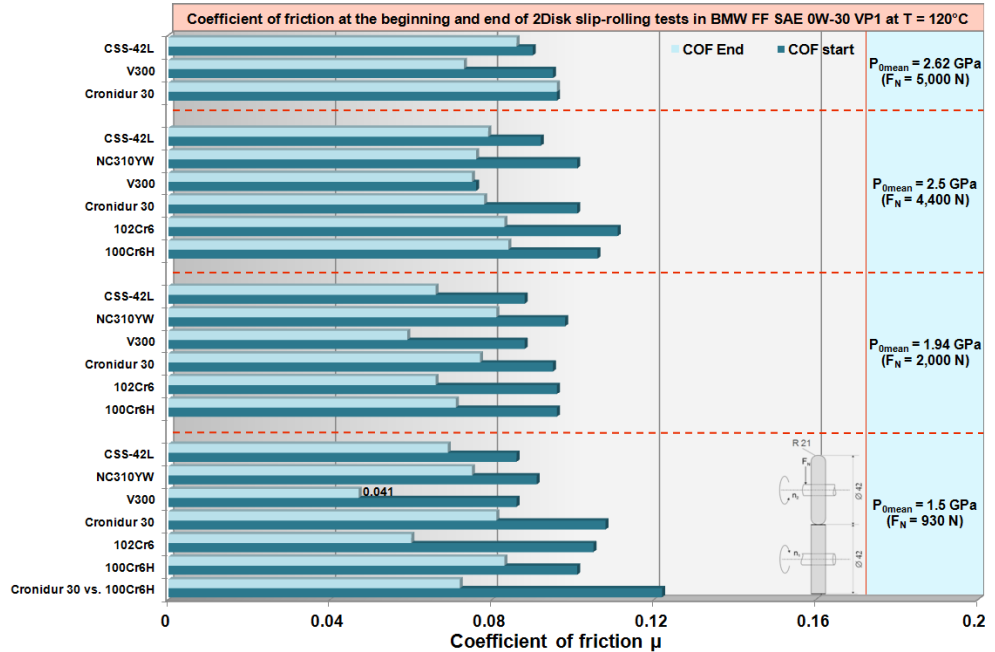


Figure 4-5: Summary of the coefficients of friction at the beginning and at the end of the test of uncoated steels

▪ Test results at $P_{0mean} = 1.94 \text{ GPa}$ ($F_N = 2,000 \text{ N}$)

In order to show the benefit of the novel high toughness alloys, it was necessary that the slip-rolling tests were carried out under more stringent conditions. For this reason the uncoated steel samples were tested at a much higher Hertzian contact pressure of $P_{0mean} = 1.94 \text{ GPa}$ (leading to $P_{0max} = 2.94 \text{ GPa}$) conditions.

After 10 million load cycles the affected steel surfaces showed nearly the same appearance as after the tests at $P_{0mean} = 1.5 \text{ GPa}$ in the optical micrographs. An increased Hertzian contact pressure finally led to larger track width after the tests ($\sim 1,300 \mu\text{m}$ to $\sim 1,600 \mu\text{m}$). Considering the results of the wear analysis an unexpected result associated with the steel 100Cr6H occurred. By means of tactile profilometry a wear rate $< 1.0 \cdot 10^{-10} \text{ mm}^3/\text{Nm}$ on the cylindrical test sample could be detected. Wear rates on such a scale are below the detection limit of the profilometer used. Even the lower quality bearing steel 102Cr6 offered a

Experimental results

good wear behavior. The advantage of low wear rates of CSS-42L at higher contact pressures could not be confirmed.

After 10 million cycles, SEM investigations of the uncoated CSS-42L test sample revealed small, marginal cracks ($\sim 2 \mu\text{m}$) along the chromium carbides inside the matrix (white arrows in Figure 4-6). The carbides were detected by means of SEM/EDX-elemental mapping (Bruker AXS XFlash[®] 5010 detector). V300 and NC310YW show similar surface patterns with singular micro-cracks on the scale of $4 \mu\text{m}$.

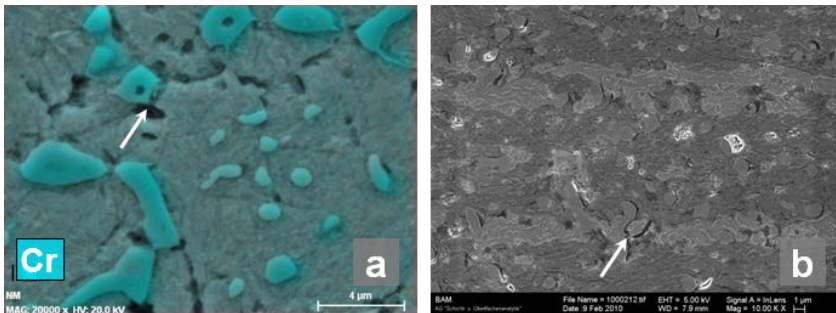


Figure 4-6: a) EDX Chromium mapping of CSS-42L and b) wear track of CSS-42L after 10 million load cycles at $P_{0\text{mean}} = 1.94 \text{ GPa}$ with detected microcracks along the chromium carbides (scale: a) $4 \mu\text{m}$ and b) $1 \mu\text{m}$)

Considering the coefficients of friction during the tests at $P_{0\text{mean}} = 1.94 \text{ GPa}$, the friction values remained in the same order of magnitude as under $P_{0\text{mean}} = 1.5 \text{ GPa}$. Whereas with a value of 0.059 V300 revealed the lowest COF_{End} in comparison to the other tested steels. Furthermore, at this load stage the friction values of all steels were not as widely spread as in the tests at 1.5 GPa .

▪ Test results at $P_{0\text{mean}} = 2.5 \text{ GPa}$ ($F_N = 4,400 \text{ N}$)

A further, new stage in testing steels without any protecting thin film coatings for highly advanced applications was reached by increasing the average contact pressure up to 2.5 GPa .

Very recently, in the tests at 2.5 GPa , the steel NC310YW reached its limit of performance. After $1.26 \cdot 10^6$ cycles macro-pitting and a total fatigue steel surfaces occurred, whereas the nearly similar steel grade V300 reached the endurance test end without structural failures. From the mechanical properties of both steels the failure of V300 with lower yield strength properties might be expected. The bearing steels 102Cr6 and 100Cr6H could finalize the test at 10 million load cycles. However, the microscopic investigations of both worn surfaces exhibited an amount of small cracks transversally to the rolling direction (cf. Figure 4-7).

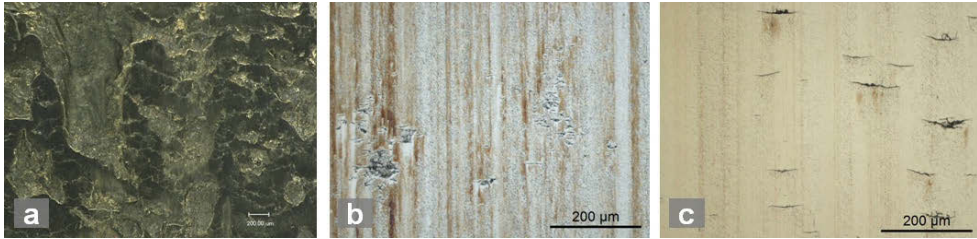


Figure 4-7: Magnifications of the affected surfaces of a) NC310YW, b) 102Cr6 and c) 100Cr6H (scale: 200 μm)

The alloys Cronidur 30, V300 and CSS-42L resisted this load level with some plastic deformation along the wear track.

In case of 100Cr6H at 2.5 GPa, the illustration of the wear rates in Figure 4-3 reveals likewise a very good wear profile as at 1.94 GPa (cylindrical 100Cr6H sample $\sim 1.08 \cdot 10^{-10} \text{ mm}^3/\text{Nm}$). The high wear rates of NC310YW are the result of the complete disruption of both contacting surfaces. Considering these results the alternative steels offered no benefit compared with the commonly used steels.

With higher demands on the steel surfaces the friction coefficient are approximately in the same range of 0.078 at the end of the tests. The coefficients of friction of V300 at the beginning and at the end exhibited no significant differences as in case of the other steels.

- **Test results at $P_{0\text{mean}} = 2.62 \text{ GPa}$ ($F_N = 5,000 \text{ N}$)**

At the load stage of 2.62 GPa, only three couples uncoated steels were tested. In Figure 4-1 it is shown that V300 did not reach the 10^7 load cycles (test abort at $2.18 \cdot 10^6$ cycles). Remarkable results showed Cronidur 30 and CSS-42L by reaching 10^7 cycles without failures on the surface. Surface investigation by means of optical microscopy of the cylindrical and spherical disc showed some plastic deformations along the wear track and microcracks transverse to sliding direction on 25 μm scale.

Even the results of the wear calculation offered an unexpected result in case of Cronidur 30. The wear rate of the spherical counterbody was below the detection limit.

As in all other test series, it is evident that V300 is the alloy with lowest coefficient of friction at the end of the test.

4.1.2 Slip-rolling resistance of coated systems

In recent investigations [Man10] [Man10-2] [Man10-3] coatings of different types and suppliers were tested under slip-rolling conditions to evaluate their slip-rolling resistance and improve the coating characteristics during stress conditions (rolling, sliding). In order to guarantee the best adhesion layer possible, the coatings were deposited on the aforementioned super-polished test sample surfaces. Over the course of different developing strategies the slip-rolling resistance of the majority of thin film coatings could be improved from primarily several thousand up to several millions of load cycles.

Experimental results

In order to compare the results obtained of different coating, the diagrams in Figure 4-10 to Figure 4-15 present the slip-rolling performance of the coatings and their different batches. The logarithmic y-axis mentions the number of cycles until failure or official test end. The different colors of the bars plotted represent the cycles reached until failure at distinct load stages performed with BMW FF SAE 0W-30 VP1 at $T = 120^{\circ}\text{C}$. The grey boxes, at the top and bottom of the diagram, symbolize the kind of the steel counterbody and the kind of the substrate.

- **Fraunhofer IWS a-C and ta-C coatings**

Two types of coatings were supplied by Fraunhofer IWS. Versions V1, V4 to V6 and V8 can be classified as ta-C, whereas V2, V3 and V7 belong to the category a-C according to the VDI guideline 2840 [VDI05]. The deposition process of Fraunhofer coatings has been refined in recent years. Starting with pulsed arc deposition, the coatings V1-V3 were developed. The second step in deposition methods is the use of pulsed laser arc deposition for coatings V4-V7. In 2011 a new filter laser arc process was introduced to deposit coating type V8 with smooth roughness values of the coating compared to coating versions V1-V7. Figure 4-8 presents the slip-rolling resistance and the coefficients of friction of these coatings lubricated with factory fill engine oil SAE 0W-30 VP1 at 120°C .

Initial, former slip-rolling tests of these coatings at room temperature showed a good slip-rolling resistance in unadditivated paraffinic oil [Woy10]. However, the slip-rolling resistance was significantly reduced by increasing the oil temperature to 120°C . Following developments deposited on Cronidur 30 shown in Figure 4-8 with the variants V2 to V8 did not fully met the expectations of 10 million cycles, but passed in some cases one million cycles at 120°C oil temperature in VP1. Comparing the slip-rolling results of coating V2 deposited on two different steel substrates (100Cr6H, Cronidur 30), it seems that the steel substrate influences the rolling resistance. The failure of the coatings appeared as partially total flaking-off of the thin films (see Figure 4-9). Due to the poor slip-rolling resistance of recently developed IWS coatings, a deposition of the alternative steel grades was relinquished.

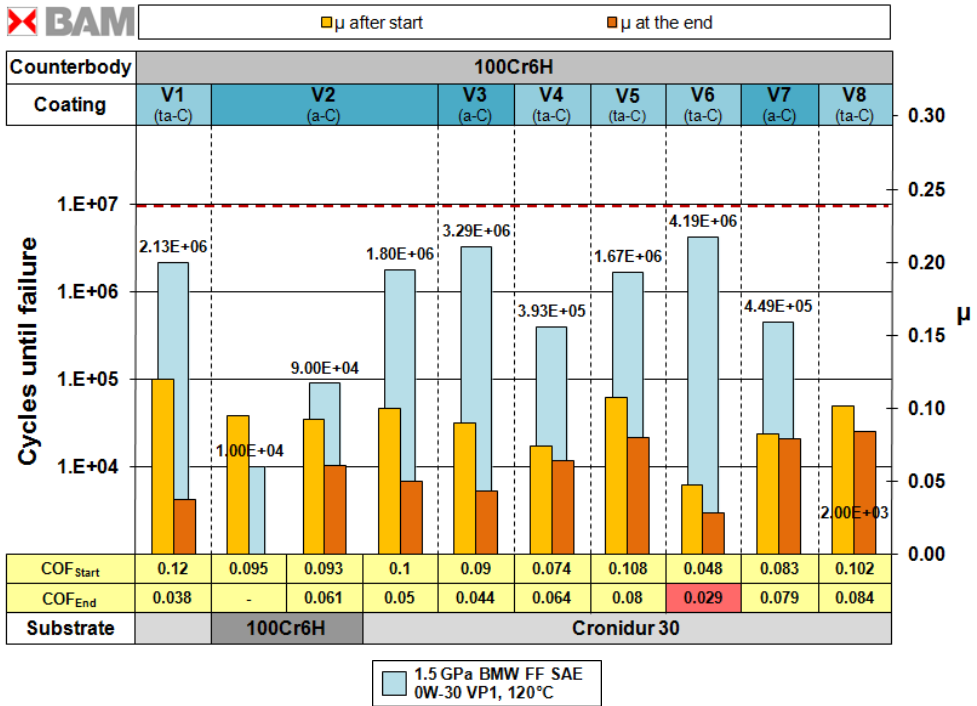


Figure 4-8: Results of Fraunhofer IWS Dresden a-C and ta-C thin film coating under slip-rolling conditions



Figure 4-9: Defects of Fraunhofer IWS coatings at $P_{0mean} = 1.5 \text{ GPa}$ in VP1 a) ta-C V5, b) ta-C V6 and c) a-C V7 (scale: a) 1000 μm , b) and c) 500 μm)

It has been shown that IWS a-C and ta-C films have a degree of potential as slip-rolling resistant coatings at mean Hertzian pressures up to 1.5 GPa and 120°C. There is no clear correlation between the mechanical properties of the coating types and lifetime, because both super hard and stiff ta-C (V6: Youngs Modulus 606 GPa, hardness 63 GPa) and a soft a-C coating (V3: Youngs Modulus 204 GPa, hardness 19 GPa) obtained the highest cycle numbers. Very low friction values below 0.029 were obtained in a state-of-the-art engine oil VP1 with the hardest ta-C coating combined with a low wear rate of $6.6 \cdot 10^{-10} \text{ mm}^3/\text{Nm}$ after running-in. The relatively high roughnesses after deposition generated significant running-in wear and represent a weakness for these types of a-C and ta-C thin films.

Experimental results

▪ BMW Group a-C:H coatings

An overview of the slip-rolling resistance of two in-house developed BMW a-C:H DLC coatings is given in Figure 4-10.

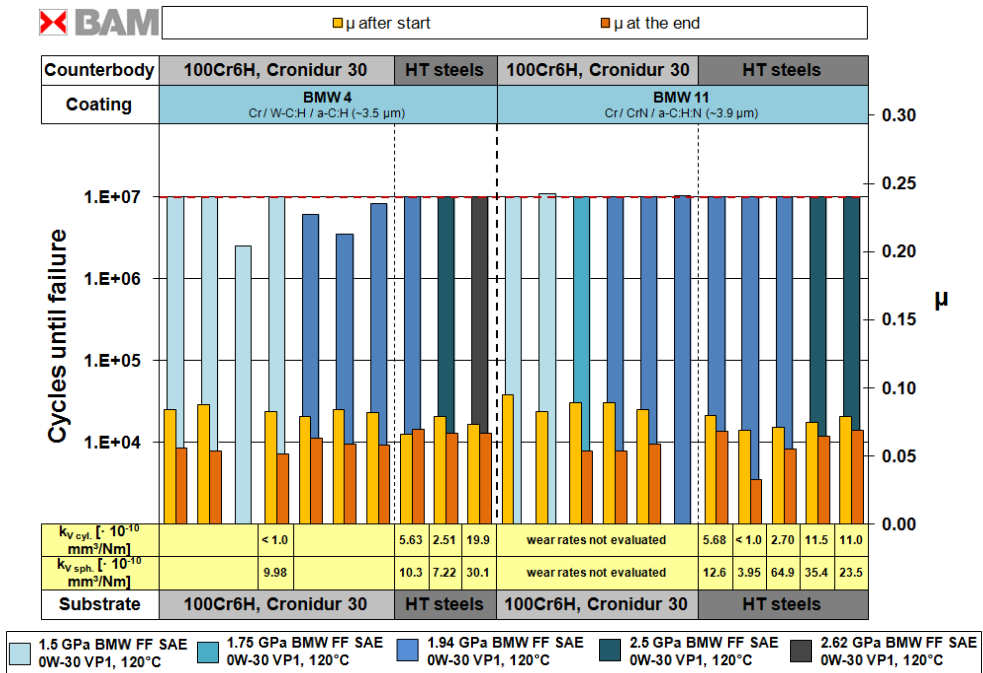


Figure 4-10: Slip-rolling resistance auf BMW a-C:H coatings BMW 4 and BMW 11 with corresponding coefficients of friction (BMW Group, Munich)

In this figure the slip-rolling resistance and characteristic tribological criteria of two selected BMW coatings, BMW 4 and BMW 11, are compared. Clearly visible is the excellent slip-rolling resistance of coatings BMW 4 and BMW 11 at lower contact pressures of 1.5 GPa. The positive test behavior under the standard testing conditions allowed an increase of the initial average Hertzian contact pressure up to 2.5 GPa ($F_N = 4,400$ N) respectively 2.62 GPa ($F_N = 5,000$ N) lubed by the standard engine oil VP1 at 120°C. In using high toughness steel grades as substrate materials, the slip rolling resistance of BMW 4 could be increased and even the highest load could be applied without destroying the coating or its counterbody. The topographical pictures of the coated surfaces after slip-rolling tests at 2.5 GPa, showing are summed up in Figure 4-11. Only in case of BMW 11 on V300 a marginal plastic deformation is visible of the substrate,

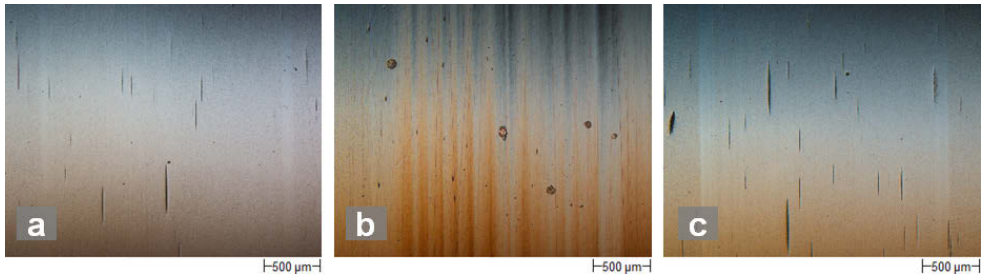


Figure 4-11: Wear tracks of BMW 4 and BMW 11 coatings after tests at $P_{0\text{mean}} = 2.5 \text{ GPa}$: a) BMW 4 on CSS-42L, b) BMW 11 on V300 and c) BMW 11 on CSS-42L (scale: $500 \mu\text{m}$)

Wear calculations of the coatings after the tests did not show a unified picture. BMW 11 on NC310YW tested at 1.94 GPa offered wear rates close to and below the resolution limit of the tactile profilometry. In contrast to this excellent result, the identical coating from the same deposition batch on CSS-42L showed much higher wear rates. It can be concluded that the uncoated CSS-42L counterbody appears to have a lower wear resistance towards a DLC coating than in case of V300 and NC310YW counterbodies, despite its higher hardness. In order to visualize the low wear of the BMW coatings AFM (Atomic Force Microscope) images within the wear track and beside the wear track were taken (see Figure 4-12).

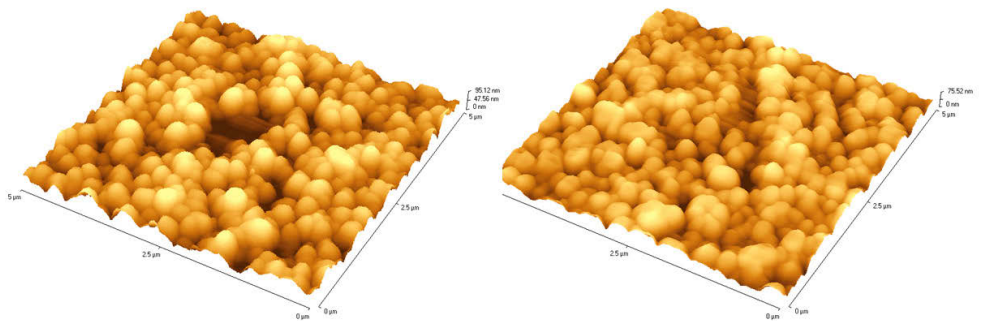


Figure 4-12: AFM images of the unaffected BMW 11 coating surface (left) and the coating surface after slip-rolling test at $P_{0\text{mean}} = 1.5 \text{ GPa}$ in BMW FF SAE 0W-30 VP1 at 120°C (right)

The roughness analysis of the AFM images taken showed a medium change in the roughness values. The unaffected surface had an initial roughness of $R_a = 0.02 \mu\text{m}$ and $R_z = 0.025 \mu\text{m}$, whereas the roughness after the test could be evaluated with $R_a = 0.013 \mu\text{m}$ and $R_z = 0.015 \mu\text{m}$. Furthermore the images revealed that the coating structure after the test is completely intact, this means that cracks could not be identified. BMW 11 on NC310YW also showed a very low coefficient of friction with 0.033 at the end of the tests, which is worth mentioning. However, the coatings of BMW Group showed remarkable results in slip-rolling tests, but no tribological advantages of BMW 4 compared with BMW 11 can be found.

Experimental results

▪ **Fundación Tekniker Zr(C,N) coatings**

The tribological performances of the different Zr(C,N) batches are well considered and examined by Manier [Man10]. It was shown that by applying a process controlled nano-layered Zr(C,N) coating the slip-rolling resistance can be improved up to 10^7 load cycles. Figure 4-13 illuminates the slip-rolling resistance of all Zr(C,N) batches which have been produced since 2006, whereas coating batch K(1) and K(10) are processed as controlled nano-layers. The tribological consideration of Zr(C,N) coated high toughness steels (batch K(10)) was part of this work.

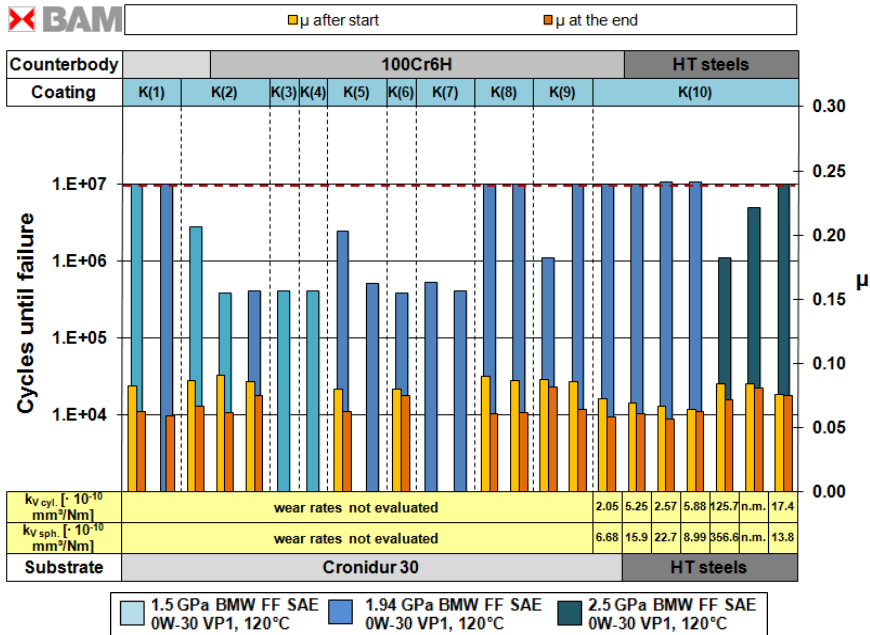


Figure 4-13: Diagram summarizing the slip-rolling resistance obtained with Zr(C,N) coatings of different batches deposited by Fundación Tekniker, Spain (test results of K(1) to K(9) determined by Manier [Man10])

With the knowledge of producing a slip-rolling resistant alternative coating to diamond-like carbons, Zr(C,N) was also applied on high toughness steel grades to show which maximum loads this coating can withstand. As is to be expected Zr(C,N) deposited on V300, NC310YW and CSS-42L as well as on Cronidur 30 reached the test end unscathed. Even up to P_{0mean} of 2.5 GPa, Zr(C,N) on CSS-42L is slip-rolling resistant without showing any failures on the surface (cf. Figure 4-14). The failure of Zr(C,N) on V300 occurred via the initial failure of the uncoated counterbody. A flake of approximately 2,500 x 2,500 μm broke out of the surface due to cyclic deformation and damaged the coating surface until the test was interrupted. Considering the failure mechanism of NC310YW vs. Zr(C,N) both surfaces revealed completely destroyed surfaces by plastic deformation, cracks and pitting along the whole wear track.



Figure 4-14: Sections of stressed and partial flaked Zr(C,N) wear tracks after a) 1.11 mio. cycles (V300), b) 4.98 mio. cycles (NC310YW) and c) 10 mio. cycles (CSS-42L) tested at $P_{0mean} = 2.5$ GPa and $T = 120^{\circ}\text{C}$ (scale: 500 μm)

Comparing the coefficient of friction it becomes visible that the values at end of the tests do not vary significantly in the respective load stages. The implementation of Zr(C,N) allows a reduction of friction down to 0.06 at the test end ($P_{0mean} = 1.94$ GPa).

▪ **KYB Corp. a-C:H coatings**

KYB Corp. provided two types of coatings: a-C:H (Type A) and a-C:H:Cr (Type B) [Tam12]. Figure 4-15 shows a distinct difference between both coating types, A and B, in the slip-rolling resistance as well as in the coefficient of friction values at test end. Tests with coating Type B could not reach the final slip-rolling criterion of 10^7 load cycles at $P_{0mean} = 1.5$ GPa. Remarkable results in slip-rolling resistance and wear behavior were obtained by using coating Type A.

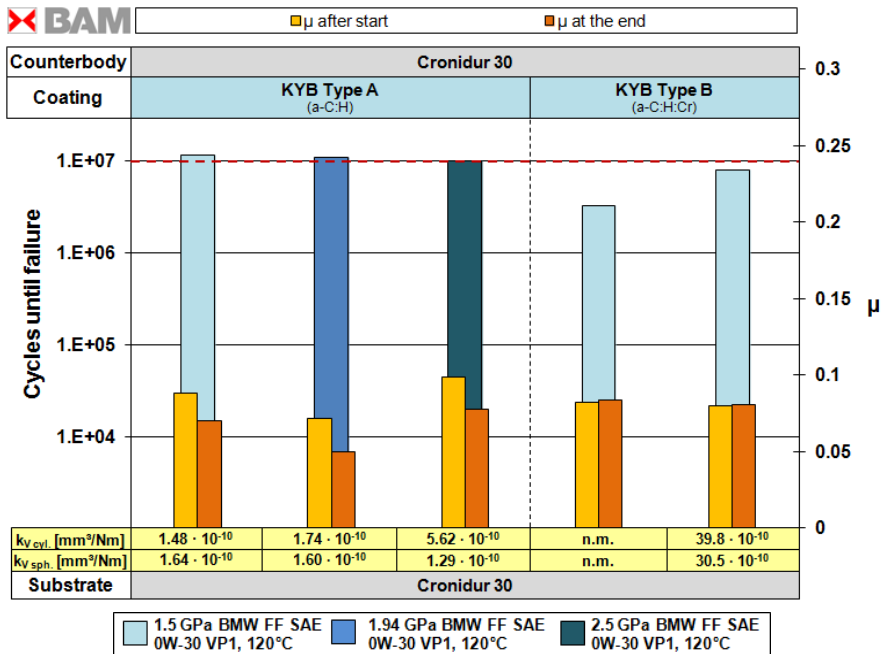


Figure 4-15: Slip-rolling resistance of a-C:H and a-C:H:Me coatings provided by KYB Co., Japan

Experimental results

Comparing the roughness values of KYB coatings with the coatings of the BMW group, BMW 4 and BMW 11, it became clearly visible that the KYB coatings are much smoother (cf. Table 4-1).

Table 4-1: Roughness values of coatings KYB Type A, KYB Type B, BMW 4 and BMW 11 measured

	KYB Type A	KYB Type B	BMW 4	BMW 11
R_a [μm]	0.01	0.01	0.023	0.015
R_z [μm]	0.06	0.29	0.169	0.116
R_{pk} [μm]	0.01	0.04	0.038	0.03

Similar to BMW 4 and 11, the coating Type A can withstand the high contact pressure of $P_{0\text{mean}} = 2.5$ GPa without showing any visible worn surface. Even in the light microscopic analysis the wear track is not quite clear to define (see Figure 4-16). Furthermore, indication for the slightly worn surface is the very low wear rate. In contrast to BMW provided coatings, the wear rates of the associating uncoated counterbody offered also wear rates close to the detection limit.

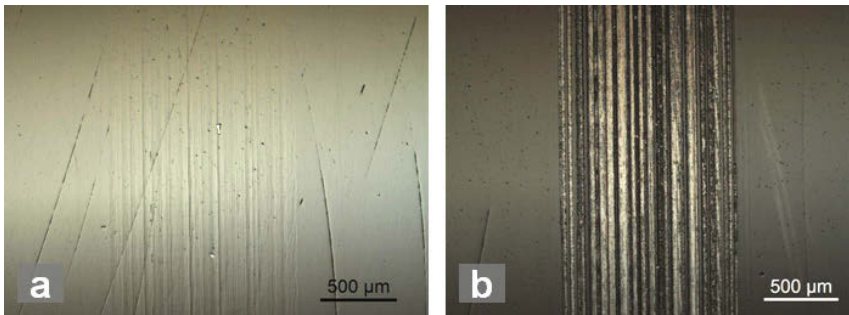


Figure 4-16: Optical micrographs of the stressed under $P_{0\text{mean}} = 1.5$ GPa KYB coatings a) type A after 10 mio. load cycles and b) type B after 3.32 mio. load cycles (scale: 500 μm)

4.1.3 Tribological behavior of self-mated DLC coatings

Within the context of corporation with the BMW Group, the frictional behavior was investigated of self-mated DLC coatings in slip-rolling tests. For this purpose, the DLC coating was not only applied to the cylindrical test sample, but also to the previously polished spherical counterbody. In order to ensure a sufficient adhesion of the DLC the counterbody was polished after grinding. This polishing step led to a surface roughness values of approximately $R_z = 0.034$, $R_a = 0.005$ and $R_{pk} = 0.008$. Hence, the surface conditions were the same for coating deposition of the cylindrical and spherical disc. For the selection of coatings to be tested against another DLC film, the decision was made to use the reliable BMW 4 coating for the spherical disc. Two recently developed and in their composition very similar coatings BMW 13 and BMW 14 were used in the test series at 1.5 GPa average Hertzian contact pressure. All coating pairing reached the predetermined limit of 10 million load cycles (cf. Figure 4-17).

After the tests, the wear rate was found to be below the detection limit of $< 1.0 \cdot 10^{-10} \text{ mm}^3/\text{Nm}$ in case of all stressed discs. Figure 4-18 depicts the worst test result of the pairing BMW 4 vs. BMW 13 (a and b) and the best of BMW 4 vs. BMW 11 (c and d). The width and location of the wear track were not possible to define of the BMW 4 coated spherical body running with BMW 11 (see Figure 4-18 c). Exemplarily comparing the wear tracks of both spherical BMW 4 counterbodies the BMW 4 interacting with BMW 13 revealed small spallings along its circumference inside the wear track (Figure 4-18 a) whereas the interaction with BMW 11 led to an as good as new surface.

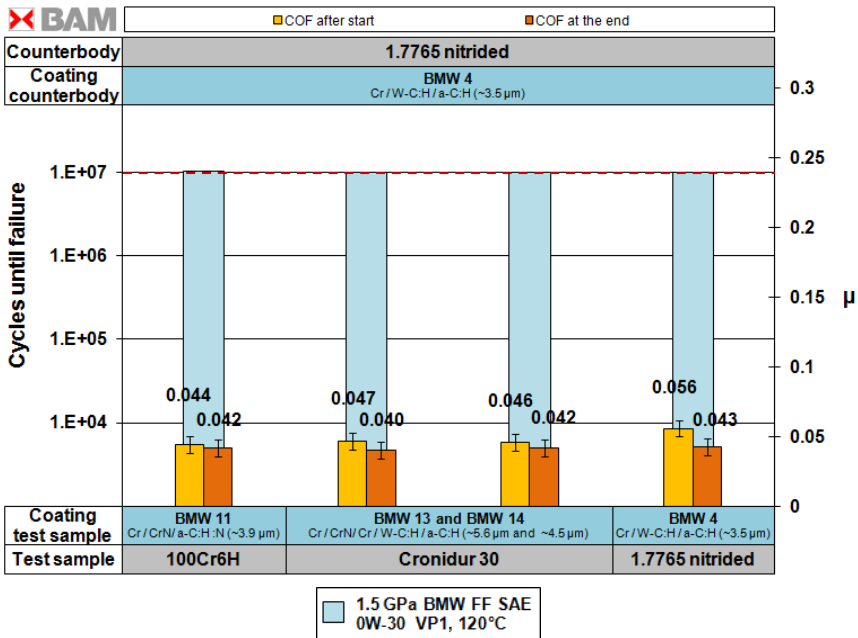


Figure 4-17: Slip-rolling test results of different BMW DLC coating against BMW 4 at $P_{0mean} = 1.5 \text{ GPa}$ and 120°C

Experimental results

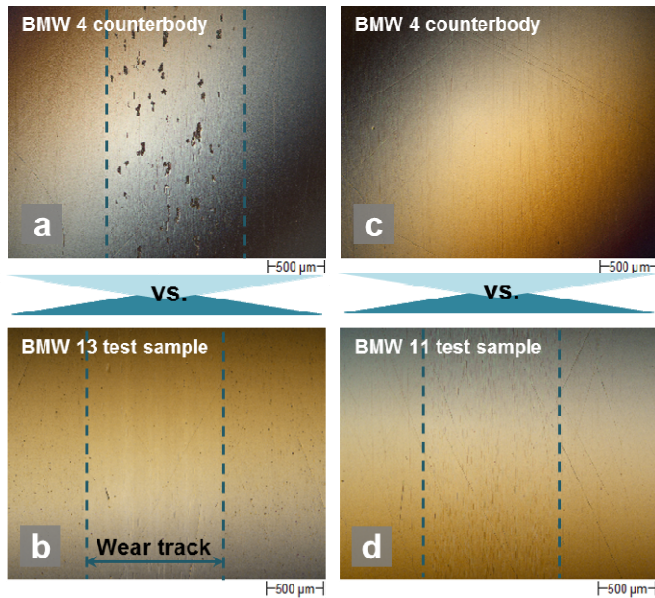


Figure 4-18: Images of the wear tracks by optical micrographs: a) BMW 4 counterbody of b) BMW 13 test sample, c) BMW 4 counterbody of d) BMW 11 test sample after 10 million load cycles at $P_{0mean} = 1.5 \text{ GPa}$ (scale: $500 \mu\text{m}$)

Regarding the frictional behavior of DLC vs. DLC, it can be deduced from the coefficients of friction at the beginning and at the end of the tests that the coatings did not show a running-in behavior as do steel pairings. Due to this fact the difference between both values is marginal (compare individual COF's in Figure 4-17).

4.2 Surface analysis at test end

Surface analyses as well as structural characterizations of the different steels and thin film coatings were performed on the most promising test samples or test samples which displayed conspicuities after the experiments.

4.2.1 SEM/ EDX observations

In the course of the SEM surface analyses of the test samples after tribological testing the chemical composition of the wear track was defined by means of EDX spectroscopy. A chemical characterization is important in considering the interaction of the coated or respectively uncoated steel surface with the engine oil used. Due to the huge amount of different additives and their various interacting processes with the surfaces to be protected, EDX was chosen as relatively easy and fast to handle method. A Thermo Fisher Scientific NSS 302 X-ray spectrometer equipped with a Si(Li) detector was used to conduct the investigations.

In Figure 4-19, the wear tracks of the cylindrical test samples (V300, NC310YW and CSS-42L) are illustrated after tribological tests at 1.5 GPa in VP1. All wear tracks revealed more or less fine stripes orientated in the rolling direction (brighter areas), which was identified as adhesive wear. These stretched areas are probably generated by the surfaces in contact submitted to sliding due to the different rotation speeds. A failure could not be observed which appearance is accompanied by massive RCF. The mentioned findings of noticeable areas inside the wear tracks were further analyzed by EDX spectroscopy. Stimulating the surface atoms with an acceleration voltage of 15 kV (CSS-42L: 10 kV) the spectra shown in Figure 4-19 were generated. Comparing the two spectra received of V300, no distinct difference in the chemical composition of the wear track surface can be determined. Characteristic elements of oils containing SAP (sulphur, ash and phosphor) such as phosphor and oxygen can be detected aside from a typical detergent element, calcium. Even the examination of NC310YW revealed the elements carbon, calcium, molybdenum, magnesium and small amounts of sodium contained in lubricants such as the VP1 used. Clearly visible is the higher peak of silicon in NC310YW due to its higher proportion in the chemical composition. High contents of vanadium, molybdenum, carbon and chromium can be found in the area of carbide structures in CSS-42L, whereas the matrix of this steel alloy predominantly revealed cobalt and iron as main components. An interaction between elements contained in the lubricant and the carbide structures cannot be found (compare Figure 4-19 CSS-42L Point 1 and Point 2).

The interaction of lubricant and steel surface became more visible by increasing the normal force and thus the contact pressure. During the test at $P_{0\text{mean}} = 2.5$ GPa the formation of a tribo-chemical film on the metal surface can be identified. The formation of tribo-chemical or tribo-reactive film on steel surfaces as well as on DLC-coatings is considered in literature many times. Overbased calcium sulfonate (CaSO_4)¹⁶ or carbonate (CaCO_3) play an important role in their function as detergents in lubricants. This type of additives is basically built up as colloidal dispersions of metal hydroxides, carbonates or borates which are stabilized by metallic soaps such as phenates, salicylates or sulfonates [Ciz04].

¹⁶ also known as OCABS: overbased calcium alkyl benzene sulfonates

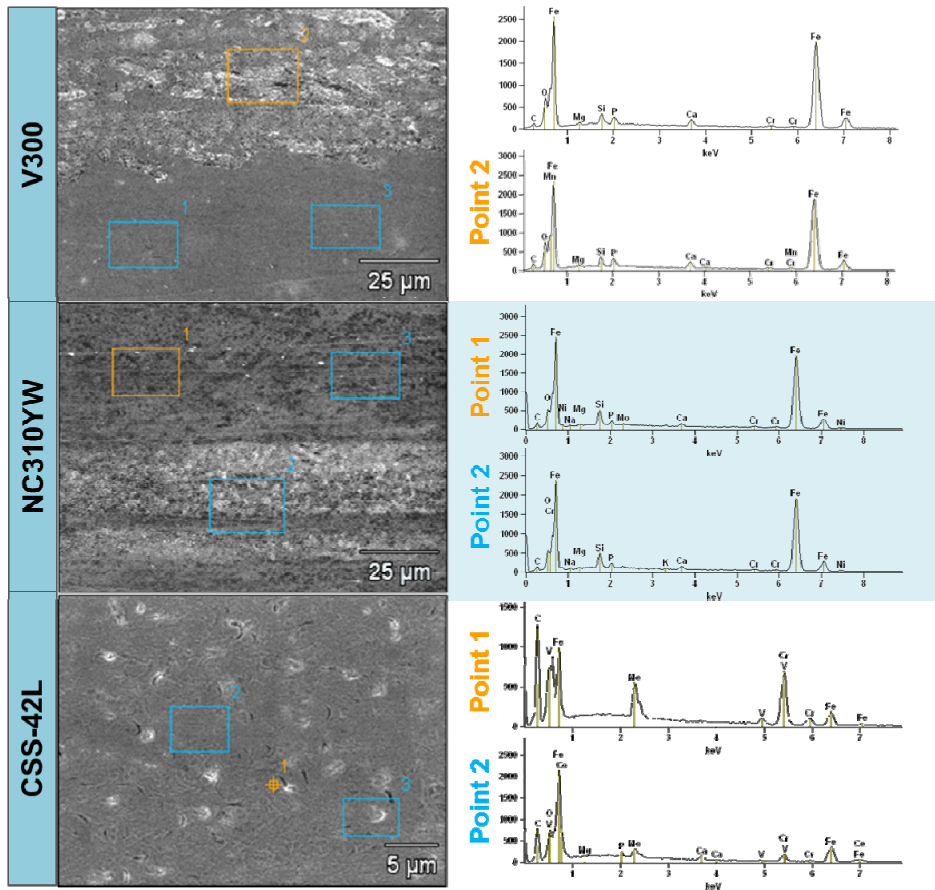


Figure 4-19: SEM pictures of V300, NC310YW and CSS-42L wear tracks and corresponding local EDX spectra of noticeable areas tested in VP1 at 1.5 GPa and 120°C after 10 million load cycles (scale: 5 μm and 25 μm)

4.2.2 Chemical analysis of detected tribo-reactive layers (EDX-element mapping)

The results of the first EDX analysis and the detection of the white appearing reaction layer require a more detailed inspection. Different tests at higher contact pressures showed that the formation of this layer starts during the running in process of the test samples, between 100,000 and 200,000 load cycles. Of interest was not only the uncoated steel surface, but also the interaction of the lubricant with the DLC (BMW 11) and Zr(C,N) (batch K(10)), which are frequently described as chemical inert. Therefore, two tests with coated V300 samples against uncoated counterbodies were carried out for 600,000 load cycles at $P_{0\text{mean}} = 2.5 \text{ GPa}$ and 120°C in VP1. Simultaneous investigations of load affected (field of white layer) and unaffected areas on the sample surface were conducted by superimposing SEM images with EDX mappings (Bruker AXS XFlash® 5010 detector), concise presenta-

tion in Figure 4-20. It is also clearly visible that the machining grooves on the counterbody surface were leveled within the wear track due to the tribological contact.

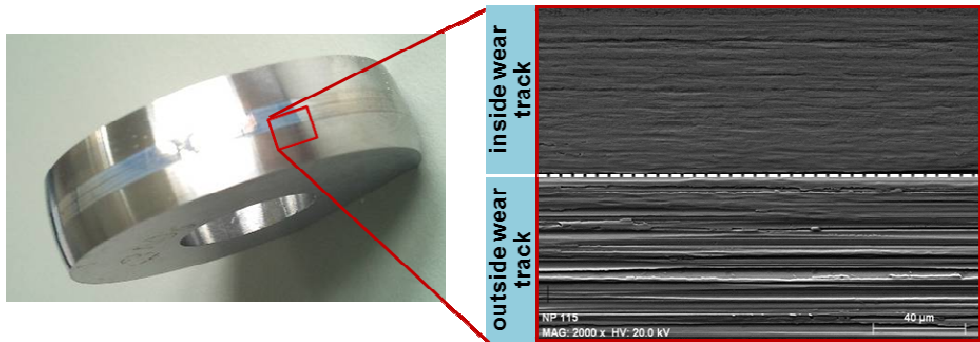


Figure 4-20: White appearing tribo-reactive layer on V300 counterbody (left) and SEM observation of the stressed wear track and unaffected outlying area tested at $P_{0\text{mean}} = 2.5 \text{ GPa}$ and 120°C in VP1 (scale: $40 \mu\text{m}$)

Comparing SEM observations of the wear track and beside the wear track it became clearly visible that the surface inside the wear track of the uncoated sample is smoothed compared to the unloaded state. In the case of the DLC coated V300 sample (BMW 11), a wear track could be determined only at higher magnification due to the high wear resistance and nearly no smoothing effect. With EDX, it could be established that the BMW 11 surface exhibits small concentrations of calcium, molybdenum, oxygen, sulphur and zinc (cf. Figure 4-21). A distinction in the element concentrations between wear track and the unaffected area could not be proved. The analysis of the white layer found on uncoated steel counterbodies showed amounts of calcium, molybdenum, oxygen, phosphorus, sulphur and fluorine. The observation of calcium, oxygen and sulphur in similar areas suggests that the layer is indeed formed by overbased calcium sulfonate detergents. Remarkably, a carbon transfer layer of the BMW a-C:H coating onto the steel surface could not be detected, whereas iron could be found as transfer on the coating surface. One of the emerging conclusions is that the DLC surface did not show any wear during the testing time of 600,000 load cycles. All elements with the exception of carbon, iron and oxygen are chemical elements which can only originate from used additive packages in the oil. Furthermore, dependency of the formation of such layers on the contact pressure can be noted. Summarizing the observed results in can be concluded that additive elements independently interact from the contact pressure with the DLC coated surface. In contrast, it seems that an activation parameter such as the contact pressure is needed to support the interaction of additive elements contained and steel surface.

Experimental results

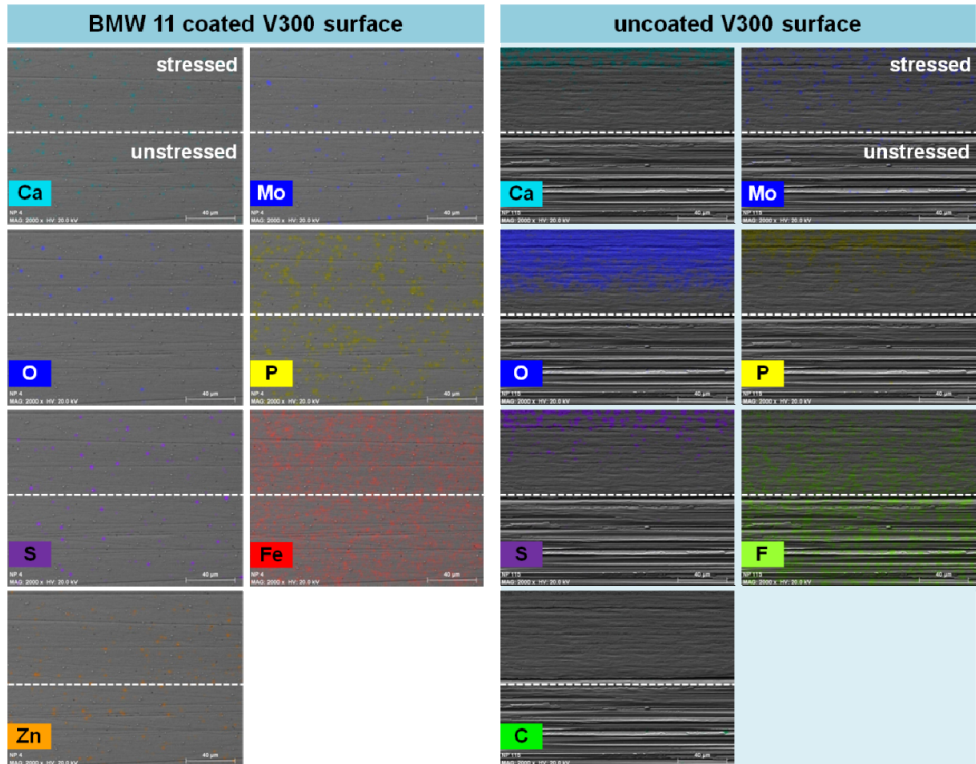


Figure 4-21: SEM images of BMW 11 coated V300 (left) and uncoated V300 (right) tested in VP1 oil at 2.5 GPa (600,000 load cycles) and 120°C superimposed with EDX mappings (scale: 40 μm)

A slightly different picture of element mapping shows the combination of Zr(C,N) and uncoated V300 after the test under identical conditions (Figure 4-22). For all elements detected on the Zr(C,N)-surface a distinct difference in concentrations is visible between wear track and outside the wear track. Especially oxygen and molybdenum illustrated the lower chemical inertness of Zr(C,N) in comparison to the BMW DLC coating. As already observed by Manier [Man10], small droplets (white arrows in Figure 4-22) on the Zr(C,N)-surface can be recognized, which cannot be found again inside the wear track. Other interesting features are small holes in the coating of up to 4 μm scale. An in literature often claimed function as oil reservoir for emergency running in case of a lubrication supply breakdown cannot be confirmed due to the absence of oil residues in the holes. The analysis of the uncoated V300 surface after the test offered a variety of different chemical elements which remained as thin layer. In contrast to the aforementioned observation of BMW 11 and its uncoated counterbody a residue of zinc in addition to calcium and molybdenum traces were detectable. Widely used Zn-based additives in engine oils are zinc dialkyldithiophosphates (ZDDP, ZnDTP) which can form wear protective layer (zinc polyphosphates) even on DLC's [Mar01].

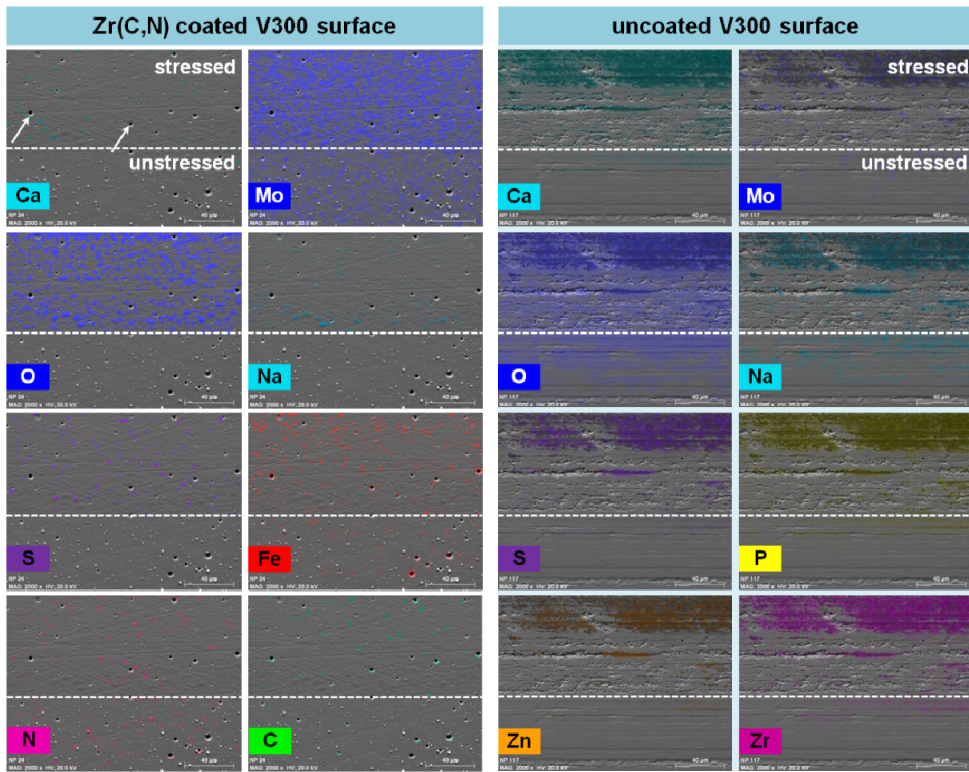


Figure 4-22: SEM images of Zr(C,N) coated V300 (left) and uncoated V300 (right) tested in VP1 oil at 2.5 GPa (600,000 load cycles) and 120°C superimposed with EDX mappings (scale: 40 μm)

4.2.3 Further considerations on the chemical structure (XPS and AES)

By means of EDX measurement systems, individual chemical elements can be detected. However, chemical compounds which were accumulated onto the steel or coating surface due to tribo-chemical reactions cannot be identified by this measuring method.

XPS (X-ray photoelectron spectroscopy) and AES (Auger electron spectroscopy) analysis of the surface provide a better significance to characterize thin reactive layers. By using XPS, two tested samples were examined, i.e. uncoated V300 and BMW 11 coated V300. The pairing was tested at an average Hertzian contact pressure $P_{0\text{mean}} = 2.5 \text{ GPa}$ for 10 million load cycles in up to 120°C heated oil VP1. The number of detected electrons, stimulated by non monochromatic Al and Mg K_{α} radiation, were plotted against the binding energy of the electrons detected. The resulting characteristic peaks correspond to the electron configuration of the electrons within the atoms and can be assigned to their atomic or molecular orbitals (1s, 2s, 2p, 3s, etc.). The amount of elements within the irradiated area is directly linked to the number of detected electrons in each peak (counts per second). XPS is frequently applied as surface characterization because of its low penetration depth (1 to 10 nm). Therefore, this analysis method is predestinated to observe reactive tribofilms and

Experimental results

allows monitoring the chemical composition. Two pre-evaluated XPS spectra of the affected BMW 11 and V300 surface are displayed in Figure 4-23 and Figure 4-24.

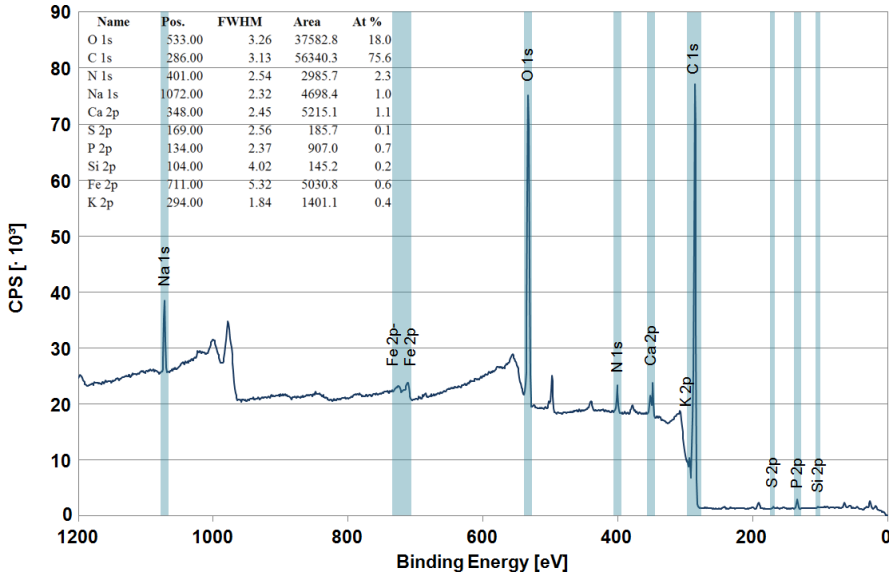


Figure 4-23: XPS spectrum of BMW 11 inside the wear track after 10 million load cycles at $P_{Omean} = 2.5$ GPa and 120°C in VP1

The wide scan survey spectrum for all elements of BMW 11 wear track delivers comparable results with the analysis by use of EDX mapping. Large XPS oxygen 1s (18.0 at.-%) and sodium 1s peaks (1.0 at.-%) could be indexed by XPS whereas the element mapping did not show any presence of oxygen and sodium on the DLC-surface. Additionally, appreciable amounts of calcium and phosphorus could be detected indicating the formation of a fragmentary Ca-based tribofilm. Evaluating particularly the calcium 2p peak with regard to their tribological relevance and the white appearance five compounds could be identified [NIST]:

- CaCO_3 (Calcium carbonate)
- CaSO_4 (Calcium sulfate)
- $\text{Ca}_2\text{P}_2\text{O}_7$ (Calcium pyrophosphate)
- CaSiO_3 (Wollastonite)
- CaF_2 (Calcium fluoride)
- CaO (Calcium oxide)

Effectively, the investigations on the formation of Ca-based tribofilms in literature are very restricted. Due to the very low detected ratios of fluorine and silicon CaF_2 and CaSiO_3 may be excluded from the list of possible compounds formed. Calcium pyrophosphate ($\text{Ca}_2\text{P}_2\text{O}_7$) is classified to the group of “white solid lubricants” and is mostly used as tribological addition to composite materials on the basis of iron [Wäs89] [Dah06]. According to high resolu-

tion XPS recording of calcium area the presence of calcium pyrophosphate might be conceivable, but literature did not report such tribofilm formation from engine oil. Yu et al. investigated the wear behavior and a possible tribofilm formation of silane-based antiwear additives [Yu11]. In most cases overbased calcium detergents are added to engine oils such as the VP1 used. Past investigations of Wan showed indeed the formation of CaCO_3 layer [Wan02]. The most likely scenario of the tribofilm formation is the interaction of the steel surface with overbased sulfonate structures. Kubo et al. proposed a model of boundary film formation on DLC and steel surfaces by calcium sulfonates [Kub07].

- 1st step: Formation of Fe and CaO-containing film on the steel surface by tribochemical reaction of iron oxide with calcium carbonate. Transfer of the film onto the DLC surface simultaneously.
- 2nd step: Accumulation of CaCO_3 and decreasing iron content.
- 3rd step: Reaction of calcium carbonate in the additive forms the boundary film composed of CaO and CaCO_3 .

Moreover, signs of sodium residuals on the uncoated V300 steel surface and DLC surface are detectable (approximately 1.0 at.-% on V300 surface, see Figure 4-23 and Figure 4-24). The most known and widely applied ZDDP additives forming for example protective zinc (poly)phosphate layers cannot be found on the bright steel surface as well as on the BMW 11 DLC surface.

Observations inside the wear track by AES (PHI-700 ULVAC-PHI), shown in Figure 4-25, were performed to confirm the analysis results of EDX and XPS measurements. This examination of $10 \times 10 \mu\text{m}$ areas included four surfaces to analyze. BMW 11 and Zr(C,N) as coated test samples run under the aforementioned conditions (cf. paragraph 4.2.2) against uncoated V300 samples. Chemical elements such as carbon, oxygen, sulphur and calcium could be found as well as small amount of sodium especially on the blank steel surfaces. As already stated by XPS analysis, AES spectroscopy supports once more the thesis of a Ca-based tribofilm. The assumption that a DLC coating offers a wider chemical inertness was also confirmed.

Experimental results

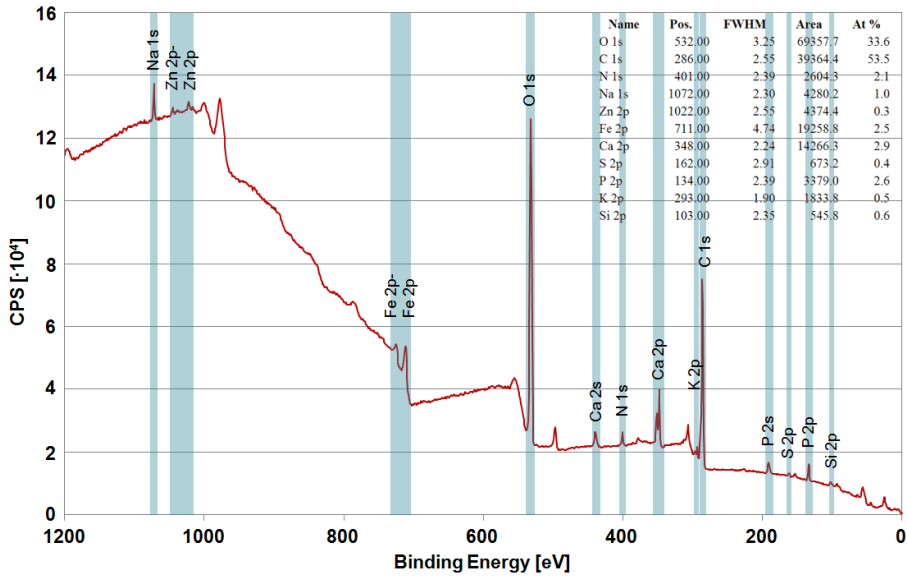


Figure 4-24: XPS spectrum of uncoated V300 inside the wear track after 10 million load cycles at $P_{0mean} = 2.5$ GPa and 120°C in VP1

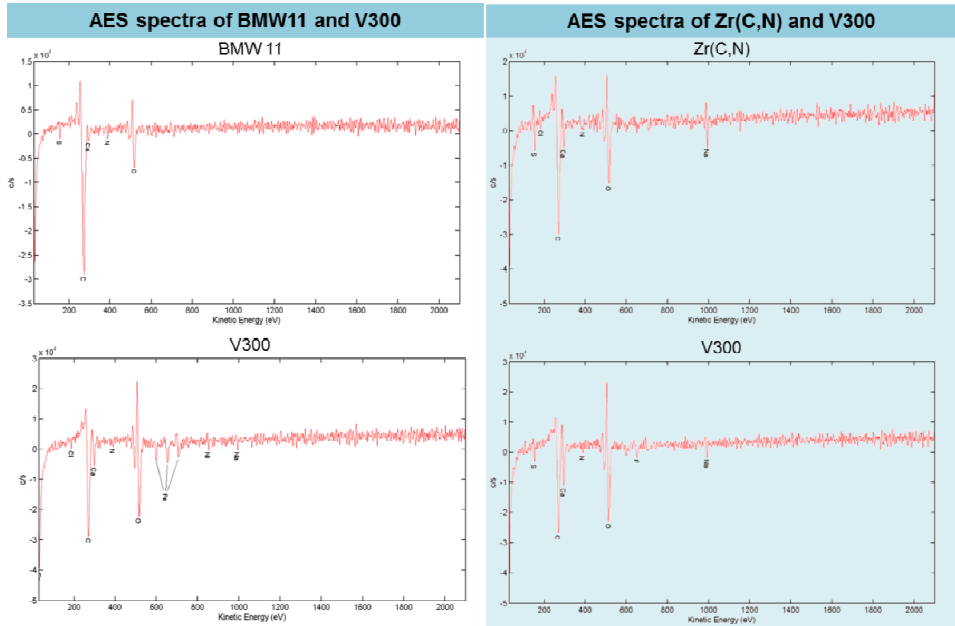


Figure 4-25: AES spectra of the pairings BMW 11/V300 and Zr(C,N)/V300 taken inside the wear track after tests in VP1 at 120°C and $P_{0mean} = 2.5$ GPa (600,000 load cycles)

4.3 Structural XRD results

The structural compositions as well as residual stress depth profiles were examined using XRD measurements methods. In-depth dissolved XRD analysis of the residual stress profiles were conducted in accordance to the $\sin^2\psi$ -method. This analysis method is based on the determination of phase-specific planes in the atomic lattice for different sample tilt angle ψ . Due to the functional interrelationship $\varepsilon_{\varphi,\psi} = f(\sin^2\psi)$, it is possible to evaluate the residual stress values σ_{φ} respectively ($\sigma_{11} + \sigma_{22}$) by linear regression as slope of the regression line from equation 4.2 and 4.3.

$$\sigma_{\varphi} = \frac{m_{\varphi}}{\frac{1}{2} S_{2,(hkl)}} \quad (4.2)$$

$$m_{\varphi} = \frac{\delta \varepsilon_{\varphi,\psi,A(hkl)}}{\delta \sin^2 \psi} \quad (4.3)$$

CoK $_{\alpha}$ -radiation ($\lambda = 0.17890070$ nm) on the 211-peak of ferrite was used in combination with K $_{\beta}$ -filter in the symmetric ω -2 θ -mode. On the primary side a 2mm²-round collimator was applied. Furthermore, on the secondary side, a vertical Soller slit as well as a scintillation detector were used. For quantification of residual stresses taking place parallel to the surface, the angular range of 97.5° to 102° was passed through in 0.1° steps (measurement duration 5 s per step). Hereby, the tilt angles ψ were $\pm 63.435^\circ$, $\pm 50.768^\circ$, $\pm 39.232^\circ$, 26.565° and 0° . The residual stresses were specified for rotation angle φ of 180° (axial direction transversally to the wear track) and 270° (circumferential direction along the wear track). In order to generate a depth profile after each residual stress measurement material of approximately 100 μm from the surface was electrolytically removed.

In this way the steels V300, NC310YW and CSS-42L were measured and calculated at the initial state of the materials, after slip-rolling tests at $P_{0\text{mean}} = 1.94$ GPa and 2.5 GPa and 10 million load cycles (NC310YW at 2.5 GPa analyzed after failure and 1.26 million load cycles).

4.3.1 X-ray diffraction profile of V300, NC310YW and CSS-42L

As previously mentioned, the structures of V300, NC310YW and CSS-42L were examined with XRD. The corresponding CoK $_{\alpha}$ -2 θ -diagrams using the Bragg-Brentano configuration are displayed in Figure 4-26. The peak positions detected were compared with diffractions data stored in a data base included within the measuring arrangement. The diffraction results of V300 correspond to the XRD retained austenite measurements whereas only 2.5 % retained austenite could be found. The overview diffractogram of V300 revealed the typical ferritic peak position with the pre-dominant ferrite peak (110). In a different connection synchrotron beamline (MAXIM) measurements at DESY of (200) ferrite peak will be discussed later in this context (paragraph 4.4.3). Considering the measurement results of NC310YW, it can be found that aside from ferritic structures also a detectable amount of austenite

Experimental results

exists. The aforementioned XRD analysis resulted in a 5.2% content of retained austenite. The evaluation of the measurement result concerning NC310YW revealed a diffraction profile of a cubic compound $\text{Fe Cr}_{0.29} \text{Ni}_{0.16} \text{C}_{0.06}$ which is similar to retained austenite on microstructure. In literature, insignificant amounts of M_{23}C_6 carbides were found in the structure of CSS-42L [Het08]. A very good correlation of the data base peak profile and the measured profile of Cr_{23}C_6 carbides could be found by this analysis. Effectively, all spectra did not show any inexplicable 2θ -peaks. Since Scherrer discovered the relationship between the widths of X-ray diffraction peaks and the crystallite size in 1918, the grain sizes of cubic structures can be evaluated by the following equation [Sch18]:

$$D_{hkl} = \frac{K \cdot \lambda}{B \cdot \cos \theta_{hkl}} \quad (4.4)$$

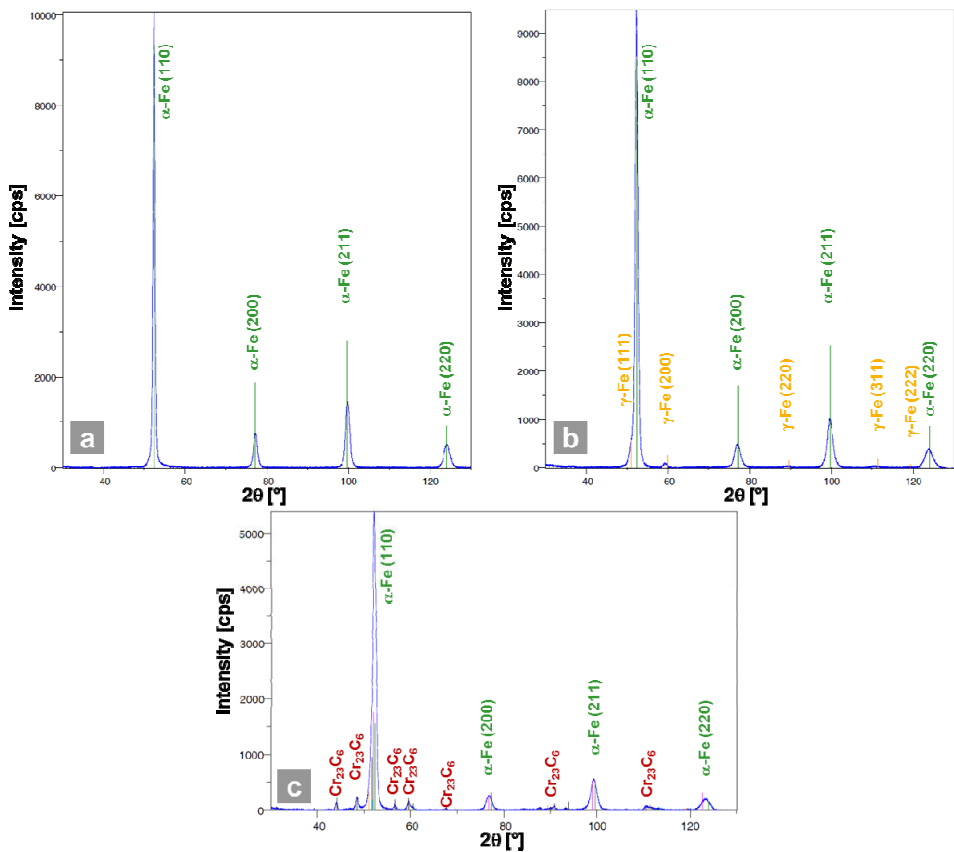


Figure 4-26: X-ray diffraction spectrum of a) V300, b) NC310YW and c) CSS-42L with CoK_{α} -radiation

Knowing the values of the wave length λ of CoK_{α} , the FWHM value B of the diffraction peak and the peak position θ , it is possible to determine the grain size D of fine structures (not applicable to grains larger than 100 nm). The factor K , called Scherrer constant, depends

on how the width is determined, the shape of the crystal and the size distribution. For cubic symmetry a K-factor of 0.94 is commonly used. A broader X-ray peak indicates small crystallite sizes. Applying the Scherrer equation (4.4), the evaluated average grain sizes for V300 are between 4 nm at (110)-peak and 7 nm at (200)-peak and for NC310YW in the range of 3 nm at (110)-peak to 5 nm at (200)-peak. The grain sizes of CSS-42L lie approximately between 3 nm at (110)-peak and 8 nm at (200)-peak.

4.3.2 Residual stresses in manufacturing state

As mentioned in paragraph 2.2.1, residual stresses can be caused by manufacturing processes as well as during the operating process. In order to clarify the stress conditions of the three alternative steels, a residual stress depth profile was taken. The stress profiles in the manufacturing state were observed immediately after polishing as the last step of machining. The resulting depth profiles of the XRD measurements are presented in Figure 4-27 (V300, NC310YW and CSS-42L).

It can be assumed that all detected profiles of untested steels offered compressive residual stresses up to 1,100 MPa (CSS-42L) due to the machining processes after heat treatment in axial and circumference measurement direction. The compressive stress values of CSS-42L are the highest compared to V300 and NC310YW. The analysis of this sample did not show the appearance of internal tensile stresses up to a measurement depth of 900 μm . With a case depth of approximately 1,000 μm , the residual stress profiles were restricted to the area affected by the case carburization process. At a depth of ~ 150 μm , in case of V300 and NC310YW, compressive residual stresses pass over to tensile residual stresses. According to the investigations of Schlicht et al. [Sch88], the residual stress course of V300 is consistent with a recorded residual stress course of bainitic steel whereas NC310YW is sufficient conform with martensitic structures (compare Figure 2-6 left and Figure 4-27).

Experimental results

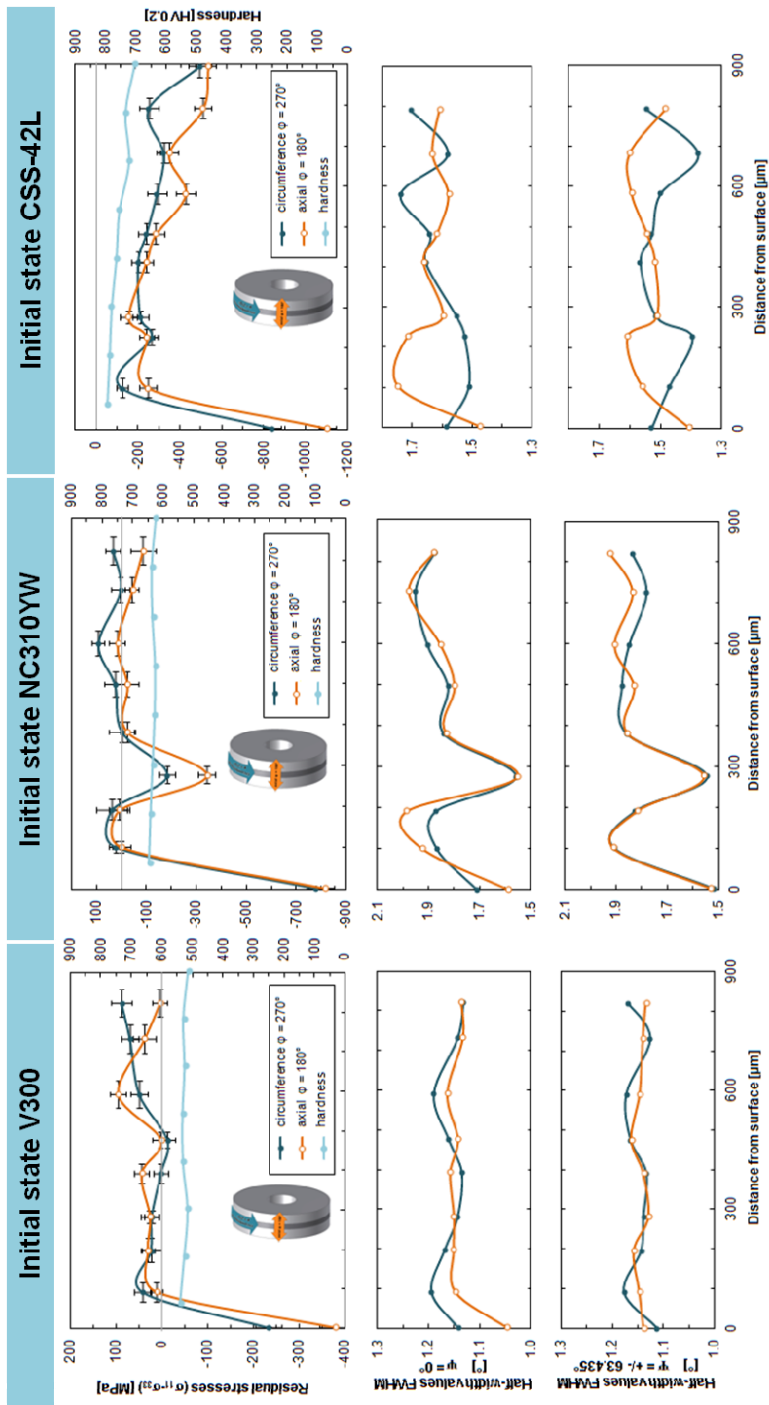


Figure 4-27: Hardness and residual stress depth profiles and corresponding FWHM values at $\psi = 0^\circ$ and $\pm 63.435^\circ$ measured with $\sin^2\psi$ -method in the initial unstressed state of V300, NC310YW and CSS-42L

Each diffraction peak has characteristic dimensions which can be used to derive physical properties, i.e. crystallite size and microstrain (residual stresses type III¹⁷). The FWHM is the width of the diffraction peak at half height of the net intensity [Spi09]. It is often observed that residual stresses and the FWHM values are correlated in the case of plastically deformed and also in mechanically surface treated metals [Hau97]. Furthermore, by means of the observed peak profile and thus also by the FWHM values, the contribution of different factors can be discussed. The following selection shows a list of factors contributing to the observed X-ray diffraction peak profile: [Gen12] [Spe12]

- Instrumental peak profile
- Plastic deformation (Plastic deformation $\uparrow \Rightarrow$ Diffraction peak width \downarrow)
- Crystallite size (Crystallite size $\downarrow \Rightarrow$ Diffraction peak width \uparrow)
- Microstrain (Microstrain $\uparrow \Rightarrow$ Diffraction peak width \uparrow)
 - Non-uniform lattice distortion
 - Faulting
 - Dislocations (Dislocation density $\uparrow \Rightarrow$ Diffraction peak width \uparrow)
 - Antiphase domain boundaries
 - Grain surface relaxation
- Solid solution inhomogeneity \uparrow : increase
- Temperature factors \downarrow : decrease

Pešička et al. showed in an investigation on the evolution of dislocation density during heat treatment and creep of martensitic ferritic steels that with a high dislocation density a broadening of the XRD peak occurred whereas a decrease in dislocation density caused a sharpening effect of the peaks [Peš03].

Therefore, the FWHM profiles were fitted at tilt angles of $\psi = 0^\circ$ and $\pm 63.435^\circ$ are additionally given in Figure 4-27. With regard to the correlation of residual stresses and FWHM the FWHM values plotted of V300 and NC310YW show an expected, typical curve characteristic. In areas of increased residual stresses, the FWHM values are decreased. Looking at the FWHM curves of CSS-42L, distinct differences between both measurement directions can be observed. A possible influence of the Cr_{23}C_6 -carbides detected on the results should be noted in this consideration.

4.3.3 Residual stresses after tribological tests at $P_{0\text{mean}} = 1.94 \text{ GPa}$

The residual stress profiles of V300, NC310YW and CSS-42L were examined under the same analytical conditions as in the initial state of the steel samples. Previous tribological tests were conducted at Hertzian contact pressures of $P_{0\text{mean}} = 1.94 \text{ GPa}$ for 10 million load cycles in VP1 at 120°C . All samples observed show compressive residual stress which are commonly reported for steels in rolling contacts (see Figure 4-28). As in case of the initial state, the maximum of residual stresses is situated directly under the surface varying be-

¹⁷ Type III stresses exist inside a grain as result of crystal imperfections within the grain

Experimental results

tween -300 MPa (V300) up to -1,000 MPa (NC310YW and CSS-42L). All steels tend to display lower residual stresses in the circumference as in the axial measurement direction. A further maximum of compressive strain can be observed in the area of depth position of maximum shear stress τ_{\max} . This approximate depth position is illustrated within the diagrams by a red vertical bar (-362 μm at $P_{0\text{mean}} = 1.94$ GPa). This is particularly evident considering the profile of V300 in Figure 4-28.

On the contrary, CSS-42L did not reveal a typical residual stress curve after testing the sample in rolling contact. The second maximum was considerably shifted towards the bulk material between 800 and 900 μm from the surface. The origin of this displacement seems to be the case carburized zone with higher hardness (800 HV) values in comparison to the core area and the other investigated materials. Due to the protective effect of the carburized layer against rolling contact fatigue, the course of the residual stress in CSS-42L can be discussed. The FWHM profiles at both tilt angles of CSS-42L were obtained as more equal than in the initial state analysis.

Concerning the FWHM values after rolling stress in comparison to the manufacturing state, no clear trend to higher FWHM values appeared. This means, the effects of increasing dislocation density, microstrain or decreasing crystallite did not contribute to a broadening of the peak profiles after cyclic loading with Hertzian contact pressures of 1.94 GPa.

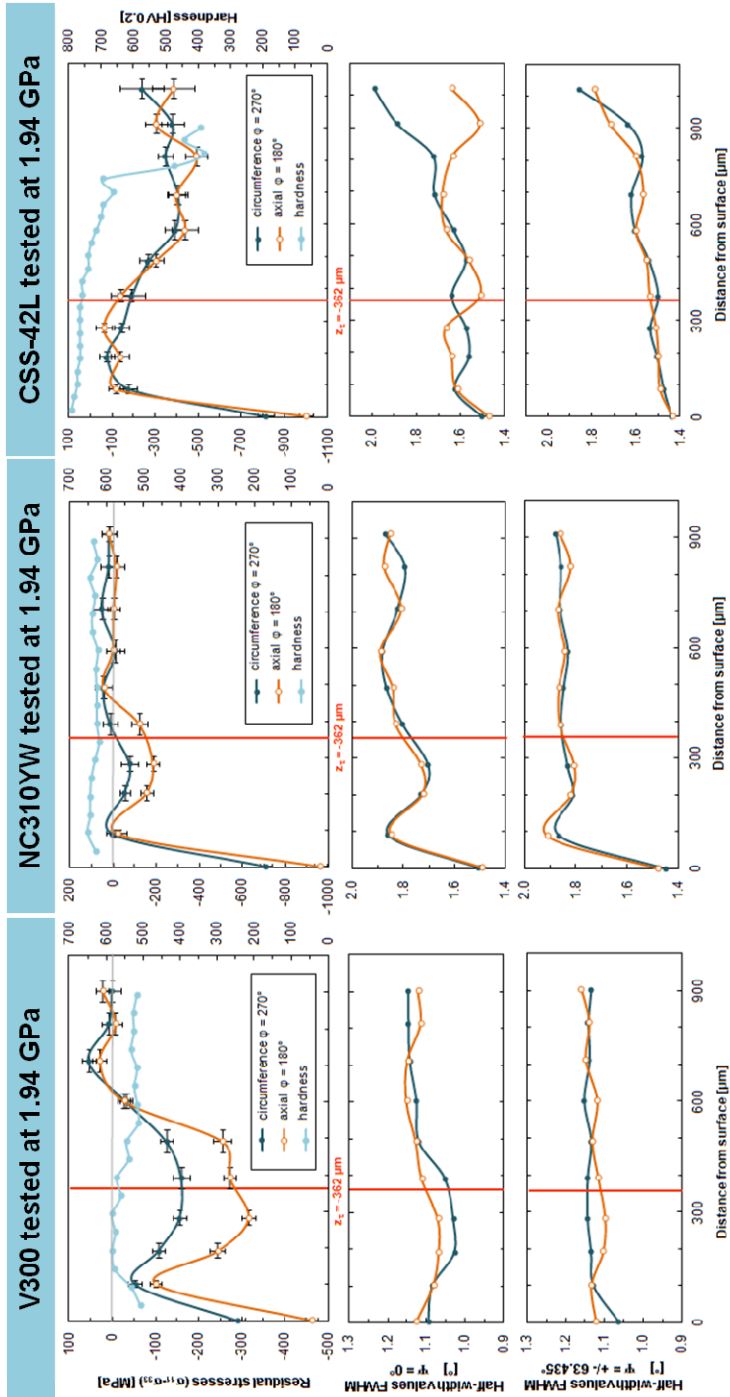


Figure 4-28: Hardness and residual stress depth profiles and corresponding FWHM values at $\psi = 0^\circ$ and $\pm 63.435^\circ$ measured with $\sin^2\psi$ -method in the initial unstressed state of V300, NC310YW and CSS-42L after tribological tests at $P_{0\text{mean}} = 1.94$ GPa

4.3.4 Residual stresses after tribological tests at $P_{0\text{mean}} = 2.5 \text{ GPa}$

Since the severest tribological tests at this time for uncoated steel samples are performed for 10 million load cycles at 120°C and $P_{0\text{mean}} = 2.5 \text{ GPa}$, the steel samples were also investigated concerning their residual stresses. In case of the steel NC310YW the demands were not bearable for the material so that the surface showed a strongly destroyed surface after relatively short testing time. The test was aborted after 1.26 million load cycles. Nevertheless, the sample failed was investigated by means of XRD as well as the other two steels reaching 10 million load cycles without failure occurrences.

Figure 4-29 demonstrates that the residual stress curves of V300 and NC310YW are clearly shaped in the area of highest shear stress values. Concerning the sample of V300 a mild increase could be detected of compressive residual stresses to -600 MPa . With increasing depth these compressive stresses pass into tensile residual stresses (at $1,000 \mu\text{m}$). Due to the failure of NC310YW, very strong compressive residual stresses could be found. In case of V300, a change became clear of the FWHM as well as NC310YW at both tilt angles at $\psi = 0^\circ$. This modification is caused by plastic deformations of the steel structures, which lead to a reduction of FWHM values. However, plastic deformations in V300 matrix can be comprehended only in partial areas of this steel.

The residual stress and FWHM curves of CSS-42L are hard to interpret just as in the initial state and after testing at 1.94 GPa (cf. Figure 4-29). Offering a FWHM after the test at 1.94 GPa of approximately 1.1 only a small change of FWHM after testing at the higher load stage of 2.5 GPa could be observed in case of steel V300.

Comparing this result with the NC310YW diffraction peak widths (~ 1.8 at 1.94 GPa) it can be assumed that the influences of higher microstrains within the NC310YW grains could cause the different material behaviors under load conditions. Furthermore in their initial states, it is clearly visible that the steel NC310YW shows a broader diffraction peak than V300 (see Figure 4-27). Therefore it is evident that NC310YW reveals a higher dislocation density before tribological testing which negatively impact the slip-rolling resistance at high loads. The formation of a maximum of compressive residual stresses at $465 \mu\text{m}$ could be observed as well as an apparently fundamental influence of existing carbides on the X-ray diffraction results.

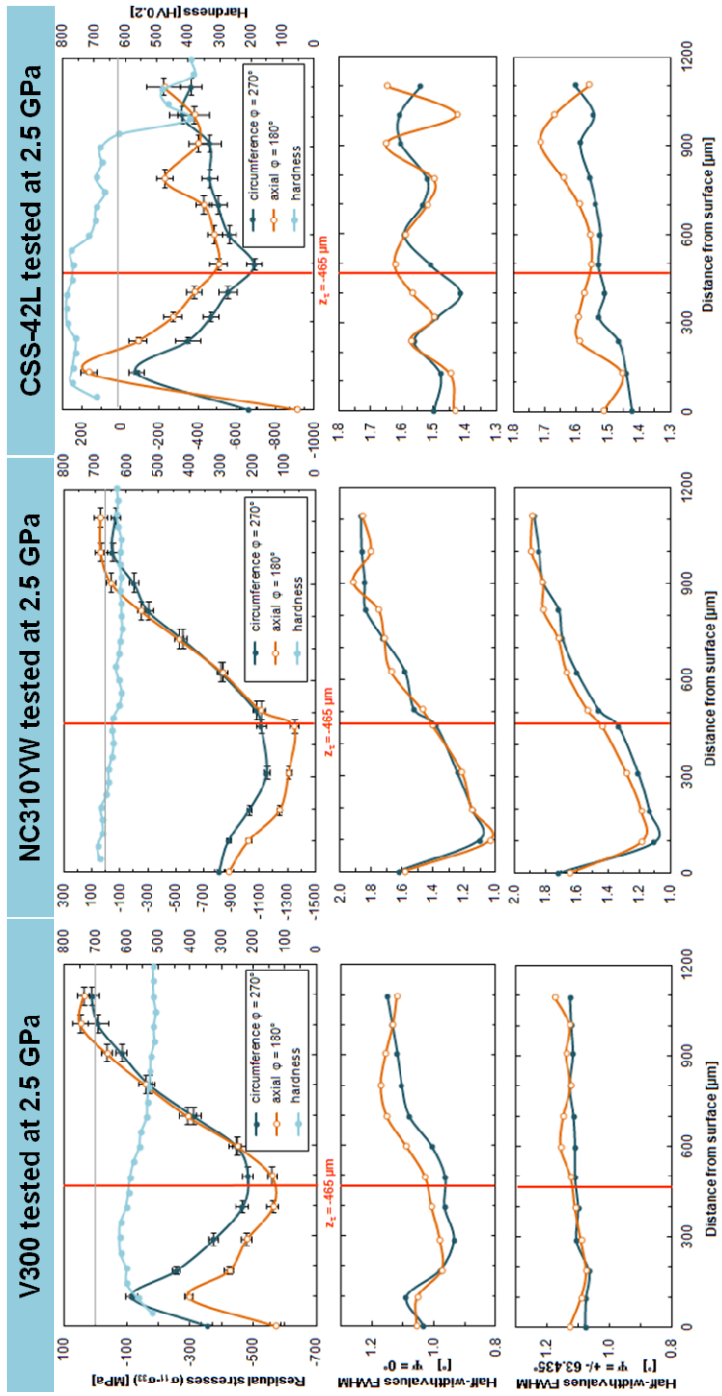


Figure 4-29: Hardness and residual stress depth profiles and corresponding FWHM values at $\psi = 0^\circ$ and $\pm 63.435^\circ$ measured with $\sin^2\psi$ -method in the initial unstressed state of V300 (left) and NC310YW (right, failure at 1.26 million load cycles) after tribological tests at $P_{\text{mean}} = 2.5 \text{ GPa}$

4.4 Structural analysis of cross sections after tests

Observations along the cross section were undertaken on mainly uncoated V300 and NC310YW steel samples by use of different techniques of microscopy. The aim of this analysis was to identify reasons for the good slip-rolling resistance of V300 and the failure of NC310YW despite the fact that both steels are nearly of similar chemical composition. Parts of this structural analysis especially in the manufacturing state were already mentioned in paragraph 3.1.3. The attention is now focused on structural changes due to slip-rolling.

4.4.1 Microscopic overview of steel structures and hardness

With optical microscopic images of the steel structures, no conspicuousness could be observed after the heat treatment. Due to literature reports of structural changes during rolling conditions, such as white etching and dark etching phenomena, the steel were investigated with regard to the structures of stressed areas and hardness depth profiles in cross section. Samples were examined after tribological tests at $P_{0\text{mean}} = 1.94$ GPa and 2.5 GPa.

By etching the cross sections of V300 and NC310YW with Nital before the microscopic examination, bright and dark looking areas became visible directly underneath the wear track. Within the microscopic images these areas and the bright and dark etching phenomena could be revealed, see Figure 4-30. These areas are stretched semicircular underneath the wear track with a broadening which is comparable to the wear track width. Extending from the surface into a depth of 490 μm (V300) respectively 400 μm (NC310YW), the position of the maximum shear stress was also included. Even with higher optical magnifications, the structural constitution cannot be resolved exactly.

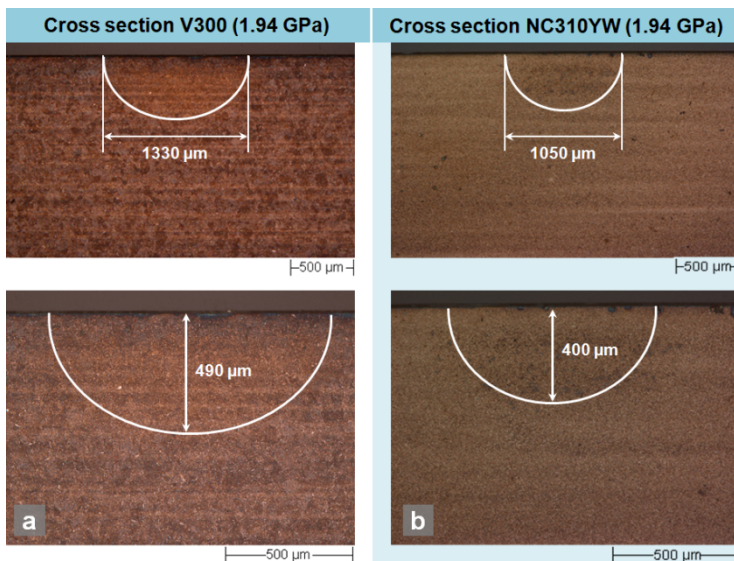


Figure 4-30: Optical micrograph taken from a) V300 and b) NC310YW cross sections after slip-rolling tests at $P_{0\text{mean}} = 1.94$ GPa (scale: 500 μm)

An indication on structural changes can be found by considering the hardness depth profiles through the areas of interest in comparison to the values of an unstressed sample (considered in Figure 4-31). Anyway, the hardness profile of V300 after 10 million load cycles confirms that up to a depth of 550 μm an increase of the hardness values can be registered. The maximum of 610 HV is well above the average value of 520 HV in the initial state. Reasonable for this hardness increase within the stressed area can be a dislocation hardening of the material. Due to plastical deformation of ductile metals, the material becomes harder and stronger. The dislocation or strain hardening phenomenon can be explained on the basis of dislocation strain field interactions. Within a deformed metal, the dislocation density increases with the grade of deformation or cold work, due to dislocation multiplication or the formation of new dislocations. As result of increasing dislocation density, the resistance to dislocation motion becomes more pronounced. [Ca107]

In the case of NC310YW, which from the outset has higher hardness values, an increase of approximately 20 HV can be detected. Thereby, it can be concluded that the strain hardening effect is not so distinct in this steel grade. The hardness depth profile of CSS-42L offered no significant difference of the values measured after test at 1.94 GPa compared to its initial state between 700 and 800 HV.

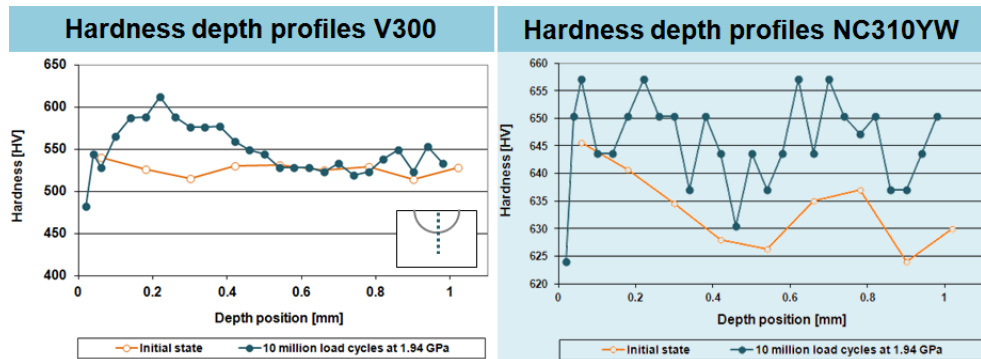


Figure 4-31: Comparison of hardness depth profiles of unstressed and under 1.94 GPa tested V300 (left) and NC310YW (right) test samples

In the light of the stringent test conditions at Hertzian contact pressures of 2.5 GPa, the aforementioned hardening effect was observed in both steels, V300 and NC310YW. Therefore, not only the hardness depth profiles but also the Hardness values parallel to the surface were plotted in Figure 4-32. The measurement of the parallel profile was performed from left to right in a depth of 250 μm . V300 presented a particularly marked hardness curve in area stressed by contact pressure. This shaping correlates with the wear track width of 2,300 μm . With regard to the sample of NC310YW it is to be noted that the tribological test was interrupted after 1.26 million load cycles. By the failure of this sample, the strain hardening effect is not so clearly visible but by means of the depth profiles identi-

Experimental results

fiable. However, the hardness decrease of CSS-42L in the depth course can be attributed to the transition of the carburized core into the martensitic case structure.

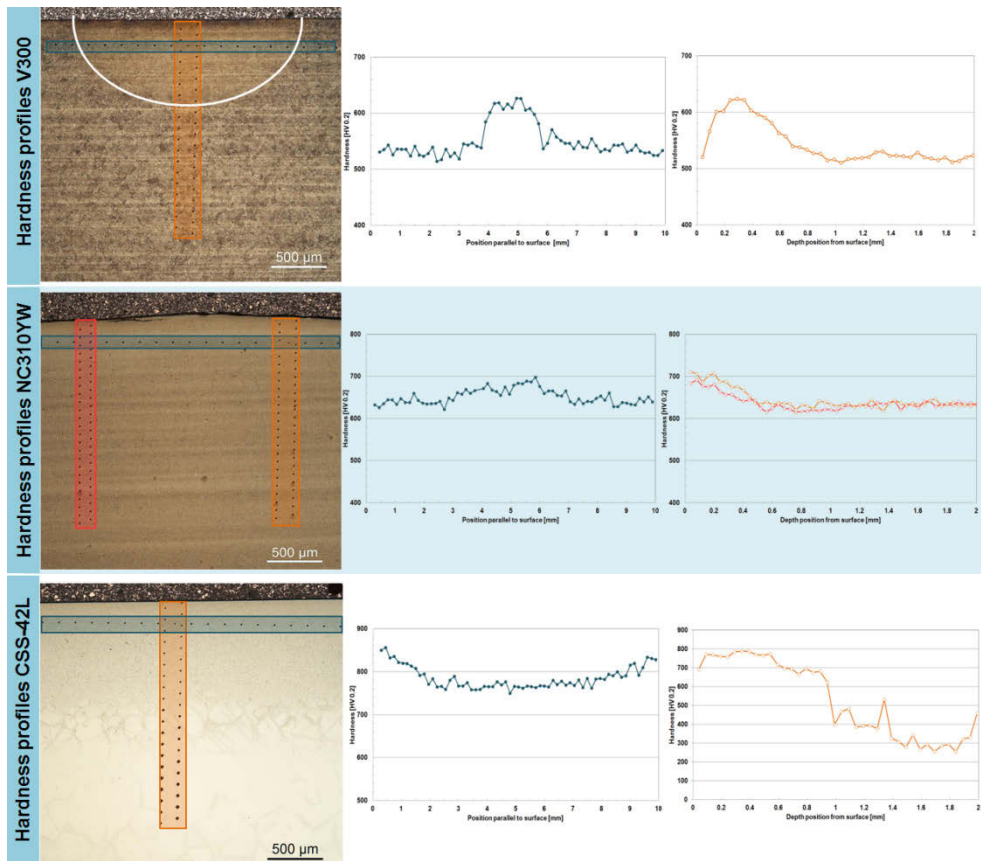


Figure 4-32: Hardness profiles of V300, NC310YW and CSS-42L measured in the depth profiles and parallel to the surface directly underneath the wear track after testing at 2.5 GPa (scale: 500 μm)

Using optical microscopy, structural characterizations of the strain hardened sections could be conducted only to a limited extent. Fine structural constituents especially cementite, silicides or bainitic microstructures are more precise and easier detectable by scanning electron microscopic methods.

4.4.2 Further structural investigations (SEM, FIB/ TEM)

Further SEM/EDX and FIB/TEM investigations present a structural comparison of the two steels V300 and NC310YW as well as a comparison of stressed and unstressed bulk material of both materials. The different strain hardening behaviors (confer paragraph 4.4.1) of V300 and NC310YW suggest that a specific difference exists.

In the first structural overview of the unstressed material both samples displayed a mainly martensitic structure, more precisely of lath martensite (cf. Figure 4-33). Lath martensite is

typical for low-carbon steels ($C < 0.4$ wt.-%) and is composed of bundles of parallel arranged lathlike martensite crystals. The length dimension of these laths reaches up to a few μm whereas the width lies between 0.1 and 0.5 μm [Löp06]. In Figure 4-33 d the former austenite grain boundaries are well recognizable (orange arrows). Comparing the structures of both steel grades, NC310YW revealed a finer microstructure. Moreover, the dark areas in the V300 matrix, along former grain boundaries, were firstly indicated as ferrite ($\alpha\text{-Fe}$). Due to these ferritic grains, the microstructure of V300 the average grain size is larger and above all less uniform as in case of NC310YW.

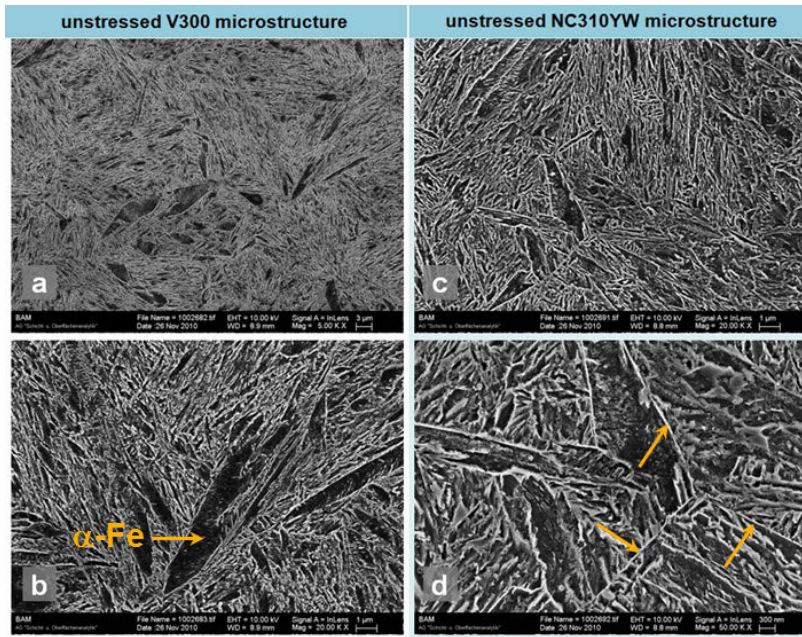


Figure 4-33: SEM overview in cross section taken from unstressed V300, images a) and b), and NC310YW, images c) and d), microstructures (scale: a) 3 μm , b),c) 1 μm and d) 300 nm)

According to the researches of Callister [Cal07] and the technical steel research of Zajac et al. [Zaj05], the ferritic grains showed a great similarity to bainitic microstructures. The effect of silicon contents in steels on bainite formation was previously reported in paragraph 0. Now, it is important to classify these structures either as martensite/ferrite or bainite. A review of all morphologies identified as bainitic structures is given in Table 4-2. The exposure of obviously small differences in microstructure and phase mixtures is possible to resolve by modern analysis methods. In literature five morphologies of bainite had been recognized: granular bainite, upper bainite, degenerated upper bainite, lower lath-bainite and lower plate-like bainite. With regard to [Oht90], bainite is classified and divided into the morphology of ferrite and the type as well as distribution of second phase. Nowadays, the production of high-strength steels is performed by quenching processes, moderate cooling

Experimental results

and normalizing which lead to a steel microstructure composed of various kinds of transformation products such as martensite, ferrite and even bainite [Oht90].

Table 4-2: Schematic representation of different bainite morphologies according [Zaj05], [Miy11], [Miy11-2] and [Tak12]

Classification	Shape	Morphology	Precipitation site of Fe ₃ C	Bainite structure
Granular Bainite (GB)	granular	Irregular ferrite with martensite Second phase can be pearlite or bainite	No precipitation	
Upper Bainite (UB)	lath	Lath-like ferrite with cementite on lath boundaries	Precipitation at the grain interface	
Degenerated Upper Bainite (DUB)	lath	Lath-like ferrite with martensite on lath boundaries. Second phase can be pearlite or bainite	No precipitation	
Lower Lath Bainite (LLB)	lath	Lath-like ferrite with cementite inside the ferrite laths	Precipitation inside the laths	
Lower Plate-like Bainite (LPB)	plate	Plate-like ferrite with cementite inside the ferrite plates	Precipitation inside the grains	
Lath Martensite (ML)	lath	Tempered lath martensite	Precipitation inside the laths	

Thus, the identification of these fine microstructures becomes very difficult. L apple as well voices the opinion of nearly equal martensite and lower bainite appearances. Typical for lower bainite is the precipitation of long shaped Fe_3C crystals within the ferrite plates under distinct angles of 50° up to 60° to the main axis of ferrite. In contrast, upper bainite is composed of bainitic ferrite arranged side by side in bundles. Between ferrite plates long shaped Fe_3C carbides are precipitated. [L ap06]

If the structures found by SEM observations inside the microstructure of V300 and NC310YW are of bainitic origin (Lower Plate-like Bainite), Fe_3C carbides as well as higher carbon contents will be verifiable. Therefore local EDX spectra of selected ferritic plates were taken and analyzed in view of the contained carbon. The measurement points are illustrated in Figure 4-34 b. Figure 4-34 demonstrates the comparison of bainitic structure given by Callister [Cal07] and V300 microstructure. An arrangement of Fe_3C in 50° up to 60° angles to the ferritic matrix is indistinguishable in the image of Callister (Figure 4-34 a).

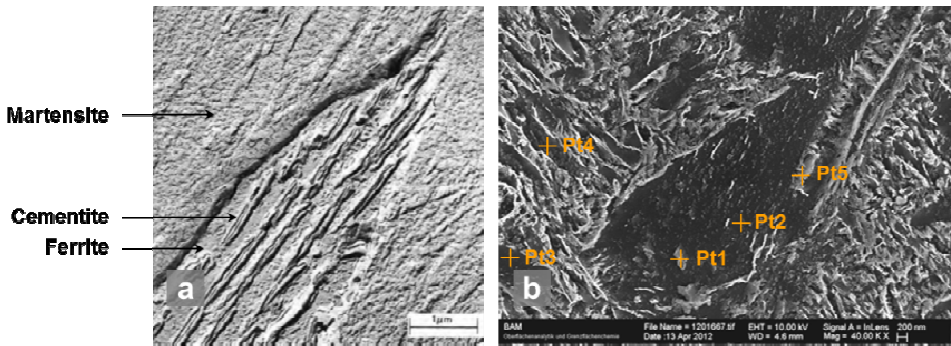


Figure 4-34: a) Transmission electron micrograph of bainitic structure (combination of cementite and ferrite) according Callister [Cal07] and b) SEM image of V300 microstructure with EDX measurement positions Pt1 to Pt5 (scale: a) 1  m and b) 200 nm)

The percentage of carbon mass on the total Fe_3C mass is data 6.69 % due to literature [L ap06]. The results of EDX analysis showed in Table 4-3 revealed more or less equally distributed carbon contents.

Table 4-3: Carbon content of analyzing points Pt1 - Pt5 in V300 microstructure by EDX (wt-%)

	Pt1	Pt2	Pt3	Pt4	Pt5
Carbon content [wt-%]	1.26	1.09	1.83	1.48	1.56

Therefore, it can be concluded that the individually measured points represent no carbide structures. However, due to the higher silicon contents, the precipitation of iron carbides is partially prevented [Bha79] and as a result Fe_3C structures are of very small sizes. Even in the case of NC310YW, higher carbon contents of distinct areas could not be detected.

Experimental results

SEM investigations of microstructure areas stressed in slip-rolling tests at $P_{0\text{mean}} = 2.5$ GPa offered an obvious change in the microstructure. Big ferritic plates found previously in the initial state in V300 matrix are not traceable due to slip-rolling influences. Furthermore, with the increase of hardness in stressed area, a microstructure refinement is associated with the slip-rolling influence (compare Figure 4-33 and Figure 4-35). On the other hand NC310YW offered a reinforcement of microstructure refinement. Figure 4-35 b shows the directly stressed and cracked area including a crack parallel to the surface in a depth position of approximately $12\ \mu\text{m}$. The structure above the crack is comparable to a cold worked microstructure with a preferential rolling direction.

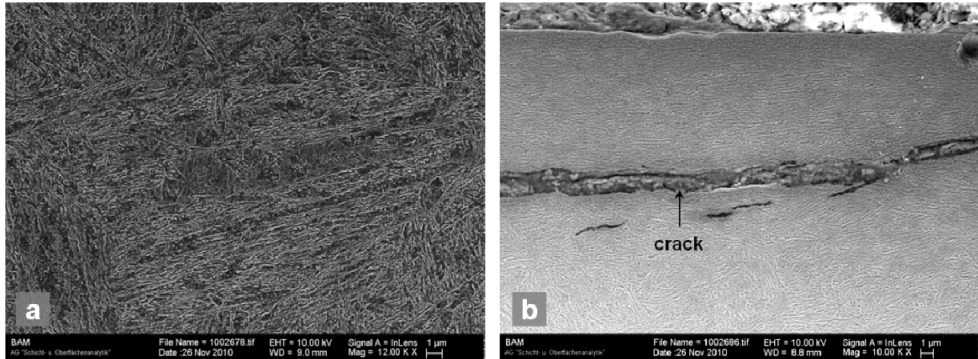


Figure 4-35: SEM images underneath the wear track after tribological tests at 2.5 GPa of a) V300 and b) NC310YW (scale: $1\ \mu\text{m}$)

Clearer information about the structural composition of both steels will come from FIB/TEM analysis. These further analysis started by using Focused Ion Beam (FIB) for cross section imaging in the resulting groove and for further processing in TEM lamellae. Their preparations were conducted by focused ion beam technique in combination with in-situ lift-out method in the BAM working group “Materialography, Fractography and Ageing of Engineering Materials” of Dr. W. Österle. In the same manner, a structural comparison of both steels (V300 and NC310YW) as well as the unstressed and stressed state ($P_{0\text{mean}} = 1.94$ GPa for 10 million load cycles) was performed by means of FIB milling (only V300 is presented) and TEM. The illustrations in Figure 4-36 show cross sectional profiles of V300 in unstressed and stressed structure area carried out by FIB. Without any doubt, a structure refinement is distinct particular visible comparing the FIB grooves in Figure 4-36 c and d. Here, the grain boundary of former austenite grains are on the one hand identifiable and in stressed state no more detectable. Ferrite grains in the non-deformed area are particularly of sizes up to $5\ \mu\text{m}$. An additional characteristic is a fine needle-shaped texture of different orientation systems.

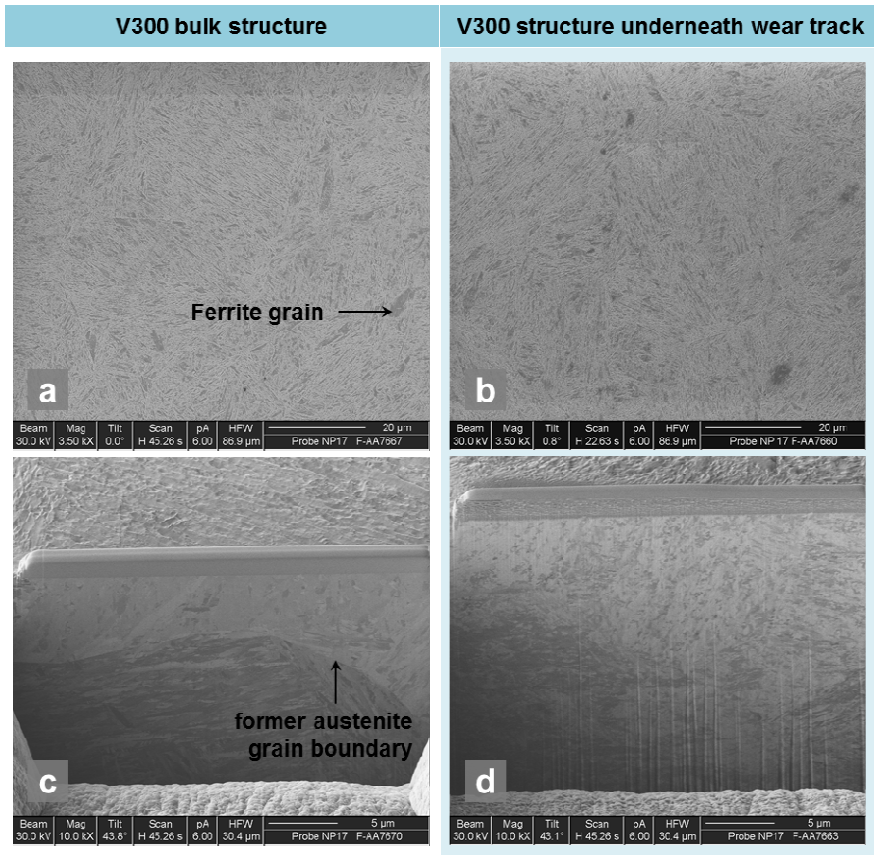


Figure 4-36: SEM pictures and FIB cross sections of a) V300 bulk structure and b) observed structure underneath the wear track (scale: a), b) 20 μm and c), d) 5 μm)

Considering the TEM cross section overview, unstressed and non-deformed V300 structure areas exhibit two characteristic areas (cf. Figure 4-37). The dark contrasted area is on the hand conform to the presence of uniformly orientated ferrite grains in [011]-orientation and on the other hand consistent to form and dimensions of dark grey areas shown in FIB-images. According to SAED (selected area electron diffraction) pattern, the brighter grey area surrounding the ferritic plates corresponds to lath martensite in the same orientation but with weak additional reflections of $g = n/3$ (211) type (see left image in Figure 4-37). Due to low content of dissolved carbon and tempering treatment (precipitation of iron carbides), the martensite included reveals the same crystal structure as ferrite (α -Fe).

Experimental results

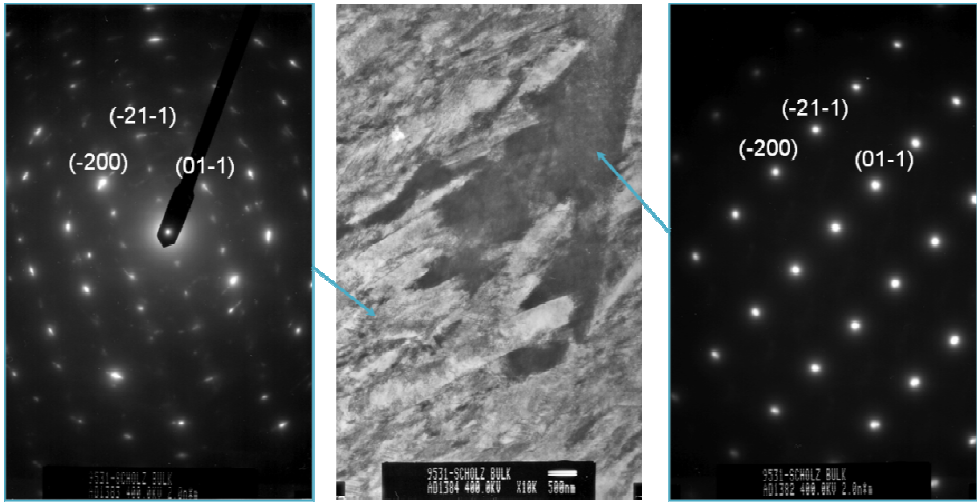


Figure 4-37: Selected area electron diffraction pattern taken from V300 TEM overview image including characteristic orientations (scale: 500 nm)

On contrary in Figure 4-38 a, TEM picture and the corresponding SAED pattern are shown of stressed V300 microstructure (area of increased hardness after slip-rolling under $P_{0\text{mean}} = 1.94 \text{ GPa}$) including lath martensite in $[001]$ -orientation. Ferrite could not be observed in the same extent found in the unstressed V300 microstructure. In addition to martensite, weak reflections can be detected related to carbide structures of Fe_3C . The low intensity in dark field imaging suggests that the carbides which are of very small dimensions. It can be assumed that different variants of austenite-ferrite-transformation processes occurred in alternating laths. An overlapping of different crystal orientations is not recognizable within the diffraction image. Due to rolling contact stress and combined partial plastic deformation, small arcs of $\alpha\text{-Fe}$ reflections became visible (continuously changing in orientation inside the bent volume).

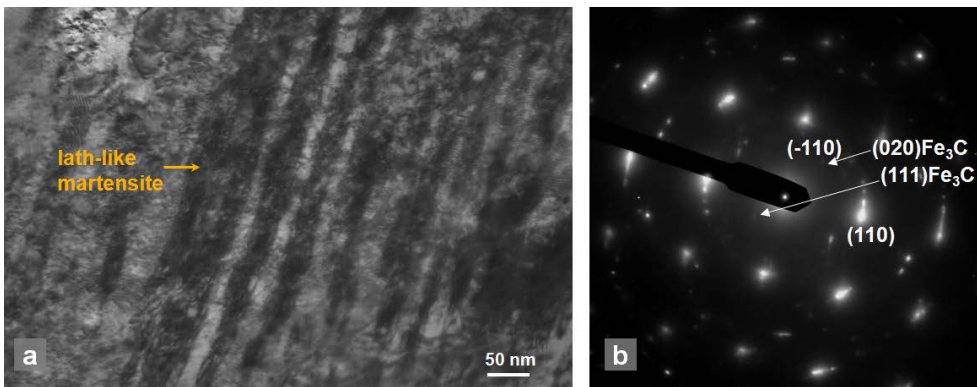


Figure 4-38: TEM overview of stressed V300 lath martensitic microstructure (area of hardness increase) and corresponding SAED pattern (scale: 50 nm)

It seems that, areas of granular bainite arised (Figure 4-39 a and b) in the heat treatment during the cooling stage before martensitic formation. This behavior is similar to ferrite grains formed at former austenite grain boundaries. Further diffraction analysis showed the presence of intensive α -Fe reflections and weak circular reflections of Fe_3C (012) and (210). The diameter of the iron carbides in (012)-direction was found to be 0.281 nm whereas (210)-direction revealed diameters of 0.207 nm. Even the micro twins detected are surrounded by granular bainite.

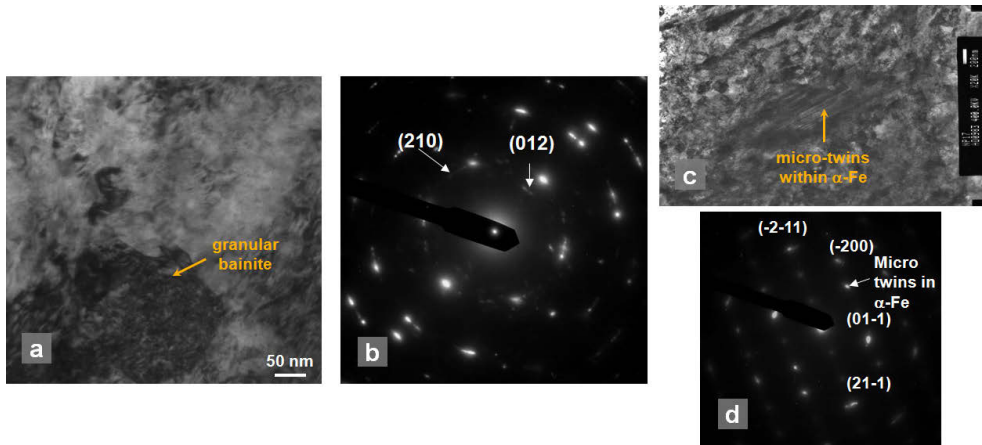


Figure 4-39: TEM and SAED images of granular bainitic structures (a, b) found in stressed V300 microstructure and micro twins within the ferrite structure in [011] orientation (c, d) (scale: a) 500 nm, c) 200 nm)

The structure of NC310YW presented in Figure 4-40, taken at the same magnification as V300 shown in Figure 4-37, is. The main characteristics of the area captured are a great variety of lath orientations and no detectable ferrite plates along former austenite grains. It can be distinguished from V300 microstructure that no granular bainite is detectable. However, diffraction pattern of NC310YW revealed the same microstructural features as V300. Additional reflections of $g = n/3$ (211) and the respective diffraction pattern are recognizable. Interpreting the SAED diffraction image in Figure 4-40, laths of alternating transformation variations can be observed. Light reflections marked by yellow arrows in Figure 4-40 suggest that Fe_3C -carbide in (110) and (112) directions are present. The grain sizes were found to be 0.338 nm (110) and 0.239 nm (112). Considering the SAED interpretation of NC310YW twin relations can be observed as well as overlapping of different ferrite orientations. In Figure 4-40 particular the overlapping is reported of two [110] areas turned with an angle of 70° against each other. The structural investigation has also established that no residual austenite exists in the area analyzed.

Experimental results

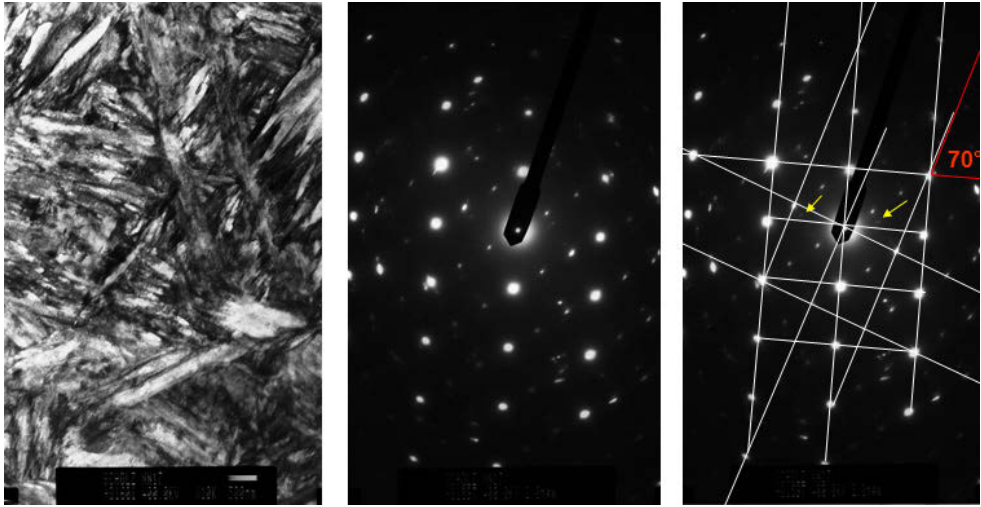


Figure 4-40: Selected area electron diffraction pattern taken from NC310YW TEM overview image including the interpretation of one lath colony diffraction pattern (scale: 500 nm)

Concluding FIB/TEM and SAED investigations of the steel grades V300 and NC310YW, shared structural features but mainly differences are recognizable. Both steels revealed a martensitic lath structure with alternating twin orientations due to different transformation variants described by Kurdjumow-Sachs [Kur30]. The laths offered in principle a high density of dislocations, but contain carbide precipitations as well (tempered microstructure). This kind of structure is caused by quenching and annealing or is due to isothermal transformation within the bainitic stage. In both cases, contents of residual austenite were not detectable.

The structural considerations of both steel microstructures are gathered in the following points:

- Whilst the structure of NC310YW consists mainly of laths with homogeneous fine grain sizes, the structure of V300 additionally contains low amounts of ferrite and granular bainite. Due to this fact, the grains of V300 are larger and less homogeneous in size. The slip-rolling motion induces a deformation of ferritic structures by means of twin formation.
- The formation of ferrite in V300 along former austenite grain boundaries appears to already existing structures before bainitic and martensitic transformation started.
- Assuming that the heat treatment of both steels is almost the same (see Figure 3-2: Schematic heat treatment curve of the 100Cr6H, Cronidur 30, V300, NC310YW and CSS-42L materials) the change in transformation behavior could alternatively be explained by the slightly different chemical composition. An increase of silicon, chromium and molybdenum contents lead to a stabilization of ferrite which results in an increase of ferrite during the cooling process. It can be con-

cluded that higher content of nickel in NC310YW stabilizes austenitic structures and thus the effect of ferrite stabilization was overcompensated.

- The high hardness with simultaneous high ductility of NC310YW can be ascribed by the very fine and homogeneous lath-like structure. Due to higher silicon contents the diffusion of carbon is restricted so that the precipitation of Fe_3C has not progressed as far as in case of V300. Even the stability of the lath structure during tempering can be described in this way. The hardness increase of V300 within the stressed area correlates with the formation of micro-twins inside the ferrite grains. Assuming this fact and the lower dislocation density V300 reveals a still higher solidification potential.
- With the absence of retained austenite in both structures even on nanoscale, the presence of NANOBAIN, reported by Caballero in [Cab11], can be excluded. NANOBAIN transforms at low temperature (125 – 350°C) which leads to nanoscale microstructures consisting of nanoscale (20 – 60 nm) crystals of bainitic ferrite (α), retained austenite (γ) and some martensite. The silicon content, which is comparable amount for V300 and NC310YW, suppresses the precipitation of brittle cementite during bainite formation. Hence, this should lead to an improvement in toughness.

Interesting for the structural consideration is the distribution of silicon within the steel matrix. With the help of EDX element mapping and images at a large magnification, the silicon distribution in V300 and NC310YW could be revealed (cf. Figure 4-41). Clearly visible is the very fine arrangement of silicon in both steels. It might be argued that the silicon atoms substituted relatively homogeneous the iron atoms within the bcc-lattice despite of their larger atomic radius of 1.18 Å compared to carbon 0.71 Å (specified in detail in paragraph 2.3).

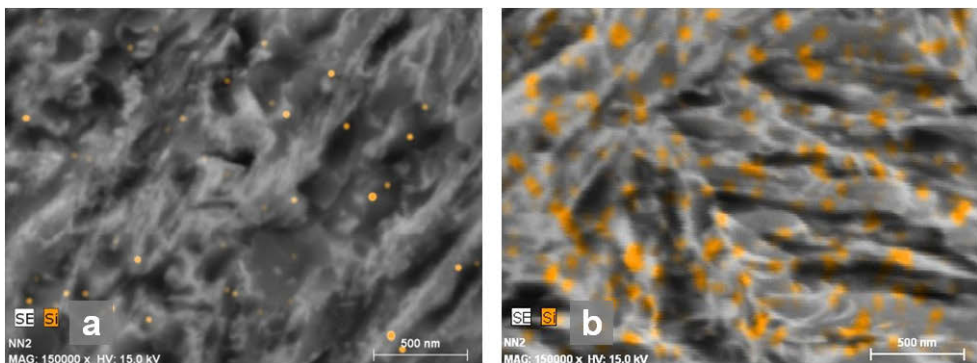


Figure 4-41: Silicon distribution in structure of a) V300 and b) NC310YW observed by means of SEM/EDX measurements

Using TEM observation in combination with an EDX system, a closer look at the silicon content at ten characteristic points in NC310YW matrix is presented in Figure 4-42. Not

Experimental results

considering Point 4 and 5, which were detected as aluminum and copper foreign particles, the silicon contents complies with the nominal composition (according to the measurement uncertainty). Hence the fine silicon distribution observed by means of EDX could be confirmed. Formations of silicon-enriched zones at the interface between ferrite and cementite phases, as described in [Cha84], were not detectable with both analysis methods.

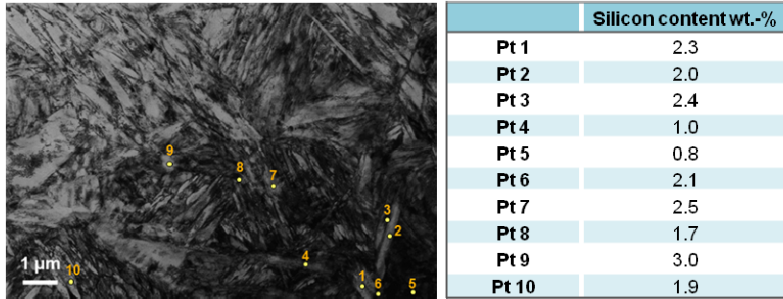


Figure 4-42: Quantitative EDX-analysis of characteristic TEM points in NC310YW steel matrix and the corresponding content results (scale: 1 μm)

4.4.3 c_m/a_m ratio and soluted carbon content in V300 and NC310YW

It is well known that martensite has a body centered tetragonal structure. In order to denote the tetragonal distortion of martensitic structures the ratio c_m/a_m can be evaluated by means of synchrotron X-ray radiation. The distortion of the martensite lattice is induced by dissolved carbon atoms. Therefore, the 200 reflection peak of martensite was chosen to obtain the c_m/a_m ratio in the steels V300 and NC310YW. The parameters of the measurements at Beamline MAXIM at DESY (Hamburg) are given in Table 4-4.

Table 4-4: Parameters of synchrotron X-ray measurements at DESY (Hamburg) of the steels V300 and NC310YW

Parameters	Values
λ	0.179021 nm
2θ	$74^\circ - 80^\circ$
$\Delta 2\theta$	0.01°
ψ	0°
$t_{\Delta 2\theta}$	~ 5 s
reflex	Fe 200
ω	$2\theta/2$
$\Delta\omega$	$\Delta 2\theta/2$
φ	0°
collimator	9.0×2.0 mm ²

Since martensite has a tetragonal structure, the 200 reflection peak has an asymmetric shape. Using Voigt functions the diffraction reflex can be separated into two reflection curves. After fitting the curves the 2θ -value of each reflection can be used to apply Bragg's

law [Bra13]. Thus the lattice spacings c_m and a_m could be determined. The parameters c_m and a_m can be quantitatively evaluated with the following equations [Vöh77]:

$$a_m = 2.8668 - 0.013 \text{ wt. } \%C \quad (4.5)$$

$$c_m = 2.8668 + 0.116 \text{ wt. } \%C \quad (4.6)$$

$$c_m / a_m = 1 + 0.046 \text{ wt. } \%C \quad (4.7)$$

In martensite transformation, the dissolved carbon induces a lattice distortion in order to produce a body centered tetragonal structure whose c_m/a_m ratio increases, if the carbon content increases [Wan02-2]. The 200 reflections of V300 and NC310YW are presented in Figure 4-43. Considering the profiles it can be argued that under the assumption of a tetragonal distorted lattice, no deviations from the adjusted profile are detectable. The lattice measured offered only a slight tetragonal distortion.

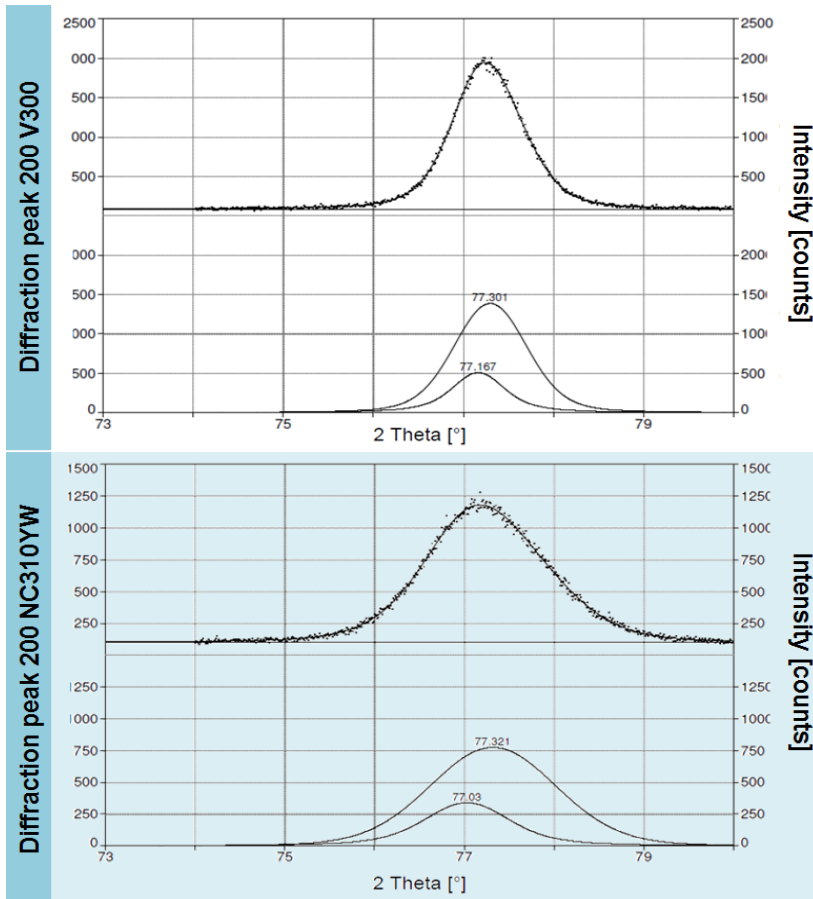


Figure 4-43: 200 reflex diffractogram of the steels V300 and NC310YW including the fitted tetragonal distorted diffraction profile

Experimental results

According to the correlation between c_m/a_m ratio and the soluted carbon content revealed by the Vöhringer equations (4.5 – 4.7) [Vöh77], the soluted carbon content in both steels was calculated. The evaluated values of the c_m/a_m ratio and dissolved carbon can be found in Table 4-5. It becomes visible that the content of dissolved carbon in NC310YW with 0.069 wt.-% is higher than in comparison to V300 with 0.032 wt.-%. According to Kurdjumov et al., the tetragonality of NC310YW is greater due to the higher content of dissolved carbon [Kur75].

Table 4-5: Results of the calculated c_m/a_m ratio and dissolved carbon content of the steels V300 and NC310YW

V300		NC310YW	
c_m/a_m	wt.-% Carbon	c_m/a_m	wt.-% Carbon
1.0015	0.032	1.0032	0.069

In general, tempering affects the structural behavior of martensitic steels. Cheng et al. [Che88] and Lucas et al. [Luc69] investigated the tempering behavior of iron-carbon martensite by means of dilatometric and calorimetric analysis. At least they found find different stages of structural changes during the tempering process of iron-carbon martensite. Each stage is accompanied either by an increase of the material volume or a volume contraction (cf. Figure 4-44).

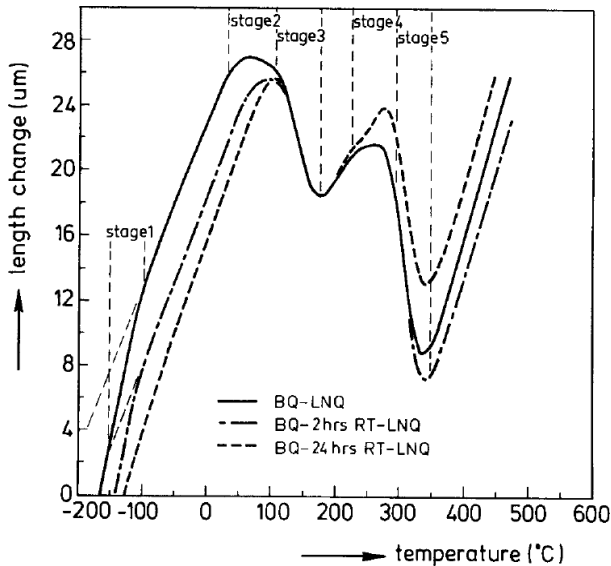


Figure 4-44: Dilatometer curves of different iron-carbon martensite steel grades showing the different stages of structural changes during tempering [Che88]

Due to the higher proportion of tetragonal distorted martensite and retained austenite in NC310YW two possible effects at higher operating or deposition temperature according Cheng and Lucas could occur:

- I. Transformation of tetragonal distorted martensite in cubic martensite at temperatures between 80 and 200°C (stage 3 in Figure 4-44). This stage involves the precipitation of transition carbides (e/n carbide) leaving a ferrite matrix containing the segregated carbon atoms [Che88]. This process step leads to a volume contraction.
- II. Decomposition of retained austenite at temperatures between 240 and 320°C. This process causes a small volume increase. [Che88]

Both effects could have a negative impact on the slip-rolling resistance of uncoated and coated steels operating at higher temperatures. Using oil heated up to a temperature of 120°C in the slip-rolling endurance tests the residual content of tetragonal distorted martensite could be transformed into cubic martensite during the test leading to higher residual compressive stresses due to the volume contraction [Luc69]. The deposition of DLC coatings for example at temperatures around 300°C could induce the decomposition of retained austenite during the coating process. Thus, the volume increase of the steel substrate material could lead to unwanted stress states within the coating and reduced coating adhesion.

5 Discussion and tribological considerations

In the present work, the slip-rolling resistances as well as the wear behavior of different materials and coatings were studied intensively. It could be proven that the choice of high toughness steels not only has positive aspects for the slip-rolling resistance, it also favors the interaction with the lubricant for low friction by the formation of tribo-reactive films in the case of V300.

Table 5-1 sums up the properties of the newly applied steels V300, NC310YW and CSS-42L revealed in tribological tests and structural analysis. Positive aspects are highlighted green and negative aspects red with regard to structural, mechanical and tribological properties. The special features are the high toughness and hardness values of these steels tested in the current research even at higher operating temperatures. As for Cronidur 30, the hardness of the high toughness steels tested remains stable until 300 °C and above, so the steels properties will not be affected by optional PVD or CVD coating processes.

Considering the mechanical properties (hardness, toughness, strength) of the steels aforementioned, it can be concluded that the slip-rolling resistance does depend on these properties in case of uncoated steels. The toughness as ability to absorb energy and plastic deformation without fracturing and crack growth allows withstanding high contact pressures applied in slip-rolling tests. Indeed, the slip-rolling resistance depends not only on the mechanical properties on its own. In the case of NC310YW, an adjustment of the heat treatment to lower hardness values may favor the slip-rolling resistance due to lower initial dislocation density. High dislocation or twin densities in the materials do not allow much scope to withstand high stresses by strain hardening effects. The higher dislocation density of NC310YW in comparison to V300 was revealed by means of XRD and FIB/TEM analysis as reported in section 4.4.2.

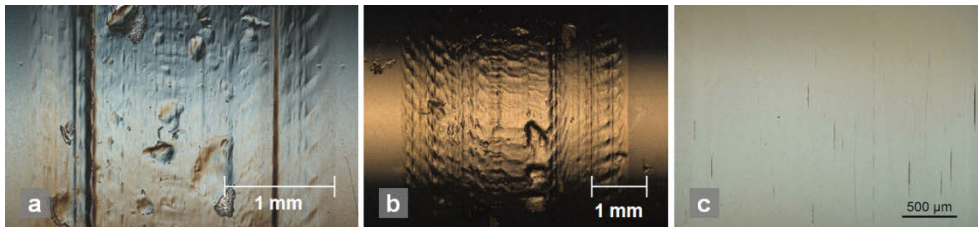


Figure 5-1: Restriction of the slip-rolling resistance of a-C:H coatings due to plastic deformation and flow of steel substrates presented in a) 100Cr6H and b) Cronidur 30 tested at 1.94 GPa and comparatively c) the high slip-rolling resistant coating BMW 4 on CSS-42L tested at 2.5 GPa for 18 days (scale: a), b) 1 mm and c) 500 μ m)

A proper metallurgical adhesion of thin film coatings on the substrate surface is essential for highly loaded tribological system. This is achieved by deposition temperatures in the range of 300 and 400°C enabling the formation of a diffusion layer between substrate and coating. Moreover, it is for all substrates important that the deposition process does not affect the mechanical properties. Otherwise failures of the tribological system such as flaking of the

coating or plastic deformation of the substrate could occur as shown in Figure 5-1. Surface defects such as this revealed in former investigations [Spa05] could not be observed for the new steels in combination with DLC's and Zr(C,N). Due to the high annealing temperatures of these steels, the process temperature had no influence on the mechanical properties. Furthermore, the ability is remarkable of the thin film coatings to withstand plastic deformation of the substrate in a certain limit (illustrated in Figure 5-1).

Table 5-1: Summary of the global structural and tribological profiles of the steels V300, NC310YW and CSS-42L observed in this work

	V300 (1.8062)	NC310YW (40SiNiCrMo10)	CSS-42L (AMS 5932)
Structural and mechanical properties	<ul style="list-style-type: none"> High level of hardenability Metallurgical manufacturing processes with low oxygen concentration required (SiO₂ formation) Adequate strength and ductility values for heavy workloads Simple heat treatment generating high annealing resistance and structural stability up to 400°C (structural stability) Low residual austenite content (below detection limit of ~2.5 vol.-%) increasing the structural stability (no austenite decomposition) Martensitic lath-like structure with alternating twin orientations containing small amounts of granular bainite and Fe₃C carbides Formation of structural changes classified as dark etching areas underneath stressed areas 	<ul style="list-style-type: none"> High level of hardenability (app. 57 HRC) Metallurgical manufacturing processes with low oxygen concentration required (SiO₂ formation) High strength and toughness for use in mechanical parts with high stresses Advanced heat treatment including sub-zero cooling and two-times annealing at 300°C Low residual austenite content of ~5.2 vol.-% requiring good toughness properties (typical for bearing and gear steels) Very fine and homogeneous lath-like martensitic structure without Fe₃C carbides 	<ul style="list-style-type: none"> Very high level of hardenability due to case carburizing up to 68 HRC Double vacuum melting process VIM-VAR required High strength properties while retaining good core ductility ($K_{IC} > 120 \text{ MPa} \cdot \text{m}^{1/2}$) Complex heat treatment with a duration of 55 h at high annealing temperatures (structural stability up to 550°C) Low residual austenite content (~3.2 vol.-%) Typical case carburized microstructure No structural changes observed
Tribological properties (friction and wear)	<ul style="list-style-type: none"> Suitable for all friction reducing PVD-/CVD-coating processes even at higher deposition temperatures without loss in mechanical properties (hardness) High slip-rolling resistance at least to 10 million load cycles at $P_{\text{mean}} = 2.5 \text{ GPa}$ and 120°C oil temperature Achieved low friction values of 0.04 with uncoated surfaces in engine oil at 1.5 GPa in the same range as DLCs vs. steels Comparable wear rates to 100Cr6H and Cronidur 30 in the uncoated state at higher contact pressures (better at 1.5 GPa) Improved wear properties by application of DLC coatings Formation of low friction tribo-reactive thin films possible High level of slip-rolling resistance, low friction and wear values in combination with a-C-H coatings (BMW and KYB Corp.) 	<ul style="list-style-type: none"> Slip-rolling resistance at least to 10 million load cycles at $P_{\text{mean}} = 1.94 \text{ GPa}$ and 120°C oil temperature Medium friction reduction in comparison to 100Cr6H and Cronidur 30 by use of engine oil Comparable wear rates to 100Cr6H and Cronidur 30 in the uncoated state at higher contact pressures Improved wear properties by application of DLC or Zr(C,N) coatings Formation of low friction tribo-reactive thin films possible to a limited extent High level of slip-rolling resistance, low friction and wear values in combination with a-C-H coatings (BMW and KYB Corp.) 	<ul style="list-style-type: none"> High slip-rolling resistance at least to 10 million load cycles at $P_{\text{mean}} = 2.62 \text{ GPa}$ and 120°C oil temperature Medium friction reduction in comparison to 100Cr6H and Cronidur 30 by use of engine oil Comparable wear rates to 100Cr6H and Cronidur 30 in the uncoated state at higher contact pressures Improved wear properties by application of DLC or Zr(C,N) coatings No tribofilm formation observed High level of slip-rolling resistance, low friction and wear values in combination with a-C-H coatings (BMW and KYB Corp.)

Positive aspects observed ■ Negative aspects observed ■

Discussion and tribological considerations

The following chapters discuss the results revealed in the present work. As aforementioned, aspired goals such as reduction in friction and improved load carrying capacity should be achieved by different optimization approaches (see Figure 1-2). Therefore the influences of high toughness steels, thin film coatings and lubricants are considered in detail. Particularly, the tribological performance of alternative lubricants (polyglycols) is compared with the results achieved by using synthetic engine oil.

5.1 Influence of alternative steels

Considering the evolution of the coefficient of friction as function of the test duration (10 million load cycles) in endurance tests conducted in the present work, the tribological benefit of the alternative steels becomes clearly visible (see Figure 5-2). As test parameter, a contact pressure of $P_{0\text{mean}} = 1.5 \text{ GPa}$ at 120°C lubricant temperature was chosen. In comparison to conventional bearing steel, such as 100Cr6H and Cronidur 30, the steel grade V300 could reduce the friction values by approximately 25 %. In order to confirm the test results of V300 the test was repeated under the same conditions. Consequently, the low friction values of V300 down to 0.05 could be reproduced. In the light of this comparison it may be concluded that a reduction of friction by an optimal choice of interacting materials could be achieved. With regard to different varying degrees of material interactions revealed the tribo-system could made more effective, compatible and consistent. Another interesting aspect in this view is that NC310YW compared with the conventional steels also offered a friction reduction, but not to the same degree as V300, although it has nearly an identically chemical composition.

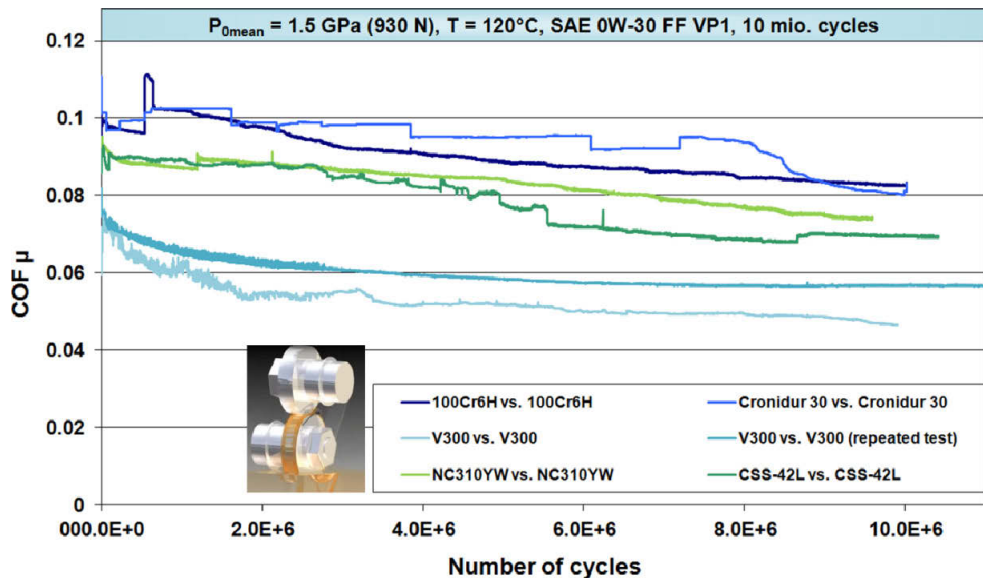


Figure 5-2: Evolution of the coefficient of friction over the test period of 10 million load cycles at $P_{0\text{mean}} = 1.5 \text{ GPa}$ and $T = 120^\circ\text{C}$ in SAE 0W-30 VP1 oil

Compared to the other steels V300 leads to a remarkable reduction in friction, which might be explained in two ways. The first possibility is the formation of tribo-reactive thin films (considered in paragraph 4.2) due to the contact pressure and presence of reactive oil additives. It would be conceivable that V300 offers a greater chemical affinity for the formation of reactive thin films on the steel surface than the other steel grades. Analysis of the material surface after the formation of a tribo-reactive layer by means of SEM/EDX, XPS and AES did not clearly identify the chemical composition of the films (cf. chapter 4.2). Therefore, further characterization and consideration on the formation of tribo-reactive layer are necessary and will be conducted in future research. The second possibility for explaining this test results is the formation of a nanocrystalline structure within the stressed area of V300. In industrial applications self-nanocrystallization is used to achieve increased mechanical properties of metallic surfaces. In order to achieve such structures, techniques are applied such as ultrasonic shot peening (USSP), high-energy shot peening (HESP) and surface mechanical attrition treatments (SMAT). Li et al. reported a markedly decrease in friction coefficients as well as wear mass loss associated with an increase of hardness up to a penetration depth of 5 μm and low grain sizes (between 10 and 20 nm) [Li10].

Comparing the test results obtained with SAE 0W-30 VP1 to those of polybutylene glycol PBG B20, an indication is evident for the formation of tribo-reactive thin film on V300. In Figure 5-3 the friction values are plotted of five steels, each tested with the aforementioned PBG B20 oil over the test duration of 10 million load cycles. In this case, the friction coefficients of 100Cr6H, V300, NC310YW and even Cronidur 30 are nearly in the same range of 0.06 and also comparable to the results of V300 lubricated with VP1. This result implies furthermore that PBG B20 offers a greater potential to decrease friction values independent from the steel choice, in contrast to VP1.

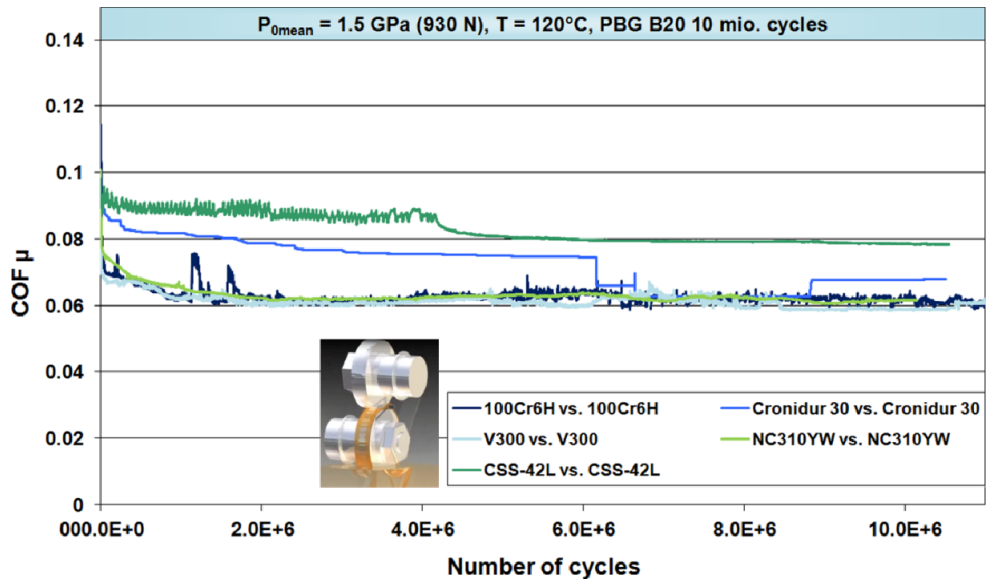


Figure 5-3: Evolution of the coefficient of friction over the test period of 10 million load cycles at $P_{0mean} = 1.5 \text{ GPa}$ and $T = 120^\circ\text{C}$ in PBG B20 oil

5.2 Influence of high performance thin film coatings

As shown above, the frictional profile of tribological systems can be optimized by a suitable material choice for example the high toughness steel grade V300. Similar results can be obtained by applying a highly wear resistant and low friction DLC coating. Therefore, an endurance test series was conducted, with different a-C:H thin film coatings of the BMW Group in order to show the frictional potential of these coating types. The test series was separated into two parts. The first part included the material pairing uncoated steel (spherical disc) vs. DLC-coated steel (cylindrical disc). After finishing these tests, the second part followed comprising the DLC-coated steel (spherical disc) vs. DLC-coated steel (cylindrical disc). In order to guarantee as same adhesion properties of the coatings on the steel surface, the grinded, spherical bodies were polished in the same manner like the cylindrical discs.

The test results are presented in Figure 5-4, including one endurance test of uncoated Cronidur 30 vs. uncoated 100Cr6H as reference (red curve) and the best in practice steel pairing, uncoated V300 vs. uncoated V300 (yellow curve). Considering the evolution of the coefficient of friction over the test duration (10 million load cycles), the diagram plotted revealed three areas.

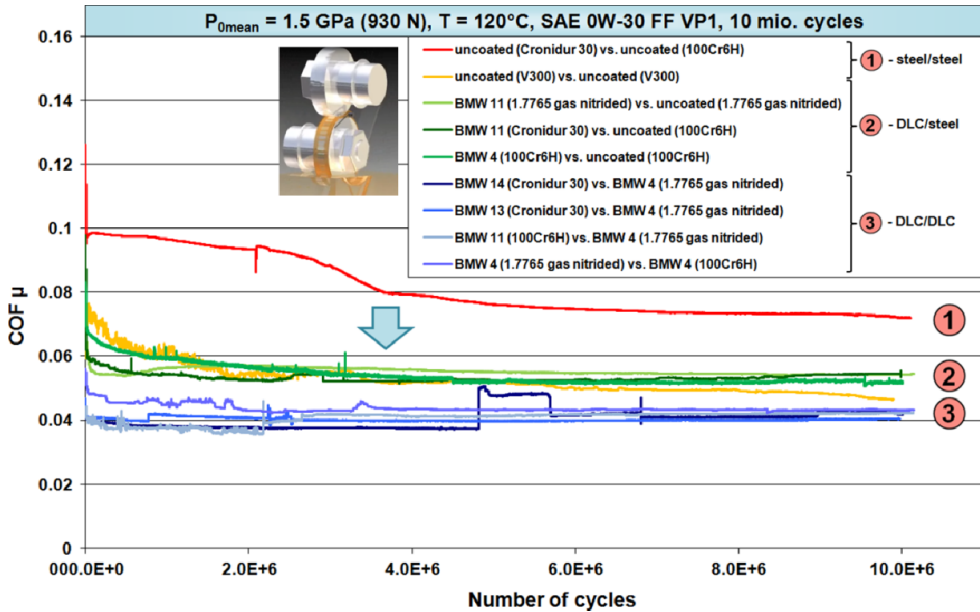


Figure 5-4: Comparison of friction coefficients of test pairings without any DLC coatings, single coated samples and pairings with DLC coatings applied on both samples tested at $P_{0mean} = 1.5 \text{ GPa}$ and $T = 120^\circ\text{C}$ in SAE 0W-30 VP1 oil

Area one represents uncoated steel pairings with average coefficients of friction of 0.07 at test end. The application of a DLC-coating on the cylindrical test sample could remarkably reduce the friction values, shown by the green curves in Figure 5-4. Considering the course of the yellow curve (uncoated V300) it is remarkable that suitable steels could offer the same potential to reduce friction as a DLC coating. Designing the lubricant for such steels the frictional benefit of uncoated steels could be more emphasized. The blue curves in Figure 5-4 represented by DLC vs. DLC pairings showed the most promising results to reduce friction. In comparison to uncoated systems the combination of DLC coatings in the contact is at the moment an optimum. However, these results were obtained using perfectly prepared steel surfaces before the coating process and showed what is potentially possible in future works.

5.3 Influence of lubricant additives

In this work, the frictional benefit of distinct DLC coatings was established. By nature DLC coatings are quite chemically inert which causes in a poor interaction of lubricants and their additives and the coating material. Figure 5-5 reveals another step in frictional optimization of tribological systems due to the interaction of DLC-coatings with special additives. The tests were conducted for 500,000 load cycles for each additive at 1.5 GPa using the self-mated DLC-coating BMW 4 and a modified version of the lubricant VP 1 containing no EP/AW additives. Testing each additive and coating for 500.000 load cycles new test cou-

Discussion and tribological considerations

ples for the following test were used. One percentage of the following additives was added to the lubricant:

- 2-ethylhexyl-molybdenum dialkyldithiophosphate (CAS number¹⁸: 72030-25-2)
- Molybdenum di-n-butyldithiocarbamate (CAS number: 68412-26-0)
- 5,5'-dithiobis-(1,3,4-thiadiazole-2(3H)-thione) (CAS number: 71342-89-7 and 64742-52-5)
- Dibenzyl disulfide (CAS number: 150-60-7)
- Triethanolamine >99% (CAS number: 102-71-6)

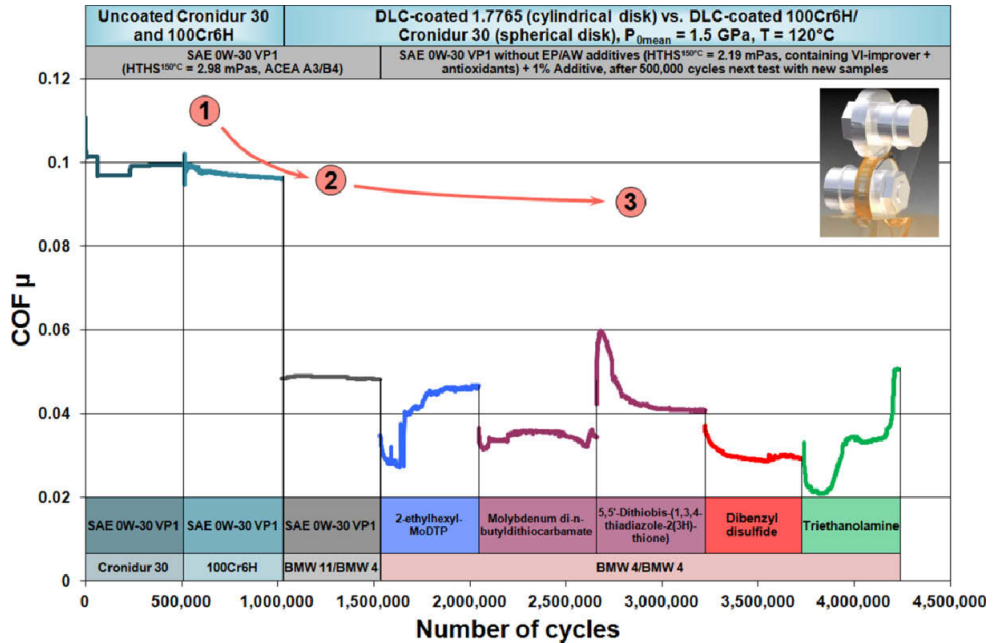


Figure 5-5: Frictional behavior of combining previously uncoated steel samples with DLC coatings and modified lubricant compositions in slip-rolling tests at $P_{\text{mean}} = 1.5 \text{ GPa}$ and $T = 120^\circ\text{C}$

In contrast to the general expectation of additivated lubricants not reacting with DLC coatings, a friction reducing effect of some additives became visible. Especially, the molybdenum containing complex as well as dibenzyl disulfide and triethanolamine revealed lower friction values down to 0.03. This fact is astonishing since the reduction of friction values due to DLC coatings is already known. The interaction of lubricant and coating represents a new perception of such tribo-systems and offers further potential for friction reduction.

These test results are a selection of other 25 different additives tested in combination with uncoated steel surface as well as DLC coatings. Hence, it has been shown that by optimiz-

¹⁸ CAS Registry Numbers are unique numerical identifiers assigned by the Chemical Abstracts Service to every chemical described in the open scientific literature and including elements, isotopes, organic and inorganic compounds, ions, organometallics, metals, nonstructurable materials. [CAS12]

ing the lubricant in terms of additives interacting with rather chemical inert surfaces the friction values could be remarkably reduced.

Considering the results obtained by use of VP1 and B20 oil at 120°C and uncoated steel surfaces, some differences became visible (compare Figure 5-2 and Figure 5-3). The curves of the friction coefficients in the case of VP1 are spread over a larger area than B20. This might be explained by the fact that VP1 is hydrocarbon based on the lubricity and tribological profile depending on the additives contained, whereas a polyglycol has in each monomer an oxygen polarity for adsorption and lubricity. Hydrocarbons are non-polar lubricants and thus inert. Therefore, this oil surely contains large amounts of additives interacting with the surfaces in combustion engines. In the case of B20 oil the additive package was considerably reduced under the premise of developing an environmentally friendly lubricant. Thus, the lubricant does not obtain such a great variety to form tribologically favorable complexes with the composed differently steels.

5.4 Global functional profile of coated and uncoated steels

Figure 5-6 summarizes the global impact of thin films and alternative, uncoated steels on friction and wear under mixed/boundary conditions for slip-rolling motion lubricated by SAE 0W-30 FF VP1 oil at 120°C. It is clearly visible at a glance that the friction values of completely uncoated systems offered considerably higher friction coefficients at test beginning than systems where both DLC coated surfaces are mated.

The majority of uncoated steels presented coefficients of friction between 0.06 – 0.09, but selected iron based steel metallurgies, such as the high toughness steel V300, can also achieve low values of ~0.04 in the same range as self-mated DLC-type thin films. From this point of view, it can be said that the application of thin film coatings on steel surfaces with their difficult deposition and quality assurance can be avoided, if alternative steels are considered at early design stage and used.

Basically, for wear resistance it is the same picture as for the frictional behavior. Thin films reduce wear rates by factors of 2 – 5, rather than by orders of magnitude. Some iron based steel metallurgies, especially in the case of V300 steel, can compete as uncoated triboelements with specific thin films. Some thin films enabled to reach the resolution limit of tactile technique used to quantify wear of these tests. In any case, coating both metal surfaces with DLC reduces the span observed in friction and wear rates.

In any case, low friction and “zero wear” requires a new metallurgy, either through thin films or alternative steels [Tam12]. Due to alternative steels, higher loads can be withstood by showing good fatigue strength properties and fracture toughness values in the frictional contact .

Discussion and tribological considerations

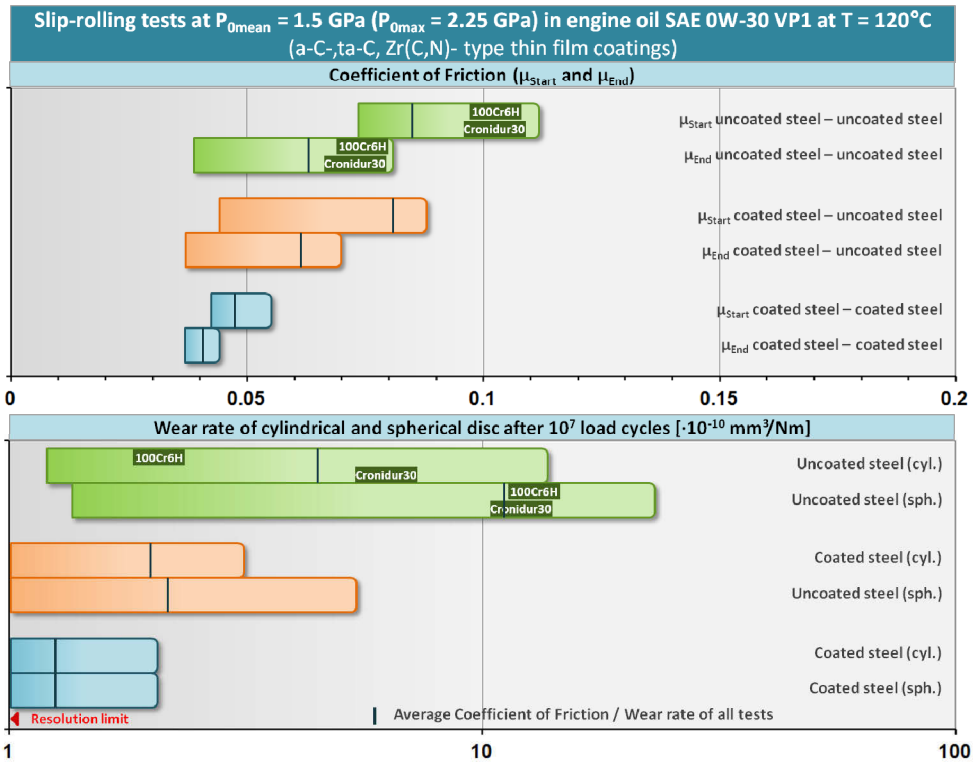


Figure 5-6: Comparison of friction and wear behavior of uncoated steel pairings, single coated pairings and pairings with two coated tribo-elements

6 Summary and Outlook

The objective target of the present work was to show the potential of different optimization paths to realize a low friction and low wear system under slip-rolling motion. Therefore, the development paths were tribologically considered in order to additionally improve the load carrying capacity and create an environmental friendly tribo-system:

- Alternative steels with high fatigue strength and fracture toughness properties
- Thin film coatings (Zr(C,N), DLC)
and
- Eco-no-tox lubricants including additives

This work investigates the frictional behavior of new but already available steels, namely V300, NC310YW and CSS-42L, with improved toughness values. For these steels in slip-rolling tests, the load carrying capacity could be increased to Hertzian contact pressures of $P_{0\text{mean}} = 2.5$ GPa respectively 2.62 GPa ($P_{0\text{max}} = 3.92$ GPa) in the mixed/boundary lubrication regime. The steels used had to sustain the contact pressure at a working temperature of motor oil in the range of 120°C for at least 10 million load cycles without showing surface failures. The steels V300 and NC310YW offered a slip-rolling resistance in endurance test up to contact pressures of 2.62 GPa and 2.5 GPa. Whereas, CSS-42L revealed a very good slip-rolling resistance even at stringent contact pressures of 2.62 GPa ($F_N = 5,000$ N) applied never before to such a tribological system. Furthermore, the steel V300 can offer a friction reduction of approximately 40% in mixed/boundary lubrication regime compared to commonly used in uncoated steel/steel contact. Moreover, it has been shown that the formation of tribo-reactive thin films could be initiated by high loads and suitable lubricants. By means of EDX, XPS and AES analysis the formation of a Ca-based film could be detected on the steel surface. The most likely explanation is that overbased sulfonate structures contained in the hydrocarbon based engine oil react with the iron surface to form a boundary film composed of CaO and CaCO₃.

The structural composition and residual stress evolution after tribological tests of V300, NC310YW and CSS-42L has been investigated. Furthermore, structural changes due to high load stressing could considerably change the microstructure and residual stresses of steels (see paragraphs 4.3 and 4.4). In the case of V300 and NC310YW, two nearly chemically similar composed steels were compared. Structural FIB/TEM analysis revealed distinct differences influencing the whole tribological behavior (cf. chapter 4.4.2). The actually lower slip-rolling resistance of NC310YW is due to higher density of dislocations which impede the ability of plastic deformations.

New test results concerning the slip-rolling resistance of high performance thin film coatings such as a-C:H, ta-C and Zr(C,N) could be achieved. These results could be obtained due to high annealing temperature (> 300°C) of the new steels used which favors optimal DLC coating deposition temperature and finally a good adhesion on the steels substrate. The superiority of high toughness steels tested in reference tests without any coating up to

Summary and Outlook

$P_{0\text{mean}}$ of 2.62 GPa became also visible by the application of thin films. Contrary to commonly used steels such as 100Cr6H the coating/steel pairing revealed good test result without plastic flow of the substrate. Particularly, novel a-C:H coatings of KYB Corp. and BMW Group could reduce the wear rates down to a hardly detectable limit, not to say down to 'zero-wear'. Even better results with regard to wear and friction values could be achieved by applying DLC coatings at both rolling contacts leading to a friction reduction of nearly 50% compared to the reference steel pairing 100Cr6H/Cronidur30. Furthermore, the beneficial interaction of distinct lubricants additives and DLC-coatings (a-C:H) using a modified oil (no friction modifier or EP-/AW-additives contained) at 120°C could be observed by the reduction of friction values in comparison to a non-modified factory fill engine oil.

It has been shown that the global functional profile of tribological systems could be optimized by the application of suitable steel and coating combinations. With regard to the potential of CO₂ emission reduction in internal combustion engines (see Figure 6-1) it became visible that still existing and optimized technologies offers certain capabilities for new improvements.

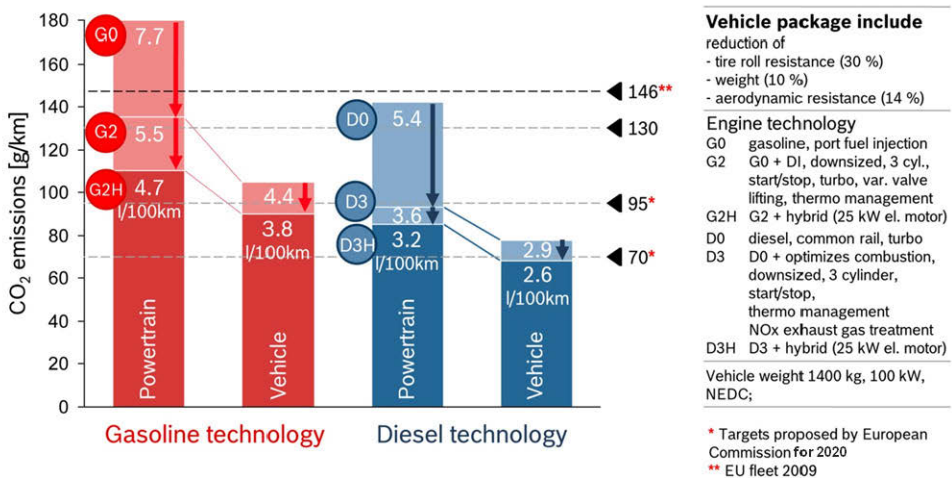


Figure 6-1: Final CO₂ reduction by vehicle technology (gasoline and Diesel) [Leo11]

Anyway, the maximum durability of the both slip-rolling test machines (Amsler and Optimol) used of 2,000 N and respectively 5,000 N was reached within the test series conducted in the present work. The testing conditions chosen here are extreme and permit a clear differentiation of the steels and thin film coatings as well as to set an extended upper limit for load carrying capacity under slip-rolling above FZG 14. In the future, the load carrying capacity of the steels should be increased further with regard to the light weight design of mechanical systems. Therefore, new steel production processes need to be used in order to create steel solutions with micro-structural benefits and improved mechanical properties

with strength values reaching 5,000 MPa. The ASP¹⁹ process developed by Aubert & Duval – Erasteel (France) enables the production of high-speed steels that include high amounts of carbon and carbide forming alloying elements while reducing the carbide size to a few microns at the same time. The benefit of gas atomization of metallic powders and following hot isostatic compaction aims, to achieve an exceptional fatigue resistance (rotating bending strength at 20 million cycles between 1,100 MPa and 1,450 MPa) [Ger10]. Furthermore, the tribological characteristics as well as the structures of new steels applied should be investigated and examined exactly especially with regard to white and dark etching areas for example.

For enhanced tribological performance, the interaction of machining and operating conditions, material surface and lubricants moves more and more in to focus. Therefore, it would be necessary to characterize the formation of so called tribo-reactive thin films in detail for a specific application. The formation of a tribo-reactive thin film during the machining and running-in process is schematically illustrated in Figure 6-2. By applying such thin films low friction and high wear resistant surfaces could be generated during the machining process while reducing the running-in time of the tribological system.

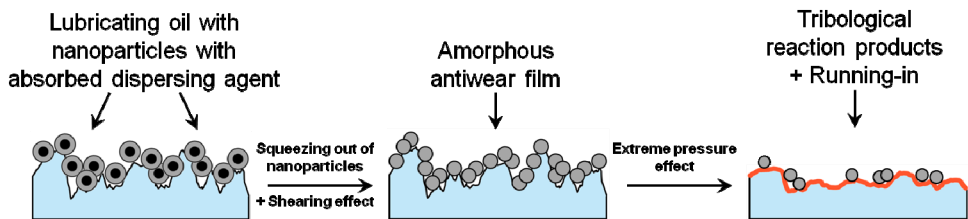


Figure 6-2: Formation of tribo-reactive thin films during machining processes in principle

On the basis of the present state of knowledge the formation of tribo-reactive films is favored by uncoated steels surfaces in combination with high contact pressures, operating conditions above room temperature and lubricant oils containing additives which are able to quickly form layers on surfaces. As shown in the present work, DLC coatings could interact with selected additives to reduce the friction and wear values. However, further studies of these reactions are necessary to understand the tribological system 'DLC coating and lubricant' and create tribo-reactive films carbon-coated surfaces.

¹⁹ ASP – Asea-Stora-Process (Erasteel – Aubert & Duval), special gas atomization process of molten steels using inert gas jets to obtain fine metal droplets which cool down during their fall in the atomizing tower. In the following step the high cleanliness level steel powders were compacted by Hot Isostatic Pressing for further process steps such as forging, hot rolling or drawing.

7 References

- [Abu03] Abudaia, F. B.: Microstructure and Fatigue Strength of High Performance Gear Steels, PhD thesis, University of Newcastle, 2003.
- [Aub10] Aubert & Duval: Special Steels and Superalloys for Bars, http://www.aubertduval.com/fileadmin/user_upload/pdf_gb/Produits_long_s_GB_04_2010.pdf, 2010.
- [Bar07] Barros Bouchet, de M. I., Kano, M.: Superlubricity of Diamond/Glycerol Technology Applied to Automotive Gasoline Engines, in: Erdemir, A., Martin, J.-M.: Superlubricity, Elsevier, pp. 253 – 271, Amsterdam, 2007.
- [Bha79] Bhadeshia, H. K. D. H., Edmonds, D. V.: The bainite transformation in silicon steel, Metallurgical and Materials Transactions A, Vol. 10, No. 7, pp. 895 – 907, 1979.
- [Bha90] Bhargava, V., Hahn, G. T., Rubin, C. A.: Rolling Contact Deformation, Etching Effects, and Failure of High-Strength Bearing Steel, Metallurgical Transactions A, Vol. 21, No. 7, pp. 1921 – 1931.
- [Bha90-2] Bhadeshia, H. K. D. H., Christian, J.W.: Bainite in Steels, Metallurgical Transactions A, Vol. 21, No. 3, pp. 767 – 797, 1990.
- [Bha01] Bhadeshia, H. K. D. H.: Bainite in Steels, Transformations, Microstructure and Properties, Second Edition, IOM Communications Ltd., 2001, ISBN 1-86125-112-2.
- [Bha11] Bhadeshia, H. K. D. H.: Steels for bearings, Progress in Materials Science, Vol. 57, Issue 2, pp. 268 – 435, 2011.
- [Bha12] Bhadeshia, H. K. D. H.: Steels for bearings, Progress in Materials Science, Vol. 57, Issue 2, pp. 268 – 435, 2012.
- [Böh99] Böhmer, H.-J., Hirsch, T., Streit, E.: Rolling contact fatigue behaviour of heat resistant bearing steels at high operational temperatures, Materialwissenschaft und Werkstofftechnik, Vol. 30, Issue 9, pp. 533 – 541, 1999.
- [Böh10] Böhmer, H.-J.: Wälzverschleiß und -ermüdung von Bauteilen und Maßnahmen zu ihrer Einschränkung, in: Woydt, M.: Reibung und Verschleiß von Werkstoffen und Dünnschichten, Bauteilen und Konstruktionen, Ursachen – Analyse – Optimierung, expert verlag, Renningen, 2010.

- [Bra13] Bragg, W. L.: The Diffraction of Short Electromagnetic Waves by a Crystal, Proceedings of the Cambridge Philosophical Society, Vol. 17, pp. 43 – 57.
- [Cab11] Caballero, F. G., Yen, H.-W., Miller, M. K., Yang, J.-R., Cornide, J., Garcia-Mateo, C.: Complementary use of transmission electron microscopy and atom probe tomography for the examination of plastic accommodation in nanocrystalline bainitic steels, Acta Materialia, Vol. 59, Issue 15, pp. 6117 – 6123, 2011.
- [Cal07] Callister, W. D.: Materials Science and Engineering: An Introduction, 7th ed., John Wiley & Sons, Inc., New York, 2007.
- [Car07] Carciun, D., Socol, G., Stefan, N., Mihailescu, I. N., Bourne, G., Craciun, V.: High-repetition rate pulsed laser deposition of ZrC thin films, Surface & Coatings Technology, Vol. 203, Issue 8, pp. 1055 – 1058, 2009.
- [CAS12] American Chemical Society:
<http://www.cas.org/expertise/cascontent/registry/regsys.html>, 15.06.2012
- [Cha84] Chang, L., Smith, G. D. W.: The Silicon Effect in the Tempering of Martensite in Steels, Journal de Physique Colloques, Vol. 45, No. C9, pp 397 – 401, 1984.
- [Che88] Cheng, L., Brakman, C. M., Korevaar, B. M., Mittemeijer, E. J.: The Tempering of Iron-Carbon Martensite; Dilatometric and Calorimetric Analysis, Metallurgical Transactions A, Vol. 19, No. 10, pp. 2415 – 2426, 1988
- [Ciz04] Cizaire, L., Martin, J. M., Le Mogne, Th., Gresser, E.: Chemical analysis of overbased calcium sulfonate detergents by coupling XPS, ToF-SIMS, XANES and EFTEM, Colloids and Surfaces A: Physicochemical and Engineering Aspects, Vol. 238, Issues 1 – 3, pp. 151 – 158, 2004.
- [Czi03] Czichos, H., Habig, K.-H.: Tribologie-Handbuch, 2nd edition, Vieweg Verlag, Wiesbaden, 2003.
- [Dah06] Grądzka-Dahlke, M.: A tribological study of composite material based on iron with addition of calcium pyrophosphate, Wear, Vol. 261, Issues 11 – 12, pp. 1383 – 1389.
- [Del05] Delagnes, D., Lamesle, P., Mathon, M. H., Mebarki, N., Levallant, C.: Influence of silicon content on the precipitation of secondary carbides and fatigue properties of a 5%Cr tempered martensitic steel, Materials Science and Engineering: A, Vol. 394, Issues 1 – 2, pp. 435 – 444, 2005.

References

- [Ene12] Energietechnik Essen GmbH: Datenblatt Cronidur30 <http://www.energietechnik-essen.de/uk/products/high-nitrogen-steels/cronidur-30.html>, State 04.01.2012.
- [EU09] Regulation (EC) No 443/2009 of the European Parliament and the Council: setting emission performance standards for new passenger cars as part of the Community's integrated approach to reduce CO₂ emissions from light-duty vehicles, Official Journal of the European Union, pp. L 140/1 – 140/15, 05.06.2009.
- [Erd04] Erdemir, A.: Genesis of superlow friction and wear in diamondlike carbon films, *Tribology International*, Vol. 37, Issues 11 – 12, pp. 1005 – 1012, 2004.
- [Erd07] Erdemir, A., Eryilmaz, O. L.: Superlubricity in Diamondlike Carbon Films, in: Erdemir, A., Martin, J.-M.: Superlubricity, Elsevier, pp. 253 – 271, Amsterdam, 2007.
- [Eva12] Evans, M.H.: White structure flaking (WSF) in wind turbine gearbox bearings: effects of 'butterflies' and white etching cracks (WECs), *Materials Science and Technology*, Vol. 28, No. 1, pp. 3 – 22, 2012.
- [Fer08] Ferrari, A. C.: Non-destructive characterization of carbon films, in: Donnet, C., Erdemir, A.: *Tribology of Diamond-like Carbon Films: Fundamentals and Applications*, Springer-Verlag, pp. 25 – 82, New York, 2008.
- [Fla09] Flacelière, L., Sourmail, T., d'Eramo, E., Daguier, P., Dabas, H., Marchand, J.: Steel solutions designed for wind mills, European Conference on Heat Treatment, Strasbourg, France, 19 and 20 March 2009.
- [Gen12] Genzel, C.: personal conversation, Helmholtz Zentrum Berlin, 10.01.2012.
- [Ger10] Germidis, A.: Advanced materials for future IC engines, Case Study: Aubert & Duval – Erasteel, Annual Showcase, pp. 36 – 38, 2010.
- [Gil11] Gili, F., Igartua, A., Luther, R., Woydt, M.: The impact of biofuels on engine oil performance, *Lubrications Science*, Vol. 23, Issue 7, pp. 313 – 330, Wiley Online Library, 2011.
- [Gle10] Glebov, A. G., Arabey, A. B., Lutsenko, A. N., Pikunov, M. V., Nemtinov, A. A.: Role of Silicon in the Macro- and Microstructure of High-Strength Steel, *Steel in Translation*, Vol. 40, No. 5, pp. 398 – 406, 2010.

- [Gol07] Gold, P. W., Loos, J., Plogmann, M.: Ermüdungslebensdauer PVD-beschichteter Wälzlager, Proc. of the 48th Tribology-Symposium, Gesellschaft für Tribology e.V.: Göttingen, 46/1, 24 – 26 September 2007, ISBN 978-3-00-022603-8.
- [Gra10] Grabulov, A., Petrov R., Zandbergen, H. W.: EBSD investigation of the crack initiation and TEM/FIB analyses of the microstructural changes around the cracks formed under Rolling Contact Fatigue (RCF), International Journal of Fatigue, Vol. 32, Issue 3, pp. 576 – 583, 2010.
- [Gra10-2] Grabulov, A.: Fundamentals of Rolling Contact Fatigue, PhD thesis, Delft University of Technology, ISBN 9789077172551, 2010.
- [Ham81] Hamrock, B. J., Dowson, D.: Ball Bearing Lubrication, The Elastohydrodynamics of Elliptical Contacts, John Wiley & Sons, New York, 1981.
- [Har05] Harada, H., Mikami, T., Shibata, M., Sokai, D., Yamamoto, A., Tsubakino, H.: Microstructural Changes and Crack Initiation with White Etching Area Formation under Rolling/Sliding Contact in Bearing Steel, ISIJ International, Vol. 45, No. 12, pp. 1897 – 1902, 2005.
- [Har07] Harris T.A., Kotzalas M.N., Essential Concepts of Bearing Technology. Rolling Bearing Analysis. Fifth Edition, Taylor and Francis, USA, 2007.
- [Hau97] Hauk, V.: Structural and Residual Stress Analysis by Nondestructive Methods: Evaluation - Application - Assessment, Elsevier, Amsterdam, 1997, ISBN 0 444 82476 6.
- [Her81] Hertz, H.: Ueber die Berührung fester elastischer Körper, Journal für die reine und angewandte Mathematik, No. 92, pp. 156 – 171, 1881.
- [Het08] Hetzner, D. W., Van Geertruyden, W.: Crystallography and metallography of carbides in high alloy steels, Materials Characterization, Vol. 59, Issue 7, pp. 825 – 841, 2008
- [Hip03] Hipler, F., Girol, S. G., Azzam, W., Fischer, R. A., Wöll, C.: Interaction of Thiadiazole Additives with Metal Surfaces: Reactions and Thin-Film Formation on Gold as a Model Surface, Langmuir, Vol. 19, Issue 15, pp. 6072 – 6080, 2003.
- [Hol09] Holmberg, K., Matthews, A.: Coating Tribology, Properties, Mechanisms, Techniques and Applications in Surface Engineering, Elsevier, Tribology and Interface Engineering Series, No. 56, Amsterdam, 2009.

References

- [Jan08] Jang, J. H., Kim, I. G., Bhadeshia, H. K. D. H.: Substitutional solution of silicon in cementite: A first-principles study, *Computational Materials Science*, Vol. 44, Issue 4, pp. 1319 – 1326, 2008.
- [Kan95] Kanisawa, H., Ochi, T., Koyasu, Y.: Development of High-Strength Carburized Steels for Automobile Gears, *Nippon Steel Technical Report No. 64*, 1995.
- [Kan06] Kano, M.: Super low friction of DLC applied to engine cam follower lubricated with ester-containing oil, *Tribology International*, Vol. 39, Issue 12, pp. 1682 – 1685, 2006.
- [Kan12] Kang, J.-H., Hosseinkhani, B., Rivera-Díaz-del-Castillo, P. E. J.: Rolling contact fatigue in bearings: multiscale overview, *Materials Science and Technology*, Vol. 28, No. 1, pp. 44 – 49, 2012.
- [Kar70] Kardonskii, V. M.: Silicon in Maraging Steels, *Metal Science and Heat Treatment*, Vol. 12, No. 7, pp. 547 – 550, 1970.
- [Kim10] Kim, K.-H., Jae-Seung, L., Duk-Lak, L.: Effect of Silicon on the Spheroidization of Cementite in Hypereutectoid High Carbon Chromium Bearing Steels, *Metals and Materials International*, Vol. 16, No. 6, pp. 871 – 876, 2010.
- [Kol04] Kolzer: Vacuum Deposition Processes, Vacuum Deposition Processes, equipment and applications, 14.07.2004, http://www.kolzer.com/files/vacuum_deposition_guide.PDF.
- [Kot10] Kotzalas, M. N., Doll, G. L.: Tribological advancements for reliable wind turbine performance, *Phil. Trans. R. Soc. A*, Vol. 368, No. 1929, pp. 4829 – 4850, 2010.
- [Kra00] Krantz, T. L., Alanou, M. P., Evans, H. P., Snidle, R. W.: Surface Fatigue Lives of Case-Carburized Gears With an Improved Surface Finish, *Technical Memorandum NASA /TM-2000-21 0044*, John H. Glenn Research Center at Lewis Field, Cleveland, Ohio, 2000.
- [Kra03] Krantz, T. L., Cooper, C. V., Townsend, D. P., Hansen, B. D.: Increased Surface Fatigue Lives of Spur Gears by Application of a Coating, *Technical Memorandum NASA/TM—2003-212463*, John H. Glenn Research Center at Lewis Field, Cleveland, Ohio, 2003.
- [Kra08] Krantz, T., Tufts, B.: Pitting and Bending Fatigue Evaluations of a New Case-Carburized Gear Steel, *Gear Technology*, March/April 2008.

- [Kub82] Kubaschewski, O.: Iron-Binary Phase Diagrams, Springer-Verlag, Berlin, pp. 136 – 139, 1982.
- [Kub07] Kubo, T., Fujiwara, S., Nanao, H., Minami, I., Mori, S.: Boundary film formation from overbased calciumsulfonate additives during running-in process of steel–DLC contact, *Wear*, Vol. 265, Issues 3 – 4, pp. 461 – 467, 2007.
- [Kud77] Kudielka, H.: Die Kristallstruktur von Fe_2Si , ihre Verwandtschaft zu den Ordnungsstrukturen des α -(Fe,Si)-Mischkristalls und zur Fe_5Si_3 -Struktur, *Zeitschrift für Kristallographie*, Band 145, pp. 177 – 189, 1977.
- [Kur30] Kurdjumow, G.V., Sachs, G.: Über den Mechanismus der Stahlhärtung, *Zeitschrift für Physik*, Vol. 64, No. 5 – 6, pp. 325 – 343, 1930.
- [Kur75] Kurdjumov, G. V., Khachaturyan, A. G.: Nature of Axial Ratio Anomalies of the Martensite Lattice and Mechanism of Diffusionless $\gamma \rightarrow \alpha$ Transformation, *Acta Metallurgica*, Vol. 23, Issue 9, pp. 1077 – 1088, 1975.
- [Lac91] Lacaze, J., Sundman, B.: An Assessment of the Fe-C-Si System, *Metallurgical Transactions A*, Vol. 22, No. 10, pp. 2211 – 2223, 1991.
- [Lac05] Lackner, J. M.: Industrially-scaled large-area and high-rate tribological coating by Pulsed Laser Deposition, *Surface and Coatings Technology*, Vol. 200, Issues 5 – 6, pp. 1439 – 1444, 2005.
- [Lat95] Maloney, J. L., Tomasello, C. M.: United States Patent, Patent Number: 5,424,028, 1995.
- [Läp06] Läßle, V.: Wärmebehandlung des Stahls, 9th edition, Verlag Europa-Lehrmittel, Haan-Gruiten, 2006, ISBN: 978 3 8085 1309 5
- [Leo11] Leonhard, R.: Reducing CO₂ emissions with optimized internal-combustion engines, 60th Automotive Press Briefing, Boxberg, June 2011.
- [Li10] Li, G., Chen, J., Guan, D.: Friction and wear behaviors of nanocrystalline surface layer of medium carbon steel, *Tribology International*, Vol. 43, Issue 11, pp. 2216 – 2221, 2010.
- [Lia10] Liang, Y. F., Lin, J. P., et al.: Microstructure and mechanical properties of rapidly quenched Fe-6.5 wt.% Si alloy, *Journal of Alloys and Compounds*, Vol. 504, Supplement 1, pp. S476-S479, 2010.

References

- [Liu07] Liu, S. J., Hua, D. Y.: Wear behaviour of W-DLC coating under reciprocating sliding motion, ASTM D02 Symposium on Wear and Friction Test Methods for Coatings and Surface Treatments, Miami Beach, Florida, 21. June 2007.
- [Lub12] Lubrizol Corp.: ACEA A3/B4-10, 09.08.2012, <http://www.lubrizol.com/EngineOilAdditives/ACEA/Sequences/ACEA-A3B4-10.html>.
- [Lub12-2] Lubrizol Corp.: ACEA C4-10, 09.08.2012, <http://www.lubrizol.com/EngineOilAdditives/ACEA/Sequences/ACEA-C4-10.html>.
- [Luc69] Lucas, G., Nützel, H.: Gefüge- und Maßänderungen von Wälzlagerteilen bei erhöhten Betriebstemperaturen, Wälzlagertechnische Sonderschriften, SKF Kugellagerfabriken GmbH, pp. 1 – 8, 1969.
- [Lun10] Lund, T. B.: Subsurface initiated rolling contact fatigue – influence of non-metallic inclusions, processing conditions, and operating conditions, Journal of ASTM International, Vol. 7, Issue 5, pp. 1 – 12, 2010.
- [Lün91] Lünenberger, A.: Zum Unwandlungs- und Verformungsverhalten bainitisch-austenitischer Siliziumstähle, PhD thesis, Universität Karlsruhe, 1991.
- [Man07] Mang, T., Dresel, W.: Lubricants and Lubrication, 2nd edition, Wiley-VCH GmbH, Weinheim, 2007, ISBN 978-3-527-31497-3.
- [Man10] Manier, C.-A.: Slip-rolling resistance of novel Zr(C,N) thin film coatings under high Hertzian contact pressures, BAM-Dissertationsreihe, Band 60, Berlin, 2010.
- [Man10-2] Manier, C.-A., Ziegele H., et al.: Zirconium-based coatings in highly stressed rolling contacts as alternative solution to DLC and ta-C coatings, Wear, Vol. 269, Issues 11 – 12, pp. 770 – 781, 2010.
- [Man10-3] Manier, C.-A., Theiler, G., Spaltmann, D., Woydt, M., Ziegele, H.: Benchmark of thin film coatings for lubricated slip-rolling contacts, Wear, Vol. 268, Issues 11 – 12, pp. 1442–1454, 2010.
- [Mar01] Martin, J. M., Grossiord, C., Le Mogne, T., Bec, S., Tonck, A.: The two-layer structure of Zndtp tribofilms: Part I: AES, XPS and XANES analyses, Tribology International, Vol. 34, Issue 8, pp. 523 – 530, 2001.
- [Mar10] Martin, J., Krell, L., Schnagl, J., Stahl, K.: Flächeneinfluss bei der PACVD-Beschichtung, Variation der Eigenschaften von DLC-Schichten, Vakuum in Forschung und Praxis, Vol. 22, Issue 3, pp. 6 – 10, 2010.
- [Mat00] Mattox, D. M.: Ion plating – past, present and future, Surface and Coatings Technology, Vol. 133 – 134, pp. 517 – 521, 2000.

- [Mat08] Matta, C., De Barros Bouchet, M. I., Le-Mogne, T., Vachet, B., Martin, J.M., Sagawa, T.: Tribochemistry of tetrahedral hydrogen-free amorphous carbon coatings in the presence of OH-containing lubricants, *Lubrication Science*, Vol. 20, Issue 2, pp. 137 – 149, 2008.
- [Mau12] Maurin-Perrier, P., Diaby, M.: Contribution of DLC coatings to the Friction Reducing of Internal Combustion Engines, 18th International Colloquium Tribology, TAE, Esslingen, 21 – 23 January 2012.
- [Miy11] Miyama, E., Voit, C., Pohl, M.: Zementitnachweis zur Unterscheidung von Bainitstufen in modernen, niedriglegierten Mehrphasenstählen, *Practical Metallography*, Issue 5, pp. 261 – 272, 2011.
- [Miy11-2] Miyama, E.: Metallographische Methoden zur Charakterisierung moderner hoch- und höchstfester Mehrphasenstähle, Kolloquium der Abteilung 5 „Werkstofftechnik“, BAM, Berlin, 29 March 2011.
- [Mor04] Morina, A., Neville, A., Green, J.H., Priest, M.: Additive/additive interactions in boundary lubrication—a study of film formation and tenacity, *Proc. 31st Leeds–Lyon Symposium on Tribology, Life Cycle Tribology*, Elsevier, Amsterdam, pp.757 – 766, 2004.
- [Mor07] Morina, A., Neville, A.: Tribofilms: aspects of formation, stability and removal, *Journal of Physics D: Applied Physics*, Vol. 40, No. 18, pp. 5476 – 5487, 2007.
- [Mov69] Movchan, B.A., Demchishin, A.V.: Study of the structure and properties if thick vacuum condensates of nickel, titanium, tungsten, aluminum oxide and zirconium dioxide, *Fizika metallov i metallovedenie*, Vol. 28, Issue 4, pp. 83 – 90, 1969.
- [Msi08] Materials Science and International Team (MSIT[®]): Ternary Alloy Systems, Phase Diagrams, Crystallographic and Thermodynamic Data, in: Martienssen, W.: *Londolt-Börnstein Numerical Data and Functional Relationships in Science and Technology*, Subvol. D Iron Systems, Part 2 Selected Systems from C-Cr-Fe to Co-Fe-S, Springer, Heidelberg, 2008.
- [Mur70] Muro, H., Tsushima, N.: Microstructural, Microhardness and Residual Stress Changes due to Rolling Contact, *Wear*, Vol. 15, Issue 5, pp. 309 – 330, 1970.
- [Mur10] Murrenhoff, H.: *Umweltverträgliche Tribosysteme, Die Vision einer umweltfreundlichen Werkzeugmaschine*, Springer-Verlag, Heidelberg, 2010.

References

- [Nel99] Nélias, D., Dumont, M. L., Champiot, F., Girodin, D., Fougères, R., Flamand, L.: Role of Inclusions, Surface Roughness and Operating Conditions on Rolling Contact Fatigue, *Journal of Tribology*, Vol. 121, Issue 2, pp. 240 – 251.
- [Nic05] Nicholls, M. A., Do, T., Norton, P. R., Kasrei, M., Bancroft, G. M.: Review of the lubrication of metallic surfaces by zinc dialkyl-dithiophosphates, *Tribology International*, Vol. 38, Issue 1, pp. 15 – 39, 2005.
- [NIST] NIST X-ray Photoelectron Spectroscopy Database: http://srdata.nist.gov/xps/main_search_menu.aspx, 24.04.2012.
- [NSK12] NSK: Ultra Clean Steel Extends Bearing Life, NSK Motion & Control, http://www.nskamericas.com/cps/rde/xbcr/na_en/10_TechTalk_Ultra_Clean.pdf, 01.06.2012.
- [Oht90] Ohtani, H., Okuaguchi, S., Fujishiro, Y., Ohmori, Y.: Morphology and properties of low-carbon bainite, *Metallurgical and Materials Transactions A*, Vol. 21, No. 3, pp. 877 – 888, 1990.
- [Ono10] Onodera, T., Morita, Y., Suzuki, A., Sahnoun, R., Koyama, M., Tsuboi, H., Hatakeyama, N., Endou, A., Takaba, H., Del Carpio, C. A., Deka, R. C., Kubo, M., Miyamoto, A.: Tribochemical Reaction Dynamics of Molybdenum Dithiocarbamate on Nascent Iron Surface: A Hybrid Quantum Chemical/Classical Molecular Dynamics Study, *Journal of Nanoscience and Nanotechnology*, Vol. 10, No. 4, pp. 2495 – 2502, 2010.
- [Öst80] Österlund, R., Vingsbo, O.: Phase Changes in Fatigued Ball Bearings, *Metallurgical Transactions A*, Vol. 11, Issue 5, pp. 701 – 707, 1980.
- [Peš03] Pešička, J., Kužel, R., Dronhofer, A., Eggeler, G.: The evolution of dislocation density during heat treatment and creep of tempered martensite ferritic steels, *Acta Materialia*, Vol. 51, Issue 16, pp. 4847 – 4862, 2003.
- [Pir02] Piras, F. M.: In situ Attenuated Total Reflection Tribometry, A new approach for the chemical analysis of tribological films, PhD thesis, University of Cagliari, 2002.
- [Rad11] Radu, C.: It's All About the Steel: the Importance of Bearing Steel Cleanliness for Long-Life Applications, RKB Technical Report, 2011.
- [Rag02] Ragen, M. A., Anthony, D. L., Spitzer, R. F.: A comparison of the mechanical and physical properties of contemporary and new alloys for aerospace bearing applications, in: Beswick, J. M.: *Bearing Steel Technology*, STP 1419, ASTM International, Philadelphia, pp. 362 – 374, 2002.

- [Ren02] Renault, S. A.: Sustainable development – “ELLYPSE” – radically designed, Das Magazin für Forschung und Entwicklung, No. 26, October 2002, Publisher: Renault, S.A., Direction de la Communication, rue du Vieux-Pont-de-Sèvres, F-92109 Boulogne-Billancourt, ISSN: 1289-009x.
- [Rix01] Rix, W.: Über Eisensilicide: Züchtung von β -FeSi₂-Einkristallen durch chemischen Transport, strukturelle und physikalische Charakterisierung, PhD thesis, University of Freiburg, 2001.
- [Röt05] Röhler, B.: Möglichkeiten zur Beeinflussung der mechanischen Eigenschaften von kaltgewalzten TRIP-Stählen, PhD thesis, Technische Universität München, 2005.
- [Rud09] Rudnick, L. R.: Lubricant Additives, Chemistry and Applications, 2nd edition, CRC Press Taylor & Francis Group, Boca Raton, 2009, ISBN 978-1-4200-5964-9.
- [SAE09] SAE International: J300, Engine Oil Viscosity Classification, 12.01.2009.
- [San82] Sandvik, B. P. J.: The Bainite Reaction in Fe-Si-C Alloys: The Primary Stage, Metallurgical and Materials Transactions A, Vol. 13, No. 5, pp. 777 – 787, 1982.
- [San82-2] Sandvik, B. P. J.: The Bainite Reaction in Fe-Si-C Alloys: The Secondary Stage, Metallurgical and Materials Transactions A, Vol. 13, No. 5, pp. 789 – 800, 1982.
- [Sch18] Scherrer, P.: Bestimmung der Größe und der inneren Struktur von Kolloidteilchen mittels Röntgenstrahlung, Nachrichten von der Gesellschaft der Wissenschaften zu Göttingen, Vol. 2, pp. 98 – 100, 1918.
- [Sch73] Schlicht, H.: Über die Entstehung von White Etching Aeras (WEA) in Wälzelementen, Härterei-Technische Mitteilungen 28, Heft 2, pp. 112 – 123, 1973.
- [Sch88] Schlicht, H., Schreiber, E., Zwirlein, O.: Effects of Material Properties on Bearing Steel Fatigue Strength, in: Hoo, J. J. C., Effect of Steel Manufacturing Processes on the Quality of Bearing steels, STP 987, ASTM International, Philadelphia, 1988.
- [Sch06] Schmidt, R., Klingenberg, G., Woydt, M.: New lubrication concepts for environmental friendly machines, BAM Research Report Nr. 277, Bundesanstalt für Materialforschung und –prüfung, Berlin, 2006.

References

- [Sch10] Schorck, W.: Reibungsminderung an Antriebs- und Motorenkomponenten durch Beschichtungen mit diamantähnlichen amorphen Kohlenstoff, Fraunhofer Institut für Werkstoff- und Strahltechnik, Fraunhofer Verlag, Stuttgart, 2010.
- [Sch10-2] Schulz, J., Holweger, W.: Wechselwirkung von Additiven mit Metalloberflächen, expert Verlag, Renningen, 2010.
- [Sch11] Scholz, C., Spaltmann, D., Woydt, M.: Slip-rolling resistance of thin films and high toughness steel substrates under high Hertzian contact pressures, *Wear*, Volume 270, Issues 7 – 8, pp. 506 – 514, 2011.
- [Sch11-2] Schnagl, J., Köhn, M., Ziegele, H.: Optimierte Achsgetriebe durch DLC-Beschichtung und angepassten Schmierstoff, Reibungsminimierung im Antriebsstrag, 2nd ATZ symposium, Esslingen, Germany, 29 and 30 November 2011.
- [Sei71-72] Seitzinger, K., Richter, M.: Grenzen und Möglichkeiten der FZG-Zahnrad-Verspannungs-Prüfmaschine zur Prüfung von Hypoidgetriebeölen I-V, *Schmierungstechnik und Tribologie*, Vol. 18, pp. 223 – 227, 1971 and Vol. 19, pp. 22 -29, pp. 58 – 60, pp. 128 – 130, pp. 145 – 148, 1972.
- [SFB09] SFB 570: Distortion Engineering, Projekt C1, Stoffwertbestimmung, Universität Bremen, 2009.
- [Sha11] Sharma, S., Sangal, S., Mondal, K.: Development of New High-Strength Carbide-Free Bainitic Steels, *Metallurgical and Material Transactions A*, Vol. 42, Nr. 13, pp. 3921 – 3933, 2011.
- [She11] Shen, T., Krantz, T., Sebastian, J.: Advanced Gear Alloys for Ultra High Strength Applications, Technical Memorandum NASA/TM-2011-217121, John H. Glenn Research Center at Lewis Field, Cleveland, Ohio, 2011.
- [Shi03] Shigley, J., Mischke, C. R., Budynas, R. G.: *Mechanical Engineering Design* 7th edition, McGraw-Hill Science, 2003.
- [Spa04] Spaltmann, D., Löhr, M., Binkowski, S., Woydt, M.: Einfluss der Topographie von DLC-Schichten auf deren Verhalten unter geschmierter Walzbeanspruchung, *Tribologie und Schmierungstechnik*, Vol. 51, No. 6, pp. 18 – 26, 2004.
- [Spa05] Spaltmann, D., Löhr, M., Binkowski, S., Kelling, N., Soltwedel, R., Woydt, M., Santner, E.: Schäden wälzbeanspruchter DLC-Schichten auf Stahlsubstraten unterschiedlicher Härte, *Materialwissenschaft und Werkstofftechnik*, Vol. 36, Issue 2, pp. 62 – 68, 2005.

- [Spe12] Speakman, S. A.: Estimating Crystallite Size Using XRD, MIT Center for Materials Science and Engineering, 07.05.2012, <http://prism.mit.edu/xray/tutorials.htm>.
- [Spi09] Spieß, L., Schwarzer, R., Behnken, H., Genzel, C.: Moderne Röntgenbeugung, Röntgendiffraktometrie für Materialwissenschaftler, Physiker und Chemiker, 2nd edition, Vieweg + Teubner, Wiesbaden, 2009.
- [Sta93] Stachowiak, G. W., Batchelor, A. W.: Engineering Tribology, Tribology Series, 24, Elsevier, Amsterdam, 1993.
- [Sta08] Staňková, H.: Einfluss der inkrementellen Deformationen bei der thermo-mechanischen Behandlung auf die Eigenschaften von TRIP-Stählen, PhD thesis, Technische Universität Chemnitz, Werkstoffverhalten, Band 003, 2008.
- [Ste05] Steinmann, M.: Beitrag zur Entwicklung neuartiger PVD-Festschmierstoffschichten für den Einsatz in trockenlaufenden Maschinenelementen, insbesondere wälzgelagerten Linearführungen, Fortschr.-Ber. VDI Reihe 1, Nr. 382, VDI Verlag, Düsseldorf, 2005.
- [Swa76] Swahn, H., Becker, P. C., Vingsbo, O.: Martensite decay during rolling contact fatigue in ball bearings, Metallurgical Transactions A, Vol. 7, Issue 8, pp. 1099 – 1110, 1976.
- [Tam12] Tamura, T., Hosohata, S., Nakase, T., Kato, S., Scholz, C., Woydt, M.: High wear resistance DLC film under high pressure contact, 12th Machine Design and Tribology Division Meeting, JSME, Ehime-ken, Japan, 23 – 24 April 2012.
- [Tak12] Takechi, H., Hanamura, T., Torizuka, S., Imagumbai, M.: Mechanical Properties of Grain refined 5%Mn-2%Si Advanced High Strength Steel for Automotive Applications, Materials in Car Body Engineering 2012, Bad Nauheim, 10 – 11 June 2012.
- [Tho74] Thornton, J. A.: Influence of apparatus geometry and deposition conditions on the structure and topography of thick sputtered coatings, Journal of Vacuum Science and Technology, Vol. 11, No. 4, pp. 666 – 670, 1974.
- [Tho93] Thom, R., Moore L., et al.: Rolling contact fatigue tests of reactively sputtered nitride coatings of Ti, Zr, Hf, Cr, Mo, Ti-Al, Ti-Zr and Ti-Al-V on 440C stainless steel substrates, Surface and Coatings Technology, Vol. 62, Issues 1 – 3, pp. 423 – 427, 1993.

References

- [Tho00] Thompson, C.V.: Structure Evolution during Processing of Polycrystalline Films, Annual Review of Materials Science, Vol. 30, pp. 159 – 190, 2000.
- [Tom02] Tomasello, C. M., Burrier, H. I., Knepper, R. A., Balliet, S., Maloney, J. L.: Progress in the Evaluation of CSS-42LTM: A High Performance Bearing Alloy, in: Beswick, J. M.: Bearing Steel Technology, STP 1419, ASTM International, Philadelphia, pp. 375 – 385, 2002.
- [Toy07] Toyoda, S.: All Toyota tribological innovation to realize “Zeronize” and “Maximize” society, Tribology Online, Vol. 2, No. 1, pp. 19 – 22, 2007.
- [VDI05] VDI-guideline 2840, Carbon films – basic knowledge, film types and properties, ICS 25.220.99, Beuth Verlag, Berlin, 2005.
- [Vos96] Voskamp, A. P.: Microstructural changes during rolling contact fatigue, PhD thesis, Technical University of Delft, 1996.
- [Vöh77] Vöhringer, O., Macherauch, E.: Struktur und mechanische Eigenschaften von Martensit, Vol. 32, No. 4, pp. 153 – 168, 1977.
- [Wan02] Wan, Y., Suominen Fuller, M. L., Kasrai, M., Bancroft, G. M., Fyfe, K., Torkelson, J. R., Hu, Y. F., Tan, K. H.: Effects of detergent on the chemistry of tribofilms from ZDDP: studied by X-ray absorption spectroscopy and XPS, Tribology Series, Vol. 40, pp. 155 – 166, 2002.
- [Wan02-2] Wang, L.: Microstructure and Residual Stress State in the Contact Zone of Rails and Wheels, PhD thesis, TU Berlin, 2002.
- [Wan09] Wang, L., Pan, Y., Chen, Y., Sun, F., Hu, K.: Analysis on Microstructure and Properties of Cold-rolling Automotive Applications TRIP Steel with 1.20% Si, Proc. Of 2009 International Symposium on Automobile Steel, Metallurgical Industry Press, Beijing, pp. 258 – 261, 2009.
- [War68] Warlimont, H.: Elektronenmikroskopische Untersuchung der Gleichgewichte und Umwandlung der α -Eisen-Silizium-Phasen, Z. Metallkde., Band 59, Heft 8, pp. 595 – 602, 1968.
- [Wäs89] Wäsche, R.: Feste Schmierstoffe für hohe Temperaturen: Eine Literaturübersicht, Tribologie und Schmierungstechnik, No. 3, pp. 145 – 151, 1989.
- [Wit08] Wittig, J. E., Frommeyer, G.: Deformation and Fracture Behavior of Rapidly Solidified and Annealed Iron-Silicon Alloys, Metallurgical and Materials Transactions A, Vol. 39, No. 2, pp. 252 – 262, 2008.

- [Woo06] Woo, A. J., Bourne, G., Craciun, V., Craciun, D., Singh, R. K.: Mechanical properties of ZrC thin films grown by pulsed laser deposition, *Journal of Optoelectronics and Advanced Materials*, Vol. 8, No. 1, pp. 20 – 23, 2006.
- [Woy08] Woydt, M., Criqui, B., Desplanches, G., Linnemann, T.: Zero wear concept using bionotox and polymer-free engine oils with triboactive materials, *Industrial Lubrication and Tribology*, Vol. 60, Issue 1 pp. 14 – 23, 2008.
- [Woy09] Woydt, M., Manier, C.-A., Brückner, A., Weihnacht, V.: Slip-rolling resistant thin film ta-C coatings for up to 3.000 MPa of Hertzian contact pressure, *Proc. of the 50th Tribology-Symposium*, Gesellschaft für Tribology e.V.: Göttingen, 55/1, 21 – 23 September 2009, ISBN 978-3-00r-r028824-1.
- [Woy10] Woydt, M., Manier, C.-A., Brückner, A., Weihnacht, V.: Wälzbeständigkeit von ta-C Dünnschichten unter hohen Hertzischen Beanspruchungen bis zu 3000 MPa, *Tribologie und Schmierungstechnik*, Vol. 57, No. 6, pp. 30 – 36, 2010.
- [Woy10-2] Woydt, M., Wäsche, R.: The history of the Stribeck curve and ball bearing steels: The role of Adolf Martens, *Wear*, Vol. 268, Issues 11 – 12, pp. 1542 – 1546, 2010.
- [Woy11] Woydt, M.: Oil Free Machinery and “Zero Wear” - Dream or Reality?, *Tribology Online*, Vol. 6, No. 1, pp. 101 – 112, 2011.
- [Wri10] Wright, J. A., Sebastian, J. T., Kern, C. P., Kooy, R. J.: Design, Development and Application of New, High-Performance Gear Steels, *Gear Technology*, January/February 2010.
- [Wut86] Wuttke, W.: *Tribophysik, Reibung und Verschleiß von Metallen*, VEB Fachbuchverlag Leipzig, Leipzig, 1986.
- [Yan02] Ros-Yañez, T., Houbaert, Y., Gómez Rodríguez, V.: High-silicon steel produced by hot dipping and diffusion annealing, *Journal of Applied Physics*, Vol. 91, Issue 10, pp. 7857 – 7859, 2002.
- [Yu11] Yu, L. G., Yamaguchi, E. S., Kasrai, M., Bancroft, G. M.: Study of silane-based antiwear additives: Wear and chemistry, *Tribology International*, Vol. 44, Issue 6, pp. 692 – 701, 2011.
- [Zaj05] Zajac, S., Komenda, J., Morris, P., Dierickx, P., Matera, S., Penalba Diaz, F.: Quantitative structure-property relationships for complex bainitic microstructures, Commission of European Communities ECSC sponsored technical steel research project, Final report, Brussels, 2005, ISBN: 92 894 9206 6.

References

- [Zar90] Zaretsky, E. V.: Bearing and Gear Steels for Aerospace Applications, Technical Memorandum NASA TM-102529, Lewis Research Center, Cleveland, Ohio, 1990.
- [Zha12] Zhao, F., Bai, Z., Fu, Y., Zhao, D., Yan, C.: Tribological properties of serpentine, $\text{La}(\text{OH})_3$ and their composite particles as lubricant additives, *Wear*, Vol. 288, pp. 72 – 77, 2012.
- [Zhi97] Zhitomirsky, V. N., Grimberg I., et al.: Vacuum arc deposition and microstructure of ZrN-based coatings, *Surface and Coatings Technology*, Vol. 94 – 95, pp. 207 – 212, 1997.

8 List of figures and tables

Figures

Figure 1-1: CO ₂ emissions of selected engine technologies in the European Union over the kerb weight including the European CO ₂ targets for 2015 and 2020 [Leo11]	1
Figure 1-2: Scheme of aspired goals and approaches of this work	3
Figure 2-1: Increase in lifetime by use of optimized 100Cr6 in comparison to commonly melted and treated 100Cr6 [Woy10-2]	5
Figure 2-2: The progressive stages of spalling forming in relation to non-metallic inclusions [NSK12]	6
Figure 2-3: Weibull plot of fatigue test data for both uncoated and coated spur gears illustrates improved fatigue lives of coated gear parts [Kra03]	9
Figure 2-4: DLC coated bevel gear components [Mau12]	9
Figure 2-5: Evolution of residual stresses by cyclic rolling stress (left) and influence of contact pressure as well as slip on the residual stress profile (right) [Böh10]	11
Figure 2-6: Changes of residual stress and half-value breadth through cyclic stressing of martensitic and bainitic structures [Sch88] (left) and residual stress profiles as function of number of cycles for a 52100 steel (850 HV) at 3.2 GPa contact pressure [Bha12] (slip rates in both figures not specified by the authors)	11
Figure 2-7: Optical image of white etching areas through inner ring of a wind turbine main shaft roller bearing in the cross section below stressed raceway	12
Figure 2-8: Schematic development of early stage butterflies influenced by spherical Al ₂ O ₃ inclusion in SAE 52100 steel [Gra10-2]	14
Figure 2-9: Schematic diagrams of Evans theory butterflies and WECs causing WSF failures in SAE 52100 bearing raceways [Eva12]	15
Figure 2-10: Optical micrograph of a dark etching area (within the image labeled as dark etching region DER) in cross section of a groove ball bearing after $2.4 \cdot 10^8$ load cycles under contact pressures of 2.6 GPa [Gra10-2]	16
Figure 2-11: Experimental binary Fe-Si phase diagram [Kub82]	17
Figure 2-12: Magnitude of stress components below the surface as function of maximum pressure for contacting spheres (left) and cylinders (right) with $\nu = 0.3$ in static case [Man10] [Shi03]	23
Figure 2-13: Determination of the contact coefficients k ₁ , k ₂ , k ₃ , k ₄ and k ₅ [Sta93]	24

List of figures and tables

Figure 2-14: Development of the maximum shear stress depending on the coefficient of friction [Wut86]	25
Figure 2-15: Characterization of friction regimes according to the Stribeck curve [Czi03]	27
Figure 2-16: Dynamic behavior of LI-MoDTC molecule on nascent Fe(001) surface [Ono10]	28
Figure 2-17: Schematic model and formation processes of the ZDDP/MoDTC tribofilm during the induction phase and at the end of the test. I – formation of N-containing species and ZDDP tribofilm resulting in wear reduction. II – adsorption of Mo oxide beside formation of species from process I. III – adsorption of MoS ₂ and Mo oxide aside from ZDDP tribofilm [Mor07]	29
Figure 2-18: Schematic representation of structure zone models of Movchan and Demchishin (left) [Mov69] and Thorton (right) [Tho74] with the influence of temperature and argon pressure on the microstructure of metal coatings. T (K) is the substrate temperature and T _m (K) represents the melting point of the coating material.	33
Figure 3-1: New demands on light-weight gear components derived from DIN 3990-5 (1987).	36
Figure 3-2: Schematic heat treatment curve of the 100Cr6H, Cronidur 30, V300, NC310YW and CSS-42L materials	39
Figure 3-3: Microstructures of (a) 100Cr6H (etchant: Nital), (b) carbide structure 100Cr6H (etchant: sulfurous acid) and (c) Cronidur 30 (etched by Energietechnik Essen, scale: a), c) 50 µm and b) 100 µm)	40
Figure 3-4: Structural composition of (a) V300 and (b) NC310YW (etchant: Nital, scale: 50 µm)	41
Figure 3-5: Microstructure of CSS-42L: a) Me ₂₃ C ₆ carbides including martensitic case, b) transition zone below carburized case and c) core (etchant: HNO ₃ and Marble, scale: a), c) 50 µm and b) 500 µm)	41
Figure 3-6: Hardness depth profiles (HV 0.2) of steels used	42
Figure 3-7: TEM analysis of the interface between steel substrate and Zr(C,N)-coating: pcnl structure (left) and conventionally deposited structure (right) [Man10] (scale: 50 nm)	43
Figure 3-8: SIMS measurement of a used a-C:H type DLC coating (BMW 4) performed at Fraunhofer IST Braunschweig	43

Figure 3-9: Structural characterization of coatings BMW 4, BMW 11 and KYB Type A by atomic force microscopy	44
Figure 3-10: Sample arrangement in the Amsler type tribometer	46
Figure 3-11: Configuration of the test samples on an Optimol 2Disc tribometer	48
Figure 4-1: Optical light microscopy photographs of the typical wear tracks of rolling steel/steel contacts displaying their morphology at different load stages, $P_{0\text{mean}} = 1.5, 1.94, 2.5$ and 2.62 GPa (scale: $500 \mu\text{m}$ respectively $1000 \mu\text{m}$ for all pictures)	52
Figure 4-2: Evaluation of the planimetric wear surface W_q by tactile profilometry	53
Figure 4-3: Comparison of wear rates of different uncoated steel pairings following the tests in BMW FF SAE 0W-30 VP1 at $T = 120^\circ\text{C}$	54
Figure 4-4: SEM images of the wear tracks of the steels a) V300, b) NC310YW and c) CSS-42L stressed at 1.5 GPa (scale: a) $3 \mu\text{m}$, b) and c) $2 \mu\text{m}$)	54
Figure 4-5: Summary of the coefficients of friction at the beginning and at the end of the test of uncoated steels	55
Figure 4-6: a) EDX Chromium mapping of CSS-42L and b) wear track of CSS-42L after 10 million load cycles at $P_{0\text{mean}} = 1.94$ GPa with detected microcracks along the chromium carbides (scale: a) $4 \mu\text{m}$ and b) $1 \mu\text{m}$)	56
Figure 4-7: Magnifications of the affected surfaces of a) NC310YW, b) 102Cr6 and c) 100Cr6H (scale: $200 \mu\text{m}$)	57
Figure 4-8: Results of Fraunhofer IWS Dresden a-C and ta-C thin film coating under slip-rolling conditions	59
Figure 4-9: Defects of Fraunhofer IWS coatings at $P_{0\text{mean}} = 1.5$ GPa in VP1 a) ta-C V5, b) ta-C V6 and c) a-C V7 (scale: a) $1000 \mu\text{m}$, b) and c) $500 \mu\text{m}$)	59
Figure 4-10: Slip-rolling resistance auf BMW a-C:H coatings BMW 4 and BMW 11 with corresponding coefficients of friction (BMW Group, Munich)	60
Figure 4-11: Wear tracks of BMW 4 and BMW 11 coatings after tests at $P_{0\text{mean}} = 2.5$ GPa: a) BMW 4 on CSS-42L, b) BMW 11 on V300 and c) BMW 11 on CSS-42L (scale: $500 \mu\text{m}$)	61
Figure 4-12: AFM images of the unaffected BMW 11 coating surface (left) and the coating surface after slip-rolling test at $P_{0\text{mean}} = 1.5$ GPa in BMW FF SAE 0W-30 VP1 at 120°C (right)	61
Figure 4-13: Diagram summarizing the slip-rolling resistance obtained with Zr(C,N) coatings of different batches deposited by Fundación Tekniker, Spain (test results of K(1) to K(9) determined by Manier [Man10])	62

List of figures and tables

Figure 4-14: Sections of stressed and partial flaked Zr(C,N) wear tracks after a) 1.11 mio. cycles (V300), b) 4.98 mio. cycles (NC310YW) and c) 10 mio. cycles (CSS-42L) tested at $P_{0\text{mean}} = 2.5 \text{ GPa}$ and $T = 120^\circ\text{C}$ (scale: $500 \mu\text{m}$)	63
Figure 4-15: Slip-rolling resistance of a-C:H and a-C:H:Me coatings provided by KYB Co., Japan	63
Figure 4-16: Optical micrographs of the stressed under $P_{0\text{mean}} = 1.5 \text{ GPa}$ KYB coatings a) type A after 10 mio. load cycles and b) type B after 3.32 mio. load cycles (scale: $500 \mu\text{m}$)	64
Figure 4-17: Slip-rolling test results of different BMW DLC coating against BMW 4 at $P_{0\text{mean}} = 1.5 \text{ GPa}$ and 120°C	65
Figure 4-18: Images of the wear tracks by optical micrographs: a) BMW 4 counterbody of b) BMW 13 test sample, c) BMW 4 counterbody of d) BMW 11 test sample after 10 million load cycles at $P_{0\text{mean}} = 1.5 \text{ GPa}$ (scale: $500 \mu\text{m}$)	66
Figure 4-19: SEM pictures of V300, NC310YW and CSS-42L wear tracks and corresponding local EDX spectra of noticeable areas tested in VP1 at 1.5 GPa and 120°C after 10 million load cycles (scale: $5 \mu\text{m}$ and $25 \mu\text{m}$)	68
Figure 4-20: White appearing tribo-reactive layer on V300 counterbody (left) and SEM observation of the stressed wear track and unaffected outlying area tested at $P_{0\text{mean}} = 2.5 \text{ GPa}$ and 120°C in VP1(scale: $40 \mu\text{m}$)	69
Figure 4-21: SEM images of BMW 11 coated V300 (left) and uncoated V300 (right) tested in VP1 oil at 2.5 GPa (600,000 load cycles) and 120°C superimposed with EDX mappings (scale: $40 \mu\text{m}$)	70
Figure 4-22: SEM images of Zr(C,N) coated V300 (left) and uncoated V300 (right) tested in VP1 oil at 2.5 GPa (600,000 load cycles) and 120°C superimposed with EDX mappings (scale: $40 \mu\text{m}$)	71
Figure 4-23: XPS spectrum of BMW 11 inside the wear track after 10 million load cycles at $P_{0\text{mean}} = 2.5 \text{ GPa}$ and 120°C in VP1	72
Figure 4-24: XPS spectrum of uncoated V300 inside the wear track after 10 million load cycles at $P_{0\text{mean}} = 2.5 \text{ GPa}$ and 120°C in VP1	74
Figure 4-25: AES spectra of the pairings BMW 11/V300 and Zr(C,N)/V300 taken inside the wear track after tests in VP1 at 120°C and $P_{0\text{mean}} = 2.5 \text{ GPa}$ (600,000 load cycles)	74
Figure 4-26: X-ray diffraction spectrum of a) V300, b) NC310YW and c) CSS-42L with CoK_α -radiation	76

Figure 4-27: Hardness and residual stress depth profiles and corresponding FWHM values at $\psi = 0^\circ$ and $\pm 63.435^\circ$ measured with $\sin^2\psi$ -method in the initial unstressed state of V300, NC310YW and CSS-42L	78
Figure 4-28: Hardness and residual stress depth profiles and corresponding FWHM values at $\psi = 0^\circ$ and $\pm 63.435^\circ$ measured with $\sin^2\psi$ -method in the initial unstressed state of V300, NC310YW and CSS-42L after tribological tests at $P_{0\text{mean}} = 1.94$ GPa	81
Figure 4-29: Hardness and residual stress depth profiles and corresponding FWHM values at $\psi = 0^\circ$ and $\pm 63.435^\circ$ measured with $\sin^2\psi$ -method in the initial unstressed state of V300 (left) and NC310YW (right, failure at 1.26 million load cycles) after tribological tests at $P_{0\text{mean}} = 2.5$ GPa	83
Figure 4-30: Optical micrograph taken from a) V300 and b) NC310YW cross sections after slip-rolling tests at $P_{0\text{mean}} = 1.94$ GPa (scale: 500 μm)	84
Figure 4-31: Comparison of hardness depth profiles of unstressed and under 1.94 GPa tested V300 (left) and NC310YW (right) test samples	85
Figure 4-32: Hardness profiles of V300, NC310YW and CSS-42L measured in the depth profiles and parallel to the surface directly underneath the wear track after testing at 2.5 GPa (scale: 500 μm)	86
Figure 4-33: SEM overview in cross section taken from unstressed V300, images a) and b), and NC310YW, images c) and d), microstructures (scale: a) 3 μm , b),c) 1 μm and d) 300 nm)	87
Figure 4-34: a) Transmission electron micrograph of bainitic structure (combination of cementite and ferrite) according Callister [Cal07] and b) SEM image of V300 microstructure with EDX measurement positions Pt1 to Pt5 (scale: a) 1 μm and b) 200 nm)	89
Figure 4-35: SEM images underneath the wear track after tribological tests at 2.5 GPa of a) V300 and b) NC310YW (scale: 1 μm)	90
Figure 4-36: SEM pictures and FIB cross sections of a) V300 bulk structure and b) observed structure underneath the wear track (scale: a), b) 20 μm and c), d) 5 μm)	91
Figure 4-37: Selected area electron diffraction pattern taken from V300 TEM overview image including characteristic orientations (scale: 500 nm)	92
Figure 4-38: TEM overview of stressed V300 lath martensitic microstructure (area of hardness increase) and corresponding SAED pattern (scale: 50 nm)	92
Figure 4-39: TEM and SAED images of granular bainitic structures (a, b) found in stressed V300 microstructure and micro twins within the ferrite structure in [011] orientation (c, d) (scale: a) 500 nm, c) 200 nm)	93

List of figures and tables

Figure 4-40: Selected area electron diffraction pattern taken from NC310YW TEM overview image including the interpretation of one lath colony diffraction pattern (scale: 500 nm)	94
Figure 4-41: Silicon distribution in structure of a) V300 and b) NC310YW observed by means of SEM/EDX measurements	95
Figure 4-42: Quantitative EDX-analysis of characteristic TEM points in NC310YW steel matrix and the corresponding content results (scale: 1 μm)	96
Figure 4-43: 200 reflex diffractogram of the steels V300 and NC310YW including the fitted tetragonal distorted diffraction profile	97
Figure 4-44: Dilatometer curves of different iron-carbon martensite steel grades showing the different stages of structural changes during tempering [Che88]	98
Figure 5-1: Restriction of the slip-rolling resistance of a-C:H coatings due to plastic deformation and flow of steel substrates presented in a) 100Cr6H and b) Cronidur 30 tested at 1.94 GPa and comparatively c) the high slip-rolling resistant coating BMW 4 on CSS-42L tested at 2.5 GPa for 18 days (scale: a), b) 1 mm and c) 500 μm)	100
Figure 5-2: Evolution of the coefficient of friction over the test period of 10 million load cycles at $P_{0\text{mean}} = 1.5 \text{ GPa}$ and $T = 120^\circ\text{C}$ in SAE 0W-30 VP1 oil	102
Figure 5-3: Evolution of the coefficient of friction over the test period of 10 million load cycles at $P_{0\text{mean}} = 1.5 \text{ GPa}$ and $T = 120^\circ\text{C}$ in PBG B20 oil	104
Figure 5-4: Comparison of friction coefficients of test pairings without any DLC coatings, single coated samples and pairings with DLC coatings applied on both samples tested at $P_{0\text{mean}} = 1.5 \text{ GPa}$ and $T = 120^\circ\text{C}$ in SAE 0W-30 VP1 oil	105
Figure 5-5: Frictional behavior of combining previously uncoated steel samples with DLC coatings and modified lubricant compositions in slip-rolling tests at $P_{0\text{mean}} = 1.5 \text{ GPa}$ and $T = 120^\circ\text{C}$	106
Figure 5-6: Comparison of friction and wear behavior of uncoated steel pairings, single coated pairings and pairings with two coated tribo-elements	108
Figure 6-1: Final CO_2 reduction by vehicle technology (gasoline and Diesel) [Leo11]	110
Figure 6-2: Formation of tribo-reactive thin films during machining processes in principle	111

Tables

Table 2-1: Phase description of binary Fe-Si system	18
Table 2-2: Maximal, mean contact pressure and maximum shear stress with its depth position following the Hertz theory for elliptical contact used in twin disc testing machines (see paragraph 0) [Man10]	25
Table 2-3: Typical characteristics of some coating processes (gaseous state)[Hol09]	32
Table 3-1: Mechanical properties and tempering temperatures of steel grades used	38
Table 3-2: Chemical composition of the steel grades (wt.-%)	38
Table 3-3: Typical roughness values of polished, cylindrical and grinded, spherical steel samples	40
Table 3-4: Properties of the different DLC and Zr(C,N) coating systems tested	45
Table 3-5: Experimental conditions	47
Table 3-6: Hertzian contact pressures for the sample geometries tested	48
Table 3-7: Viscosimetric properties of engine oil SAE 0W-30 VP1 and Polybutylene Glycol B20 [Sch06]	49
Table 4-1: Roughness values of coatings KYB Type A, KYB Type B, BMW 4 and BMW 11 measured	64
Table 4-2: Schematic representation of different bainite morphologies according [Zaj05], [Miy11], [Miy11-2] and [Tak12]	88
Table 4-3: Carbon content of analyzing points Pt1 - Pt5 in V300 microstructure by EDX (wt.-%)	89
Table 4-4: Parameters of synchrotron X-ray measurements at DESY (Hamburg) of the steels V300 and NC310YW	96
Table 4-5: Results of the calculated c_m/a_m ratio and dissolved carbon content of the steels V300 and NC310YW	98
Table 5-1: Summary of the global structural and tribological profiles of the steels V300, NC310YW and CSS-42L observed in this work	101